Faculty of Engineering

Experimental and Numerical Investigations on Micromixers and Micropumps for Performance Enhancement in Point-of-Care (POC) Applications

Buglie anak Lawrence Nanu

Doctor of Philosophy
2024

Experimental and Numerical Investigation on Micromixers and Micropumps for Performance Enhancement in Point-of-Care (POC) Applications

Buglie anak Lawrence Nanu

A thesis submitted

In fulfillment of the requirements for the degree of Doctor of Philosophy

(Mechanical Engineering)

Faculty of Engineering
UNIVERSITI MALAYSIA SARAWAK
2024

DECLARATION

I declare that the work in this thesis was carried out in accordance with the regulations of Universiti Malaysia Sarawak. Except where due acknowledgements have been made, the work is that of the author alone. The thesis has not been accepted for any degree and is not concurrently submitted in candidature of any other degree.

……

Signature

Name: Buglie anak Lawrence Nanu

Matric No.: 20010021

Faculty of Engineering

Universiti Malaysia Sarawak

Date:

ACKNOWLEDGEMENT

I would like to express my deepest appreciation to Assoc. Prof. Ir. Dr. Khairul Fikri bin Tamrin, my supervisor for the professional assistance and helpful guidance throughout this study.

My sincere gratitude to the Yayasan Sarawak for the financial support through Biasiswa Yayasan Sarawak Tun Taib, and an appreciation also given to the Universiti Malaysia Sarawak (UNIMAS) for the continuous support on materials and equipment through Postgraduate Student Research Grant (F02/ PGRG/2043/2020).

Finally, I glorify the Heavenly Father who deeply strengthen and guide me towards the journey in life, and to Valanie, Ruth Abigail and all family members who always motivate me, physically and mentally. Thank you.

ABSTRACT

Point-of-care (POC) device is a medical tool for a rapid initial diagnosis of near-patient testing which suits the necessities in telemedicine. In POC devices, lamination-based passive micromixers have been largely used. This, however, requires a long mixing channel to mix fluid or bioassays completely. To overcome this, structured two-dimensional (2D) mixing channels have been introduced as an alternative to achieve the same mixing performance but with a shorter channel length. Hence, in this present study, two variants of the obstacle-based 2D passive micromixer were shortlisted, namely the T-micromixer with circular mixing channel and Tesla micromixer were introduced and fabricated to identify the best micromixer for POC application. Micromixer selection was based on the liquid mixing performance determined using the RGB method. Tesla micromixer was selected due to the capability to mix fluid completely (MI = 100%) compared to the T-micromixer with circular mixing channel (MI =57.33%) at the same Re = 40. On the other hand, passive micropumps are alternatives for conventional benchtop pumps used in POC devices due to the latter are usually placed at the micromixer inlets hence multiple units are required to drive fluids into a micromixer that has many inlets. Apart from that, running on these conventional pumps also may cause leakage in the device due to the higher working pressure than the ambient. Therefore, to cope with these shortcomings, two variations of the passive micropump were suggested, namely the multi-angle paper-based capillary (MAPC) and sub-atmospheric pressure (SAP) micropumps. They were fabricated and assessed for the selection of the suitable micropump to be used in the proposed POC unit. The micropump selection was based on the flow rate performance of the mentioned micropumps. During standalone operations, the SAP micropump has a higher flow rate (Q = 49.9 μL/s) as compared to the MAPC micropump (24.4 μL/s), thus it was selected to be integrated with Tesla micromixer

in the proposed POC unit. SAP micropumps were identified to be suitable for attachment to the outlet of a micromixer for overcoming the leakage problem in tubing networks. In the final stage, the numerical investigation was done in terms of CFD simulations to optimize the gauge pressure of the integrated unit of the Tesla micromixer and SAP micropump. Optimization showed a complete fluid mixing was achieved at a gauge pressure of -10 kPa. In addition, the simulation showed that fluid mixing was caused by the generation of Dean vortices and minor chaotic advection at each valve stage. It was also identified that the actual gauge pressure was lesser than the simulated gauge pressure, and found to be diminished with time due to the physical limitation of the micropump chamber. In overall, the mixing performance between the simulation and experiment compares well despite the deviation of about -0.51 kPa, and demonstrates the viability of the proposed POC unit for enhanced fluid mixing.

Keywords: Micromixing, micropumping, point-of-care, micromixer, micropump

Kajian Experimentasi dan Berangka Pencampur dan Pam Mikro bagi Meningkatkan Prestasi Bendalir di dalam Peranti Titik Rawatan (POC)

ABSTRAK

Peranti titik rawatan (POC) merupakan salah satu alat diagnosis perubatan yang pantas dan sesuai untuk pengesanan awal penyakit terutamanya dalam aplikasi teleperubatan. Di dalam peranti POC, pencampur mikro pasif berasaskan laminasi telah banyak digunakan. Walau bagaimanapun, saluran pencampuran yang panjang adalah diperlukan di dalam peranti ini untuk cecair diadun secara lengkap. Bagi Untuk mengatasi masalah ini, saluran pencampuran berstruktur dua dimensi (2D) atau tiga dimensi (3D) diperkenalkan sebagai alternatif untuk mencapai prestasi adunan yang sama namun dengan panjang saluran yang lebih pendek. Oleh yang demikian, di dalam kajian ini, dua varian pencampur 2D pasif berasaskan halangan telah dipilih iaitu pencampur mikro T dengan saluran pencampuran bulat dan pencampur mikro Tesla telah diperkenalkan dan diselidik bagi mengenal pasti pencampur mikro terbaik untuk aplikasi POC. Pencampur mikro Tesla dipilih berasaskan keupayaannya untuk mengadun cecair sepenuhnya (MI = 100%) berbanding dengan pencampur mikro T dengan saluran pencampuran bulat (MI = 57.33%) pada Re = 40 yang sama. Sebaliknya, pam mikro pasif adalah suatu alternatif untuk pam konvensional yang biasa digunakan bersama dengan peranti POC. Ini adalah kerana pam konvesuional ini kerap diletakkan di salur masuk pencampur mikro menyebabkan berberapa unit diperlukan untuk mengepam cecair ke dalam pencampur mikro yang mempunyai banyak salur masuk. Selain itu, pam konvensional juga boleh menyebabkan kebocoran di dalam peranti POC disebabkan ia bekerja dengan tekanan yang lebih tinggi daripada tekanan atmosfera. Untuk mengatasi kelemahan ini, dua variasi pam mikro pasif telah dicadangkan, iaitu pam mikro kapilari kertas berbilang sudut (MAPC) dan pam mikro tekanan sub-atmosfera (SAP).

Kedua – duanya telah difakrikasi dan dinilai bagi pemilihan pam mikro terbaik untuk aplikasi di dalam unit POC. Semasa operasi kendiri, pam mikro SAP mempunyai kadar aliran yang lebih tinggi (Q = 49.9 µL/s) berbanding pam mikro MAPC (Q = 24.4 µL/s) menyebabkan ia telah dipilih untuk digabungkan dengan pencampur mikro Tesla dan disepadukan ke dalam unit POC. Pam mikro MAPC dan SAP ini juga didapati sesuai untuk dipasang pada saluran keluar pencampur mikro untuk mengatasi masalah kebocoran dalam rangkaian tiub unit POC. Kajian berangka melalui simulasi CFD telah digunakan untuk mengoptimumkan tekanan di dalam unit POC. Hasil daripada simulasi ini menunjukkan bahawa adunan cecair yang lengkap telah dicapai pada tekanan tolok -10 kPa. Simulasi CFD juga menunjukkan adunan cecair adalah berpunca daripada penjanaan vorteks Dean dan aruhan berbilang arah terjadi pada setiap peringkat injap Tesla. Tekanan tolok sebenar juga didapati lebih rendah daripada tekanan tolok simulasi serta berkurangan megikut masa disebabkan oleh limitasi fizikal gandang pam mikro SAP.

Kata kunci: *Pencampuran mikro, pengepaman mikro, point-of-care, pencampur mikro, pam mikro*

TABLE OF CONTENTS

LIST OF TABLES

LIST OF FIGURES

LIST OF ABBREVIATIONS

2D	Two-dimensional
3D	Three-dimensional
AOI	Area of Interrogation
ASSURED	Affordable, Sensitive, Specific, User-friendly, Rapid and robust, Equipment-free, and Deliverable to end users
CFD	Computational Fluid Dynamics
DNA	Deoxyribonucleic Acid
FD & C	Federal Food, Drug and Cosmetic Act (USA)
JCGM	Joint Committee for Guides in Metrology
MAPC	Multi Angle Paper-based Capillary
MI	Mixing Index
MHD	Magneto-hydrodynamic
MSTV	Multistage Tesla Valve
PCap-μPAD	Paper-based Capillary-empowered Micro-paper Analytical Devices
PCR	Polymerase Chain Reaction
PDMS	Polydimethylsiloxane
PMMA	Polymethyl Methacrylate
POC	Point-of-care
RGB	Red-green-blue
SAP	Sub-atmospheric Pressure
SAR	Split and Recombination
SEM	Scanning Electron Microscope

T45-R	Tesla Valve Model (Forster et al. (1995)
UV	Ultraviolet
WHO	World Health Organization
YCSAR	Y-shaped, Circle-split, and Recombination Micromixer

LIST OF SYMBOLS

β	Contact Angle of Material Surface with Liquid
γ	Interfacial Tension of Paper Matrix
η	Micropump Efficiency
μ	Fluid Dynamic Viscosity
ρ	Fluid Density
σ	Standard Deviation
b	Minimum or Maximum of Blue Pixels
g	Minimum or Maximum of Green Pixels
$\vec{g}$	Gravitational Acceleration
h	Elevation of a Point
h_B	Elevation of Point B in MAPC Micropump
h_T	Elevation of Point T in MAPC Micropump
n	Number of Pixels
r	Red
t	Time
$\vec{\mathbf{u}}$	Fluid Steady-state Velocity Field
v	Fluid Velocity
y	Minimum or Maximum of Yellow Pixels
A_{flow}	Cross-sectional Area of the Flow Path in the Paper Matrix
A_{CS}	Cross-sectional Area of the Microchannel in MAPC Micropump

D_{cap}	Effective Capillary Diameter
D_H	Hydraulic Diameter of Microchannel
L_b	Bias Limit
L_p	Precision Limit
N_{mixed}	Number of (Fully Mixed) Green Pixels
$N_{not\text{-}mixed}$	Number of Non-mixed Pixels
P	Fluid Pressure
P_{atm}	Atmospheric Pressure
ΔP	Micropump Gauge Pressure
$\Delta P_{simulation}$	Optimum Gauge Pressure Determined from CFD Simulations
ΔP_{actual}	Actual Gauge Pressure of Micropump
Q	Volumetric Flow Rate
Q_H	Hydrostatic-based Volumetric Flow Rate
Q_{PC}	Capillary-based Volumetric Flow Rate
Q_{MAPC}	Volumetric Flow Rate of MAPC Micropump
Re	Reynolds Number
U_m	Measurement Uncertainty
V_B	Fluid Velocity at Point B in MAPC Micropump
V_{cap}	Water Absorption Capacity
V_{CC}	Volume of Compressed Pump Chamber
V_T	Fluid Velocity at Point T in MAPC Micropump
V_{UC}	Volume of Uncompressed Pump Chamber
X_{MI}	Mean Value for Mixing Index
X_{Re}	Mean Value for Re

X_V	Mean Value for Electrical Potential
$\cap$	Boolean Operator for AND

CHAPTER 1

INTRODUCTION

1.1 Chapter Overview

This chapter provides a brief introduction to the application of microfluidic mixers and pumps in Lab-on-a-Chip (LOC) systems and point-of-care (POC) devices for biomedical usage. The background study and subsequently the focus and direction of this study are discussed in Section 1.2, with the problem statement concerning micromixing and micropumping will be covered in the subsequent Section 1.3. Section 1.4 elaborates on the study scopes, whilst the research questions are explained in Section 1.5. Finally, the research hypotheses, objectives, and thesis structure and summary are provided in Sections 1.6, 1.7, and 1.8, respectively.

1.2 Background Study

The application of microfluidics in life sciences and chemistry fields is actualized in LOC systems. Here, LOC systems generally comprise of a combination of microfluidic units such as microneedles, micromixers, microdispensers, microfilters, microseparators, microreactors, micropumps and microvalves by which these units are capable to carry out a complete laboratory analysis within a small sized platform and volume samples, and obtain analytical signal rapidly (Gurkan et al., 2024; Mukherji & Mondal, 2017; Nguyen et al., 2019; Ringkai et al., 2021a; Wang et al., 2020). Though with these advantages, LOC systems are still utilized as benchtop equipment in medical diagnostics laboratories. By reducing the complexity of equipment involved in the system, LOC can be simplified further in the form of passive POC devices. This simplification is said to be parallel to the requirements of Industrial Revolution 4.0 on telemedicine (Kost & Zadran, 2019), and the Sarawak Digital

Economic within its Digital Health sector (Ahmad et al., 2020; Wootton et al., 2017). In the recent years, microfluidic-based POC devices are developed as an alternative to the benchtop equipment and emerged as an influential technique that satisfies the ASSURED criteria (Affordable, Sensitive, Specific, User-friendly, Rapid and robust, Equipment-free, and Deliverable to end users) outlined by the World Health Organization (Hong et al., 2016; Pittman et al., 2023; Xu et al., 2020). Micromixer-based POC devices in bio-medical field are successfully utilized in the Lateral Flow Assay (LFA) and Nucleic Acid Tests (NAT) (Sachdeva et al., 2021). The overview on micromixers and micropumps in biomedical applications is shown in Figure 1.1.

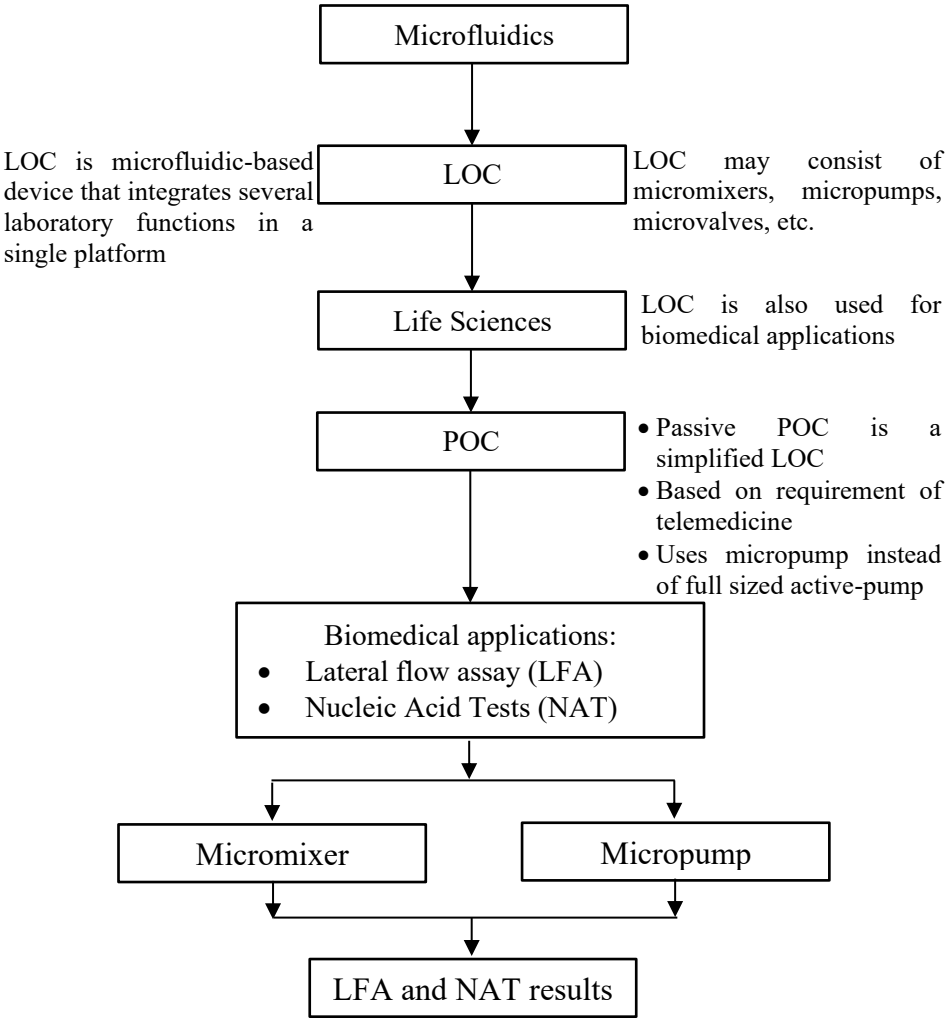

Figure 1.1: Overview of Micromixers and Micropumps in Biomedical Applications

Micromixer-based POC devices often integrates along several other microfluidic units including micropumps, microvalves, microreactors, etc. to accomplish the complete assay of bio-fluids on a single platform. Particularly in POC applications, active micromixers were found to be intricate as they are difficult to be transported and setup at a new location by less experienced laboratory personnels (Afzal & Kim, 2021; Kost & Zadran, 2019; Lee & Fu, 2018). Alternatively, passive micromixers are deemed to be more suitable, nevertheless, many studies on passive micromixers are generally focused on the elongated mixing channel to achieve complete fluid mixing through the technique of fluid layers lamination as shown in Figure 1.2 (Bayareh et al., 2020; Feng et al., 2021; Lv et al., 2022). For a shorter mixing channel, structured mixing channel in the form of two-dimensional (2D) or three-dimensional (3D) structures were introduced to give the same mixing performance (Afzal & Kim, 2021). 3D-structure passive micromixers however, must utilize precision fabrication techniques and equipment (Afzal & Kim, 2012, 2021; Alam et al., 2014).

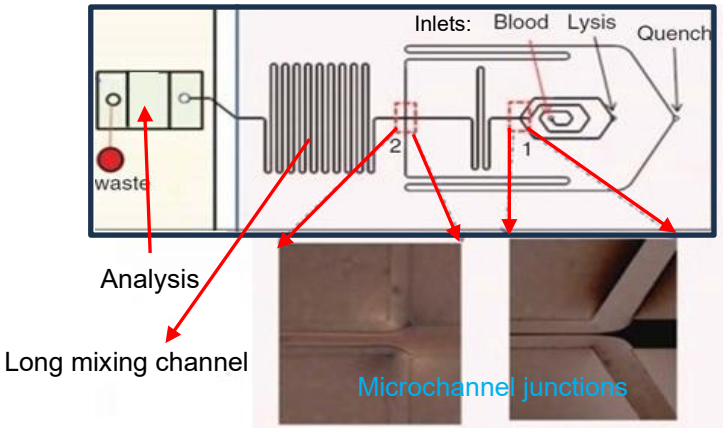

Figure 1.2: Schematic Diagram of Micromixer-based POC Device (Wang et al., 2020)

On the other hand, it was identified that LOC systems are mostly fixed as benchtop equipment, and utilizing a large and full-size active-driven benchtop such as syringe pumps or compressed air to drive fluid in the micromixer making them complicated for a rapid setup

and transportation (Lee et al., 2017; Liu et al., 2016; Petkovic et al., 2017). The benchtop pumps are also required to push fluid into the micromixer, hence higher working pressure than the ambient is used. This will make the tubing network to be prone to fluid leakage (Lee & Fu, 2018). Another problem will arise when the benchtop pumps are required to drive fluids into a micromixer with many inlets in which multiple units of benchtop pumps are needed to be separately attached to each inlet (Xu et al., 2020).

From the literature, it is also identified that characterizations on micropumps used in microfluidic system were only made onto a standalone micropump operation without integrating with any micromixers. Integrated micromixer-micropump unit for a successful liquid mixing has never been comprehensively studied (Holstein et al., 2016; Olanrewaju et al., 2018; Tian et al., 2018; Yamada et al., 2017). Accurate diagnosis of a microfluidic-based POC device is attributed to the mixing performance of the integrated micromixer-micropump unit. Thus, a comprehensive study on the micromixing performance of liquid and the micropumping performance are essential to be carried out.

1.3 Problem Statement

Lamination-based passive micromixers that are widely used in POC devices require a long mixing channel to achieve complete mixing of fluid or bioassays. Conversely, structured mixing channels in the form of two-dimensional (2D) and three-dimensional (3D) structures have been introduced as an alternative to achieve the same mixing performance but with a shorter channel length. Though with this advantage, 3D-structure passive micromixers and obstacle-based 2D passive micromixers must utilize precision techniques and equipment during fabrication. On the other hand, passive micropumps are preferable in POC devices to conventional benchtop active-driven pumps due to their portability, easy assembly, and setup. However, most literature only focused on the latter for driving fluid

within the device. These benchtop pumps are usually placed at the micromixer inlets hence multiple units are required to drive fluids into many inlets of a micromixer. Apart from that, running on these active-driven benchtop pumps may cause leakage in the device due to the higher working pressure than ambient. It is also identified that in the recent studies on micropumps, characterizations were made without the integration of micromixers. Hence, the integrated micromixer and micropump as a single POC unit to successfully actuate and mix fluid has never been comprehensively studied.

1.4 Study Scopes

The study scopes are:

i. Experimental investigation on liquid mixing performance in 2D-structure passive micromixers ($5 \leq Re \leq 40$) for utilization in POC

ii. Experimental investigation on flow rate performance of passive micropumps ($\Delta P < 0$ kPa, negative gauge pressure) for utilization in POC

iii. Numerical investigation in the form of CFD simulations within the scope of gauge pressure optimization for an enhanced mixing performance of the proposed POC unit

1.5 Research Question

The research questions are:

i. What is the suitable 2D-structure passive micromixer in terms of liquid mixing performance for utilization in POC?

ii. What is the feasible passive micropump in terms of flow rate performance for utilization in POC?

iii. How to optimize the integrated passive micromixer and micropump so that enhanced fluid mixing performance is achieved?

1.6 Hypothesis

The hypotheses are:

i. 2D-structure passive micromixer can be integrated in POC device only if a complete fluid mixing is achieved

ii. Passive micropump can be integrated in POC device only if a compatible flow rate is achieved

iii. Enhanced mixing performance of the integrated Tesla micromixer and sub-atmospheric (SAP) generating micropump can be achieved by determining the optimum gauge pressure

1.7 Objectives

The objectives of this study are:

i. To investigate the liquid mixing performance of 2D-structure passive micromixers for utilization in POC

ii. To investigate the flow rate performance of passive micropumps for utilization in POC

iii. To optimize the gauge pressure via CFD simulation for enhanced mixing performance in the proposed POC unit

1.8 Structure of Thesis

As an introduction to the thesis, Chapter 1 gives the general overview of the background study, problem statement, study scopes, research questions, hypotheses and the study objectives. Chapter 2 provides an in-depth review of the related literatures to identify the knowledge gap concerning the types of micromixers and micropumps used in POC devices. The discussion is generally based on the microchannel designs and micromixing techniques applied in those lamination-based, 3D-, and 2D-structures passive micromixers. From the wide variations of passive micromixers, the ones that utilize Dean vortex and fluid collision was selected and discussed further, such that found in passive micromixers with circular and Tesla-type mixing channel. In the following section, micropumps that generally used in POC are discussed, and focus was made into the micropumps specifically for the placement at the outlet of a micromixer. From a careful consideration, the designs that suits this application is identified to be the paper- and vacuum-based passive micropumps. In Chapter 3, the experimental method used in this study is detailed and segmented into sections based on the study objectives. To realize the first objective, the design and fabrication of micromixer with circular mixing channel and the Tesla-type micromixer were made, and their performances were compared. In the second section, the design, fabrication and performance comparison of the paper-based and vacuum-based micropumps were made to realize the second objective. For the third objective, CFD simulation was executed to optimize the integrated micromixer-micropump as a single POC unit prior the actual fabrication. CFD simulation was then verified with the actual experiment of the fabricated POC unit for validation. Next, the results and discussion based on the study objectives are

presented in Chapter 4, and the conclusion of the study and recommendations for future improvements is outlined in Chapter 5.

CHAPTER 2

LITERATURE REVIEW

2.1 Chapter Overview

This chapter reviews relevant literatures concerning the applications of microfluidic-based POC devices specifically on micromixers and micropumps to identify the knowledge gap. The discussion is generally based on the microchannel designs and micromixing techniques applied in those lamination-based, 3D-, and 2D-structures passive micromixers. From the wide variations of passive micromixers, the ones that utilize Dean vortex and fluid collision were selected and discussed further, such that found in passive micromixers with circular and Tesla-type mixing channels. Subsequently, various micropumps that generally used in POC were reviewed, and focus was made on micropumps specifically for the placement at the outlet of a micromixer. From a careful consideration, the designs that suits this application is identified to be the paper- and vacuum-based passive micropumps.

2.2 Micromixer in POC Devices

In biomedical applications, micromixer-based POC devices are successfully utilized in the lateral flow assay and nucleic acid tests (Sachdeva et al., 2021). Micromixers are majorly classified as either active or passive micromixers (Mahmud et al., 2020; Ringkai et al., 2021b; Yang et al., 2019). The overview of micromixers categories is shown in Figure 2.1. Active micromixers usually have simpler microchannel designs, but embedded with external auxiliary-energy drives such as sound, thermal, pressure, electrical and magnetic fields, to further enhance fluid mixing (Kim et al., 2018; Modarres & Tabrizian, 2020). Passive micromixer utilizes the fundamental concept of enhancing the diffusive effect between fluids by increasing the contact surface area between the mixing samples.

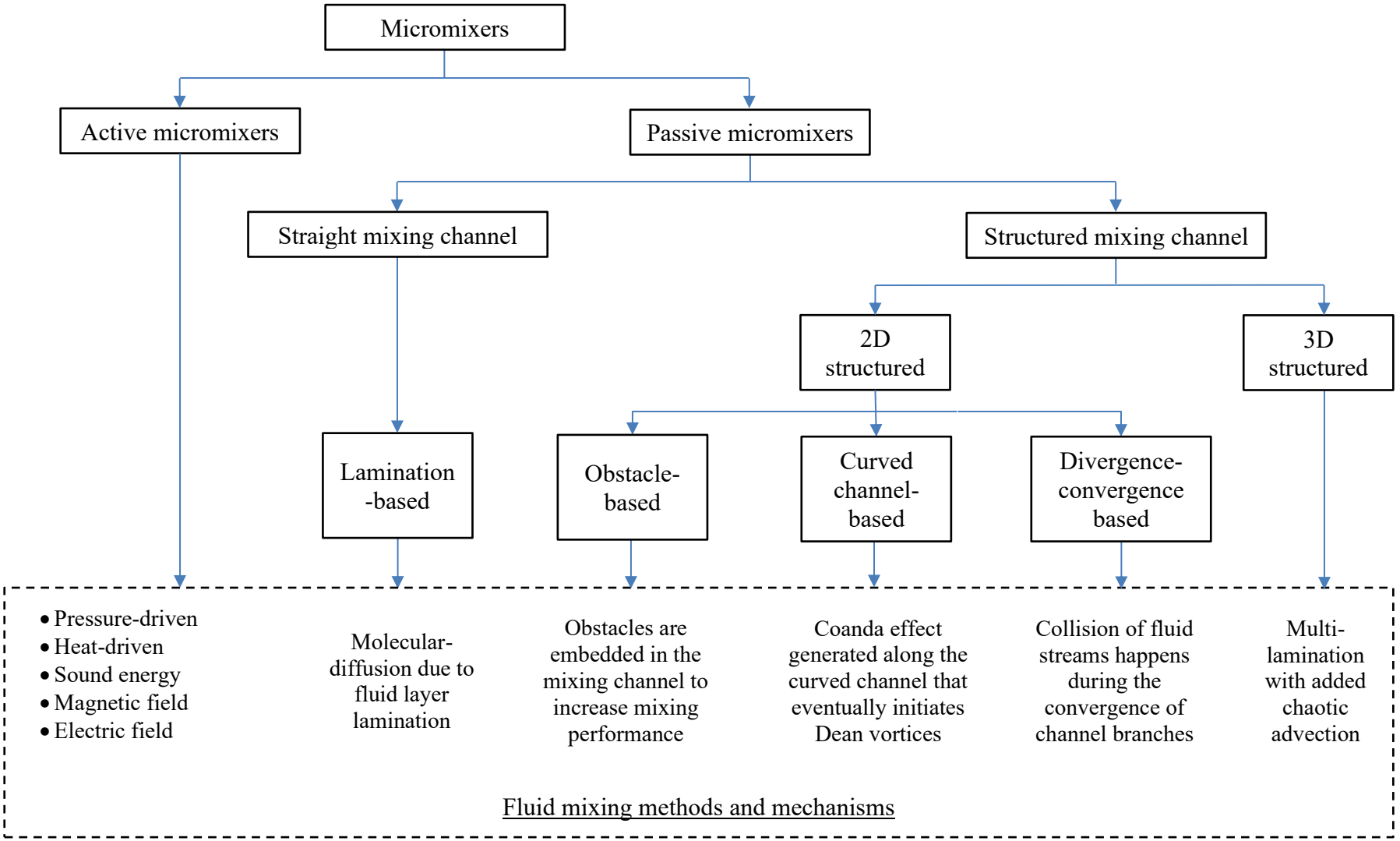

Figure 2.1: Overview of Micromixers Categories

2.2.1 Lamination-based Passive Micromixers

The most common and conventional design of lamination-based micromixers is the T- and Y-micromixers (Figure 2.2). Both micromixers are well known structures in which two liquid streams are injected into two separate inlets. The fluid flows are then combined in a straight mixing channel. In these designs, fluid mixing is primarily generated by molecular diffusion, which is considerably in a slow rate.

Mahmud et al. (2021) studied the mixing performance based on varying Re for T- and Y-micromixers. Mixing performance in terms of mixing index were observed at 10 mm after the inlets' junction for $5 \leq Re \leq 100$. Both micromixers were reported to achieve maximum mixing index no more than 35% at Re = 5, and it was significantly reduced after the Re was increased. Overall, the mixing performance was considerably low for both micromixers that were having a straight-line mixing channel. This low mixing performance in lamination-based micromixers can be addressed by using a long mixing channel to achieved a complete fluid mixing (Bayareh et al., 2020; Gobby et al., 2001).

Figure 2.2: (a) T-micromixer and (b) Y-micromixer (Mahmud et al., 2021)

Wong et al. (2004) investigated a conventional T-micromixer with straight-line mixing channel and T-micromixer with diamond step mixing channel. Different Re were used and the mixing performances were observed. Experimental results showed the liquid streams break up into striations at progressively higher Re. Through simulation, the fast liquid mixing was observed to be resulting from the generation of vortices at the diamond step junction due to flow circulation.

Rudyak and Minakov (2014) simulated the fluid movement at varying Re in the Y-micromixers to show the differences between a straight-line mixing channel and mixing channel with rectangular obstacles. In the latter, results showed that flow without vortex was generated at $Re < 5$. In $5 < Re < 150$, flow with two symmetrical vortices were observed.

Both Wong et al. (2004) and Rudyak and Minakov (2014) showed that, the microchannel geometry in T- or Y-micromixers must be manipulated to increase the fluids contact to increase the rate and efficiency of fluid micromixing. Proper geometrical manipulation in terms of 2D- or 3D-structures made the possibility to break, split, stretch and fold liquid, all of which are essential to increase micromixing performance in a passive micromixer, and therefore many studies based on these had been introduced in the recent years (Mahmud et al., 2020).

2.2.2 3D-Structure Passive Micromixers

3D-structure passive micromixers group consists of 3D-lamination, 3D-chamber, 3D-spiral and 3D-overidge based micromixers (Cai et al., 2017). Rafeie et al. (2017) designed and studied a novel 3D micromixer which incorporates the curved and fine threaded microchannels to induce the Dean flow and diffusive mixing, respectively. The micromixer maintains its high performance in a wide Re range, with efficiency of $\approx 93\%$.

Yang et al. (2015) studied both experiment and CFD simulation for flow and mixing characteristics of the developed 3D-structure Tesla micromixer for detecting antibodies binding reaction to recognize antigens of lung cancer. The CFD analysis via the steady 3D conservation equations of mass, momentum and species concentration was conducted to simulate the mixing behaviour. The results of the micromixer showed good mixing performance for $0.1 \leq Re \leq 100$.

Li et al. (2015) reported the development of a 3D-structure passive micromixer named the overbridge-shaped micromixer, that mixes liquid based on splitting, recombination, and chaotic advection mechanisms simultaneously. Up to a 90% mixing efficiency had been achieved within $0.01 \leq Re \leq 50$ by numerical analysis and experiments.

Though 3D-structure passive micromixers are capable to generate various combination of vortices such as second flow vortices, Dean vortices, and chaotic advection etc., to enhance mixing, they however are dependent on complex spatial structures, which require cumbersome and precision fabrication techniques (Cai et al., 2017). To add, fabrication of 2D-structure passive micromixers is much uncomplicated as compared to 3D-ones (Bayareh et al., 2020).

2.2.3 2D-Structure Passive Micromixers

2D-structure passive micromixers that utilizes the geometric manipulations of microchannel had been used recently for fluid mixing. It can be classified in the form of obstacle-based, curved channel-based, and convergence-divergence based mixing channels. These patterns were used to induce Dean vortices that eventually promotes chaotic advection in fluids (Mahmud et al., 2020).

Obstacles-based Micromixers

Obstacle-based micromixers are mostly combined with various embedded grooves or barriers with different shapes and heights in the mixing channels. Hossain et al. (2011) proposed a micromixer with staggered herringbone grooves on the top and bottom walls of its mixing channel. The channel was of 200 μm width and 77 μm depth and with total length of 8.5 mm. These groove obstacles were embedded to create a strong transverse flow with vortices in the fluid. The micromixer was optimized based on the geometric variables; the number of grooves, ratio of the groove depth to channel height, angle of grooves, and ratio of the groove width to pitch. Simulation results showed that the best mixing efficiency could reach up to 91.7%.

Wang et al. (2014) fabricated a passive micromixer containing 64 sets of grooves in the form of triangle barriers. Fluid mixing was improved with the increase of the triangles apical angle from 30 to 150°, and the quantity of triangle barriers. It was also reported that at Re = 1, mixing performance was 85.5% at the length of 6.4 mm of the mixing channel, which is approximately two-times performance improvement than the conventional T- and Y-micromixers.

Alam et al. (2014) presented a micromixer with obstacles in the form of cylindrical, diamond and hexagonal-shaped barriers for mixing water and ethanol within $0.1 \leq Re \leq 60$. The effects of cross-sectional shape, height, and placement of the obstacles on mixing performance and the pressure drop were evaluated. Simulated results showed the barriers were capable of generating secondary flows that subsequently produced high fluid mixing performance as compared to conventional T-micromixer.

Chen and Zhao (2017) optimized the design and layout of obstacles in a T-micromixer to increase mixing performance. Numerical analysis showed that the flow direction changed in a constant manner as a result of blocking by obstacles which later produced chaotic advection and increased the fluid mixing effectively. The multi-unit obstacle micromixer was reported to perform at 90% mixing efficiency for a wide range of flow rate as compared to T-micromixer.

Heshmatnezhad et al. (2017) numerically studied the transverse flow induced by triangle-shape obstacles for enhancing the interfacial area between two fluids. Simulation results showed that Dean vortices and recirculation of flow in the side branches and behind the triangle-shape obstacles were increased when triangle-shape obstacles were positioned at pre-mixing unit. The change of obstacles positions in the mixing channel and its aspect ratio became so obvious with the increased of Re.

Curved Channel-based Micromixers

Howell Jr et al. (2004) studied a curved-channel micromixer to generate Dean vortices during fluid mixing. High velocity streams were observed at the centre of the mixing channel. It is also identified that a greater centripetal force was generated when fluid is directed around a curve. These then created a pair of counter-rotating vortices moving towards the inner and outer wall of mixing channel. Dean vortices were becoming stronger as the Re increased.

Al-Halhouli et al. (2015) presented experiments results and computational simulations of curved channel-based micromixer designs that consisted of chains of interlocking semicircles and omega-shaped mixing channels aimed to generate Dean vortices in addition to molecular diffusion for enhancing fluid mixing performance at

different Re. At Re < 1, the mixing of two fluids is low and predominantly depends on the diffusion of fluid particles across the entire mixing channels. By increasing the flow rate further (Re > 1), the effect of Dean vortices and inertial forces becomes noticeable, and a rapid enhancement on the mixing performance was observed.

Shamloo et al. (2017) studied a curved-centrifugal micromixer for the application in Lab-on-a-Compact Disc. In this design, Dean vortices were induced due to the curvature of the mixing channel. Mixing performance was identified to be inversely proportional to the increment in angular velocity until it reaches a threshold of angular velocity (50 rad/s). Beyond this threshold, the secondary flow due to Dean vortices overcomes the molecular diffusion, and mixing performance begins to increase with angular velocity.

Convergence-divergence Based Micromixers

A convergence-divergence structure of micromixers can cause expansion vortices, subsequently causing a great disturbance to the laminar flow in the mixing channel, and increases the contact area between the fluid layers, thereby enhancing the mixing performance.

Wu and Tsai (2013) designed and studied a 2D micromixer with a converging–diverging cross section and semi-elliptical microchannel surfaces. Results showed that the fluid mixing is enhanced by the Dean vortices due to centrifugal force in the microchannel flow and the separation vortices was caused by the converging–diverging shape of the meandering channel.

Afzal and Kim (2015) proposed another design of convergent-divergent based micromixer with sinusoidal chambers under a periodic-time pulsing of inlet flows. The micromixer was reported to be capable of giving high mixing performance at a shorter length

of mixing channel. With pulsatile inlet flows, the design was said to achieve a 92% fluid mixing within two unit of the sinusoidal chambers.

Tran-Minh et al. (2014) proposed a convergent–divergent based micromixer operating in laminar flow for a continuous human blood mixing. With a split-and-recombination (SAR) channel pattern in terms of ellipse-like micropillars, the total length of mixing channel can be made shorter than a conventional T-micromixer for a complete fluid mixing.

Shah et al. (2019) had also improved the fluid mixing in SAR-type micromixers with the introduction of four types of mixing channel geometries, namely, Y-shaped straight SAR, Y-shaped circle SAR, Y-shaped rhombus-circle SAR, and Y-shaped rhombus SAR. Mixing in Y-shaped straight SAR mainly resulted from the molecular diffusion which was very low (≈ 15%). All three other geometries had shown an improved fluid mixing as compared to Y-shaped straight SAR due to the generation of flow rotation. Flow rotation was generated in the mixing channel due to the transverse flow produced during the fluid recombination and enhanced the fluid mixing performance as convection becomes dominant.

2.3 Micromixing Technique based on Dean Vortices and Fluid Collision

Coanda effect happens when a flowing fluid tries to keep attached to a curved surface similar to the aerofoil effect on aircraft wing. The physical tendency of fluid layers to continually attached onto a curved surface resulting to a curving motion of fluid stream (Hong et al., 2004; Hossain et al., 2010; Liu, 2000; Stroock et al., 2002) that eventually produces pressure imbalance that subsequently leads to secondary flows to form counter-rotating flows, known as Dean vortices (Nivedita et al., 2017). On the other hand, a transverse flow that is not attributed from Coanda effect can also be generated by the splitting

and recombination of fluid flow. This also causes flow rotations that eventually generates Dean vortices (Shah et al., 2019).

In contrast to a transverse flow, a complete reversed direction flow can also be useful for fluid mixing, and may have greater effect than a transverse flow. In the reversed flow, fluid is recombined back from the secondary channel to main channel in a completely reverse and opposing direction to the fluid flow in the main channel that subsequently generates fluid collision.

Integrated effect of Dean vortices and fluid collision can be beneficial for generating chaotic advection-based fluid mixing. This is advantageous for an effective fluid mixing, and such method can be found in micromixers with circular mixing channel and Tesla-type micromixer. In micromixers with circular mixing channel, Dean vortices and fluid collision are created by the curved or circular-shape mixing channel (Alam & Kim, 2013), while in Tesla-type micromixers, they are created majorly by the reversed flow exited from the helix branch channel (Wang et al., 2021).

2.3.1 Micromixer with Circular Mixing Channel

Micromixers with circular mixing channel provide multi-lamination of fluid layers that subsequently enlarges the inter-contacting surfaces. Mixing channels in the form of circular-shape chambers with added constriction or chocking provide fluid recirculation within the chamber which in turn is significant for mixing. Fluid rotation or recirculation is effective at large range of Re.

Chung et al. (2004) introduced designs of micromixer with circular mixing channel (in the form of mixing chambers) for generating self-circulation of fluid to improve the mixing performance. Figure 2.3 shows the proposed micromixer designs that having mixing

channels in the form of circular and annular chambers. Once fluid flowed into the mixing chamber, it was separated into the main flow and circulating-secondary flow (Figure 2.4). Within the secondary flow streams, vortex was formed due to the velocity different of the outer and inner flow streamlines, and eventually increased the contact area which then improves the fluid mixing. Their results showed that micromixer with hollow chamber was more suitable for operating at $20 \leq Re \leq 400$ as compared to annular chamber micromixer.

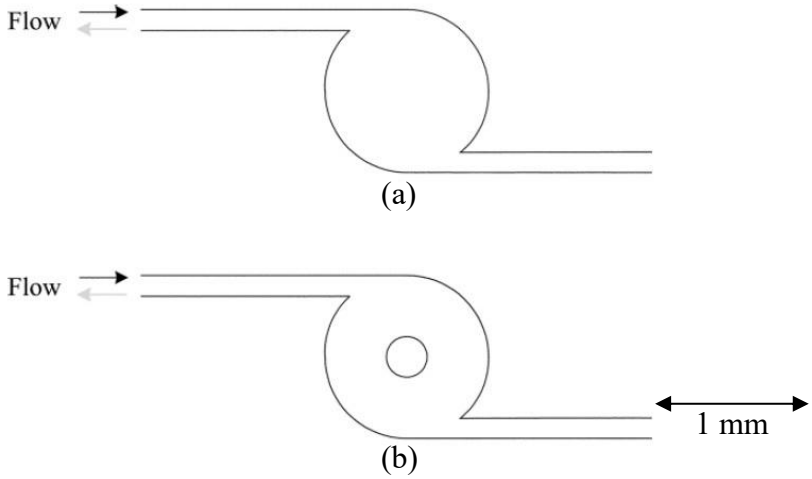

Figure 2.3: Micromixer with; (a) Hollow-circular Chamber, and (b) Pillar-annular Chamber (Chung et al., 2004)

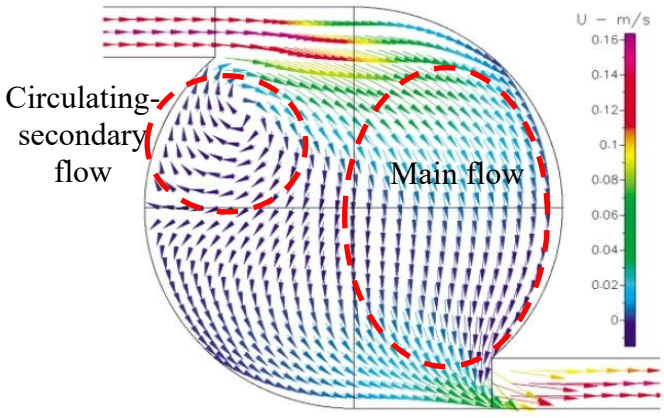

Figure 2.4: Fluid Circulation in the Mixing Chamber (Chung et al., 2004)

Ansari et al. (2010) investigated a micromixer that was designed based on the annular-chamber micromixer, first introduced by Chung et al. (2004), but with the added concept of unbalanced splits and cross collision of fluid streams (Figure 2.5). The main channel was split into two unequal widths sub-channels and then recombined after a certain distance in a repetitive fashion. It was identified that the difference in the inertia of the fluid flow in the split channels by the unequal widths creates an unbalanced collision, which perturbs the flow and shifts the interface of the fluid streams into the sub-channel where Dean vortices become effective in enhancing mixing, which is very effective for mixing as compared to a balanced collision.

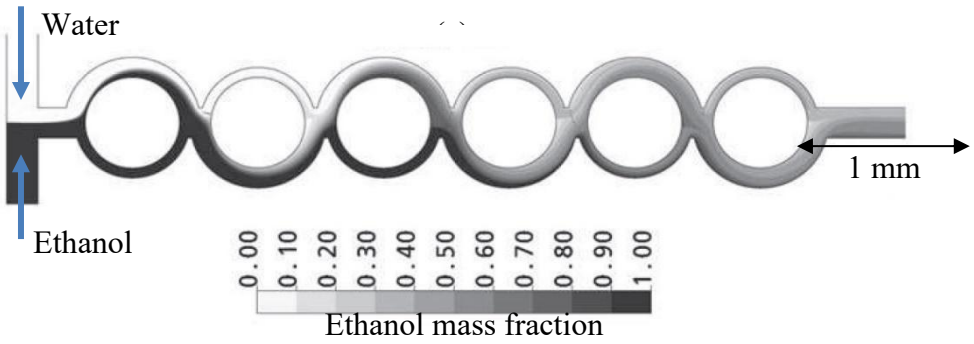

Figure 2.5: Annular-chamber Micromixer with Unbalanced Splits and Cross Collision of Fluid Streams (Ansari et al., 2010)

Alam and Kim (2013) proposed a planar micromixer design with circular mixing chambers and two constriction channels crossing and overlapping each other to connect adjacent mixing chambers as shown in Figure 2.6. The design used the techniques of fluid recirculation and split-and-recombination to improve mixing performance. The micromixer performance was compared to the design variations that was based on annular-chamber micromixer introduced by Chung et al. (2004). In the low Re range ($Re \leq 10$), the diffusional contacts area of fluid layers became much larger due to the distributions of the mass fraction

of ethanol changed alternatively in subsequent circular chambers resulting from the split-and-recombine of fluid. In higher Re (Re > 10), two symmetric counter-rotating flows were formed in the central region of the circular chamber. However, the strength of these two symmetric recirculating flows was not greater than that of the single recirculating flow that occurred in the circular chambers with a single constriction channel. Therefore, the micromixer was proposed to be used in Re ≤ 10 so that excellent mixing performance can be produced.

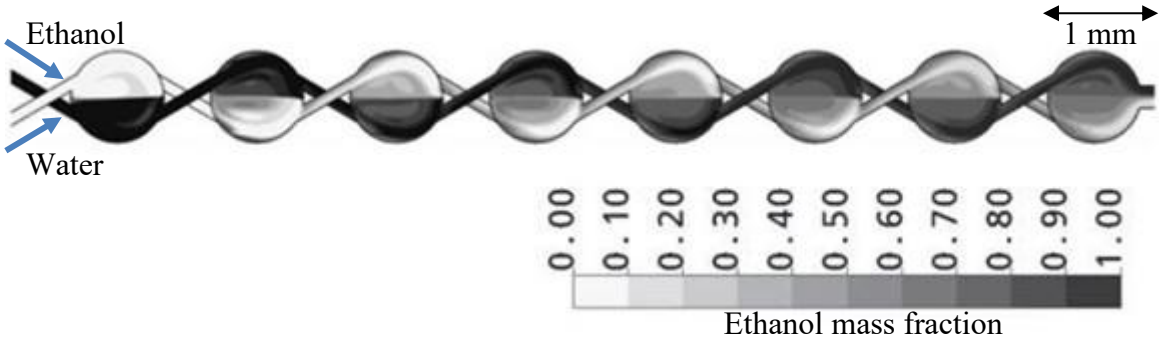

Figure 2.6: Micromixer with Circular Mixing Chambers and Inter-connecting Channels (Alam & Kim, 2013)

2.3.2 Tesla-type Micromixers

Conventional and full-size Tesla valve is best known for its no-moving-parts, passive operation and fluid flow control. In microfluidic applications, the full-size valve can be made smaller and utilized as micromixers (Figure 2.7).

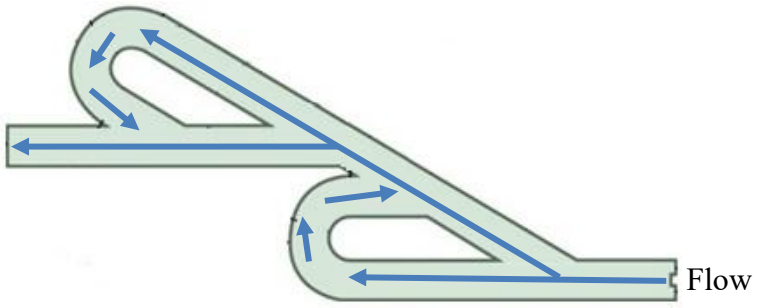

(a)

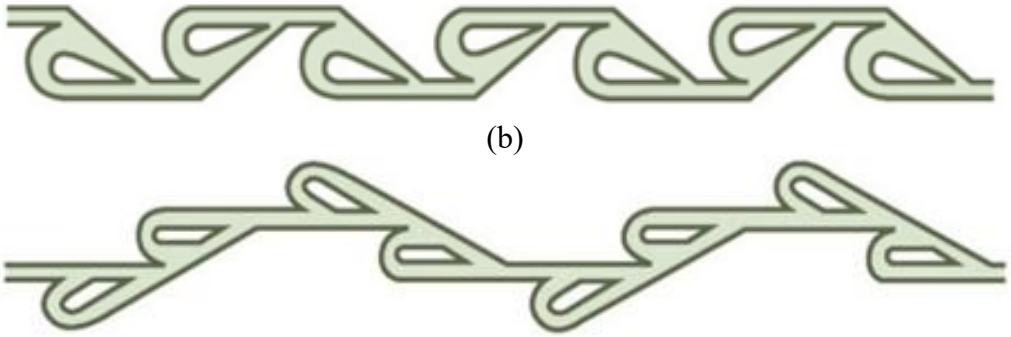

(b)

(c)

Figure 2.7: (a) Two Unit of Reversed Tesla Valves Placed in Series, (b) Multi-stage Reversed Tesla Valves Arrangement Type-1, and (c) Type-2 (Weng et al., 2021)

Forster et al. (1995) had introduced an original study about of Tesla valve intended for microfluidics (Forster et al., 1995). The valve was having a square cross section of 100 x 100 μm^2 and named as the T45-R valve with the angle between the helix and trunk is at 45°. A common attribute of any Tesla-type valves is their diodicity performance. It is defined as the ratio of pressure drop between reversed and forward fluid flows for a corresponding flow rate. Findings of the study shows that in laminar type of flow (Re < 300), Diodicity performance for the Tesla valve type T45-R was linearly increased with flow rate. Further, (Truong & Nguyen, 2003) performed 2D steady-state CFD analysis onto the Tesla valve T45-R to further investigate flow behaviour.

Gamboa et al. (2005) optimized further the Tesla valve T45-R geometry and demonstrated that helix-to-trunk angle of 45° and above performed 25% more efficient than the original version. Based on the optimization, the return angle of the helix of the valve was found to be larger than the original valve introduced by Tesla. Increasing this angle resulted in helix flow opposing the main channel flow, in turn introducing a fluid velocity opposite to the pressure gradient in the main channel, an important factor for maximizing fluid diodicity. Zhang et al. (2007) found that a square channel yielded maximum Di for low Re

(Re < 500), and a linear relationship was shown between aspect ratio and higher Re by 3D simulations on T45-R valve.

In the recent years, several numerical studies had been conducted to evaluate key design features on flow characteristics of the Tesla valves stacked in series or multi-stage Tesla valve (MSTV). The flow controlling effect of MSTV is amplified by spatially arranging multiple valves in series, thus forming multiple stages. For obtaining maximum fluid diodicity with increasing Re, the addition of more Tesla valves was suggested.

Mohammadzadeh et al. (2013) studied the performance of the MSTV as a function of diodicity and discovered that the diodicity increases with the increase of Re. They also performed unsteady simulations on MSTV with pulsating inlet flows for determining their flow-rectifying ability. This particular MSTV design consisted of 'high-angled' valve-to-valve connection schemes.

Thompson et al. (2014) evaluated the diodicity of MSTV for laminar flows by 3D CFD investigation with the 20-stage Tesla valves at Re ≤ 200. The diodicity of the MSTV was found to be proportional to Re. For low Re < 50, the diodicity was shown to be independent of number of valves used. For obtaining maximum fluid diodicity with increasing Re, addition in the number of Tesla valves and minimization of valve-to-valve distance was suggested.

Porwal et al. (2018) studied the flow rectification and thermal enhancement capabilities of a single and 10-stage Tesla valve for their potential to function as heat micro-exchanger in the aerospace applications. Their simulations demonstrated that the recombination of fluid from the helix and main channel introduces the colliding-reversed

flow as shown in Figure 2.8. The valve effectiveness was increased through the placement of multiple valves arranged in series that subsequently improved fluid diodicity.

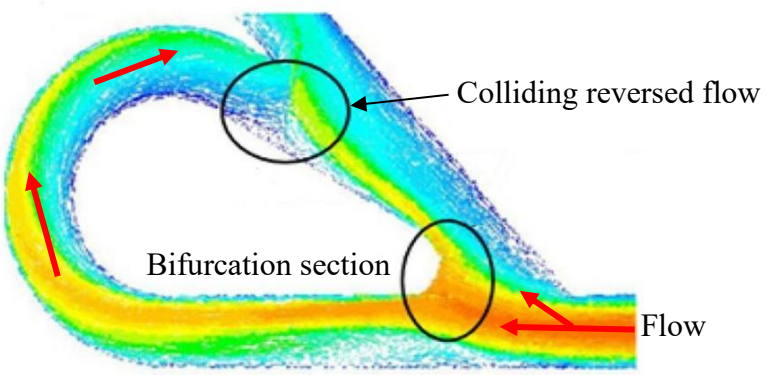

Figure 2.8: Colliding Reversed Flow in Tesla Valve (Porwal et al., 2018)

Qian et al. (2019b) numerically showed the flow of Al_2O_3-water nanofluids driven through a Tesla valve type T45-R (Figure 2.9). Pressure drops and fluid diodicity, flow rate, temperature, and volume fraction in the bifurcated section were investigated. Results showed that the jet flow from the helix branch channel influences the pressure drop significantly, leading to a larger pressure drop and fluid diodicity changed almost linearly with the supplied flow rate. Results showed that major fractions of fluid were passed into the helix than the main channel resulting from the orientation of bifurcation section. The mass fraction in the helix channel was larger as compared to the main channel as fluid tend to maintain its momentum direction, which made it mostly flow straight into the helix channel. At the converging junction of helix and main channel, the recombination of fluid gives a colliding flow in a transverse direction to the main flow.

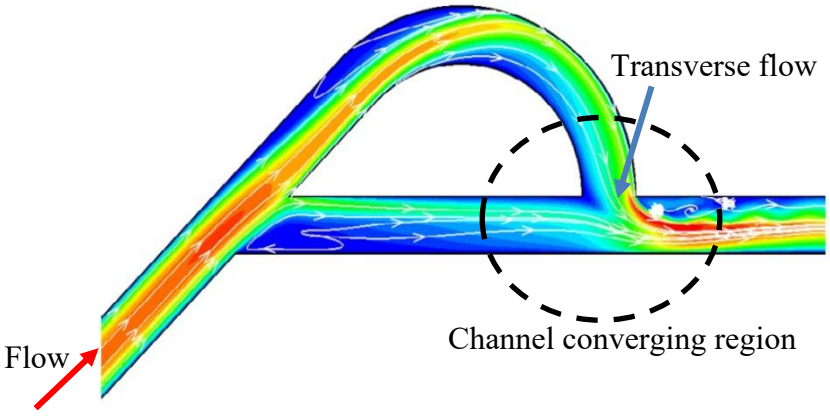

Figure 2.9: Transverse Flow in The Helix-to-main Channel Converging Region of a Tesla Valve

Qian et al. (2019a) simulated the hydrogen flow through multi-stage Tesla valves. Highly pressurized hydrogen is usually used to promote the recharge mileage. Decompression of hydrogen is needed before it flows into the fuel cell as a relatively lower pressurized hydrogen is required so that for fuel cell can functioned appropriately. Large pressure drops between the inlet and outlet of a Tesla valve could be successfully used for hydrogen de-compression. In this study, pressure and the velocity within the Tesla valves decreased once the valve stage was increased. As hydrogen flows toward the outlet, pressure was reduced progressively at each valve stage. Meanwhile, fluid collision in the form of jet flow impingement appeared after the intersection of helix to main channel at each stage (Figure 2.10).

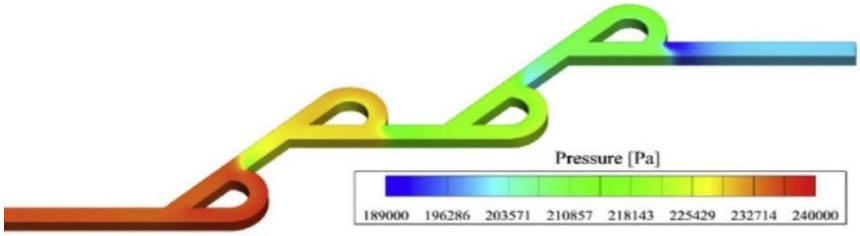

Figure 2.10: Pressure Distribution in a Single Tesla Valve by Qian et al. (2019a)

2.4 Micropumps in POC Devices

Incorporation of micromixers in POC devices often integrates along several other microfluidic units including micropumps to accomplish the complete assay of biomaterials on a single platform. Micropumps can be loosely categorized into either actively or passively driven (Wang & Fu, 2018). Active-driven micropumps utilise the auxiliary power to drive and control either by using mechanical actuators; (electromagnetic, electrostatic, thermos-pneumatic, shape memory alloy, electro-active polymer), or non-mechanical actuators; (electro-hydrodynamic, electroosmotic, magneto-hydrodynamic, electro-chemical) (Dereshgi et al., 2021). These however comes with the expense of a more sizeable and complicated components as compared to passive-driven ones (Wang & Fu, 2018). On the other hand, passive micropumps are further classified based on their fluid pumping method of either direct pressure-based, capillary-based and air transfer-based (Xu et al., 2020). The overview of micropumps categories is shown in Figure 2.11. In this study, a micropump placed after the micromixer is designated as post-micromixer placement and the vice versa as pre-micromixer placement.

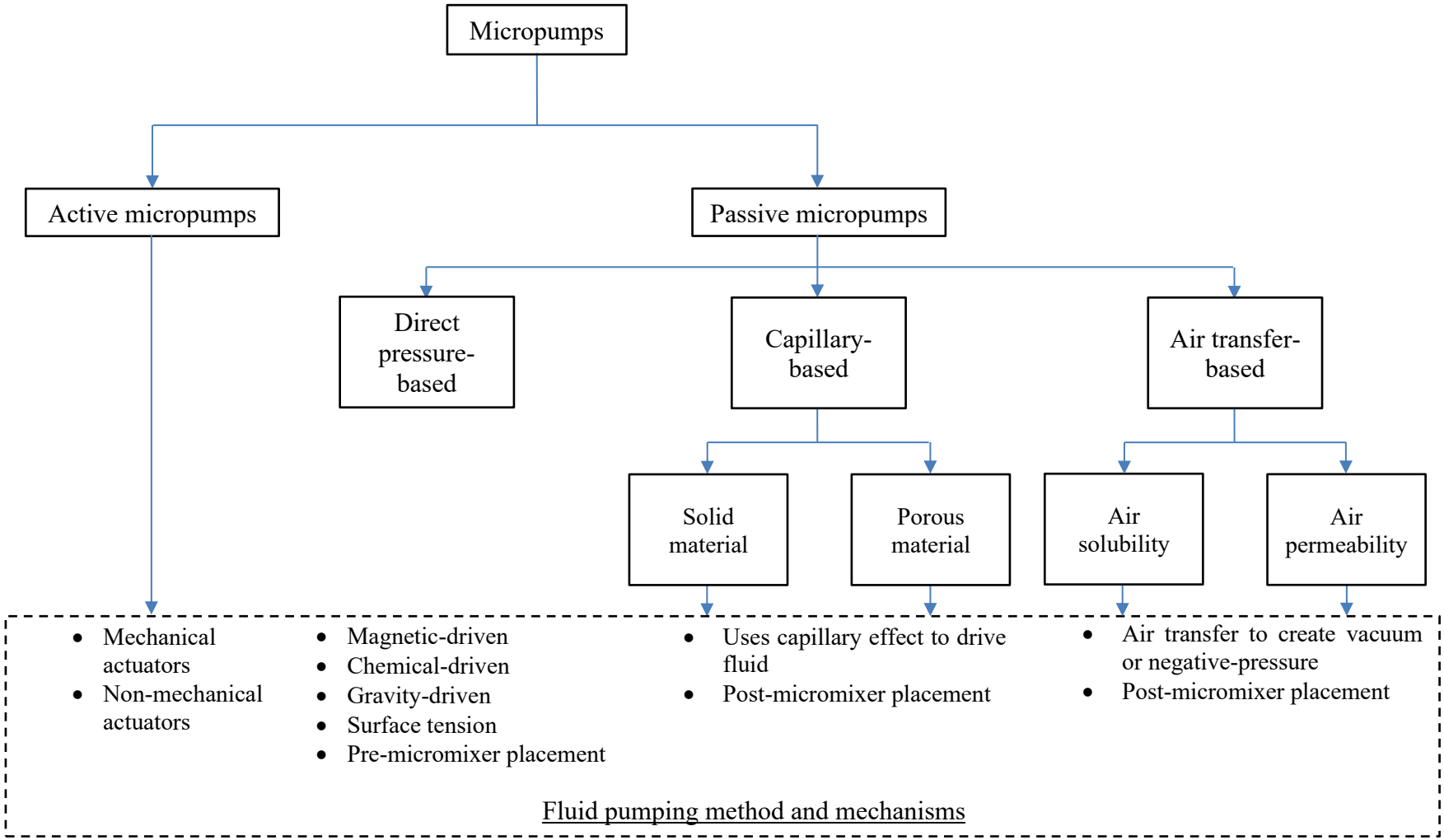

Figure 2.11: Overview of Micropumps Categories

In the studies on micropumps, it is also identified that the characterizations were made onto standalone pump operation without incorporating along with any micromixers (Table 2.1).

Table 2.1: Overview on the Studies on Micropump

No.	Author (year)	Micropump Design	Integration with Micromixer
1.	Hitzbleck et al. (2011)	Capillary-based	No
2.	Gervais et al. (2011)	Capillary-based	No
3.	Safavieh and Juncker (2013)	Capillary-based	No
4.	Xing et al. (2013)	Capillary-based micropump	No
5.	Nilghaz et al. (2013)	Capillary and multi filament threads-based	No
6.	Holstein et al. (2016)	Paper-based	No
7.	Yamada et al. (2017)	Paper-based	No
8.	Olanrewaju et al. (2018)	Capillary-based	No
9.	Tian et al. (2018)	Paper-based	No

The overall performance of a micromixer-micropump based POC device is attributed to the integrated performance of the individual micromixer and micromixer. Thus, it is essential to comprehensively investigate the liquid mixing and micropumping performances for the integrated micromixer-micropump unit of this present study.

2.5 Passive Micropumps for Post-micromixer Placement

From the previous literatures (Table 2.1), most studies were generally focused on the fluid mixing performance of the LOC system, and a fixed benchtop equipment that utilizing active-driven pumping such as the syringe pumps were used. The overview on the micromixer-micropump-based LOC system for biological analytical processes is presented in Table 2.2.

Table 2.2: Overview on the Micromixer-micropump-based LOC System for Biological Analytical Processes

No.	Author (year)	Integrated LOC System		Function
		Micromixer	Micropump	
1.	Nason et al. (2011)	Zig-zag shaped mixer (passive)	Active syringe pumps	Drug screening
2.	Jung et al. (2011)	Serpentine 3D mixer (passive)	Active syringe pumps	Multiplex pathogen detection
3.	Limu Wang et al. (2012a)	Ribcage mixer (passive)	Active syringe pumps	Protein concentration measurements
4	Choi et al. (2012)	Multi-layer mixer (passive)	Active pneumatic pump	PCR-microarray system
5.	Balbino et al. (2013)	Vortex mixer (passive)	Active syringe pumps	Produce pDNA/CL complexes
6.	Lounsbury et al. (2013)	Serpentine mixer (passive)	Active syringe pumps	PCR system
7.	Li et al. (2013)	Dual-focusing mixer (passive)	Active syringe pumps	DNA–protein interaction
8.	Wang et al. (2013)	USCC mixer (passive)	Active syringe pumps	Bacteria detection and quantification
9.	Lin et al. (2014)	Bubble-driven mixer (active)	Active syringe pumps	Bladder cancer biomarker detection
10.	Geissler et al. (2014)	Air stream mixer (passive)	Active syringe pumps	DNA-hybridization assays
11.	Rajabi et al. (2014)	SAR and SHM mixer (passive)	Active syringe pumps	Cell perturbation, lysis, and separation
12.	Aguirre et al. (2015)	Trapezoid type mixer (passive)	Active syringe pumps	blood Incubation and separation cancer cell
13.	Femmer et al. (2015)	SHM mixer (passive)	Active syringe pumps	Gas-liquid contact oxygenation device
14.	Cosentino et al. (2015)	3-SERP mixer (passive)	Active syringe pumps	Red blood cell lysis
15.	Gao et al. (2015)	Acoustic mixer (passive)	Active syringe pumps	Antibody-antigen binding assay
16.	Liu et al. (2016)	3D U-type mixer (passive)	Active syringe pumps	Analysis of bio-macromolecules folding kinetics

Table 2.2: continued

17.	Lee et al. (2017)	Multivortex mixer (passive)	Active syringe pumps	Isolation of circulating tumour cells
18.	Petkovic et al. (2017)	Rotary mixer (active)	Active vacuum pump	Detection of Hendra virus

In these studies, pumps are placed at the inlets of a micromixer (pre-micromixer placement), and used to push fluid using a considerably higher working pressure than the ambient. This setup will make the whole assembly to be prone to fluid leakage. Another problem arises when the pumps are required to drive fluids into many inlets of a micromixer by which multiple units of pumps are required to be separately attached to each inlet.

Hence, based on these shortcomings, a micropump placed at the outlet of a micromixer is best used to address these problems. Such micropumps are represented by the capillary- and air transfer-based micropumps. These micropumps are usually placed at the outlet of a micromixer (post-micromixer placement).

2.5.1 Paper-based Micropump

Some porous materials such as cotton yarn, wool, polyester and paper have been used for capillary-based pumping. The paper-based platform is deemed promising as the size can be minimized and it is easily disposable.

Kokalj et al. (2014) introduced a paper-based capillary micropump that operated on the drawing-in of working into paper matrix upon activation by fingertip press. The flow rate was controlled by manipulating the type, shape and size of the paper matrix, and the geometry of the microchannel. Paper matrices were cut in the shapes of circular sectors with different central angles θ of 20°, 40° and 60° (Figure 2.12), but each paper matrices having the same overall volume in order to preserve the same pumping energy. It can be understood

that when the liquid was absorbed into a homogenous and isotropic material such as paper, the radius-time dependence would remain the same for any circular section of this material. However, flow rate will not remain constant, but indeed having a linear dependence on central angle, with a larger θ, gave a larger the pumping power. However, problem was identified in paper material due to the unavoidable interaction of biological sample with its cellulose fibres, thus making it incapable to transport cells.

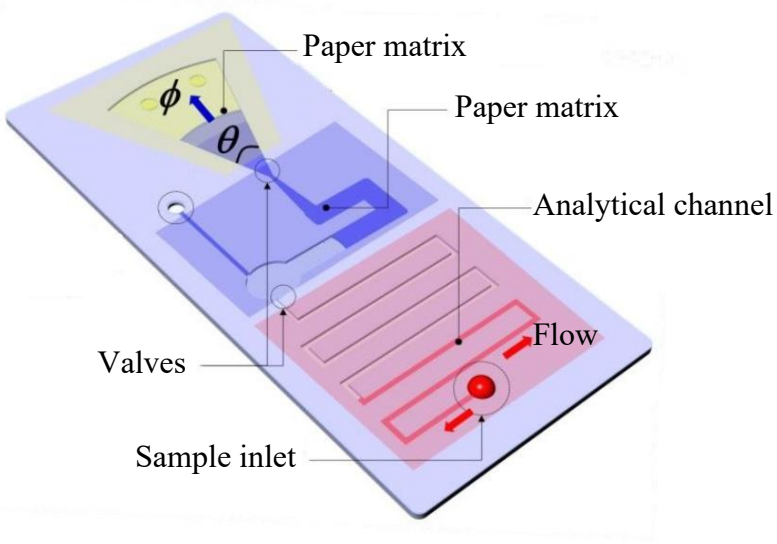

Figure 2.12: Schematics of Self-powered Imbibing Microfluidic Pump (Kokalj et al., 2014)

Shangguan et al. (2018) proposed a paper-based capillary-empowered micro-paper analytical devices (PCap-μPAD) that was having a robust flow control to accommodate a high-quality analysis of samples (Figure 2.13). The design was taking advantageous from the fast sampling with low surface adsorption and homogenous sample distribution. These specialties have facilitated repeatable and reliable sample analysis for ions and large molecules. However, some problem was found where the fluid movement was more intricate to control as compared to a conventional microfluidic channel. The undesirable low flow

rates in paper-based micropumps usually lead to longer surface adsorption time of samples which was inefficient for sample transportation.

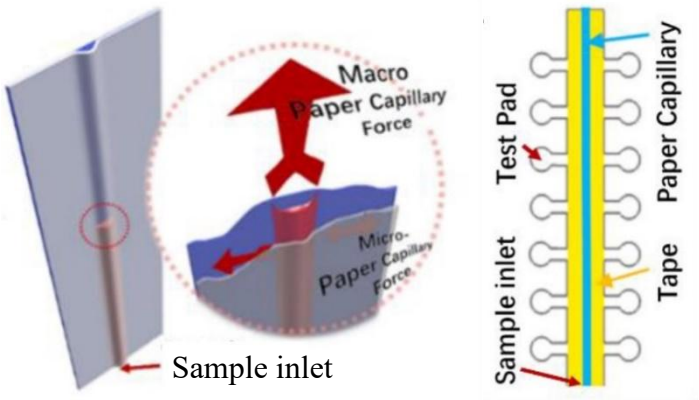

Figure 2.13: Illustration of PCap-μPAD (Shangguan et al., 2018)

2.5.2 Vacuum-based Micropump

Air-transfer based micropumps use the capabilities of material to store or allow vacuum to be transferred later for micropumping. Material with good air permeability allows air trapped which can be diffused into the adjacent pneumatic chamber where a vacuum is stored; thus, negative pressure is generated inside the microchannel. These micropumps were presented in studies such that found in Liang et al. (2011) and Begolo et al. (2014), which are promising for the application in the POC device.

Liang et al. (2011) showed that Polydimethylsiloxane (PDMS) based degas-driven flow was capable to be used as a micropump without requiring any external power. This method took advantage of the inherently high porosity and air solubility of PDMS by removing air molecules from the bulk PDMS before initiating the flow (Figure 2.14). Investigation was done on the effects of channel cross-sectional area, channel surface area, PDMS thickness, PDMS exposure area, degas time and post-vacuum idle time, on fluid flow velocity and channel filling time. It was found that with the 4.1 mm thick, and a channel width and height of 50 μm, the micropump degas time was completed in about 45 min. The

maximum flow velocities were ranging within 0.2 to 3 nL/s, depending on the design geometries.

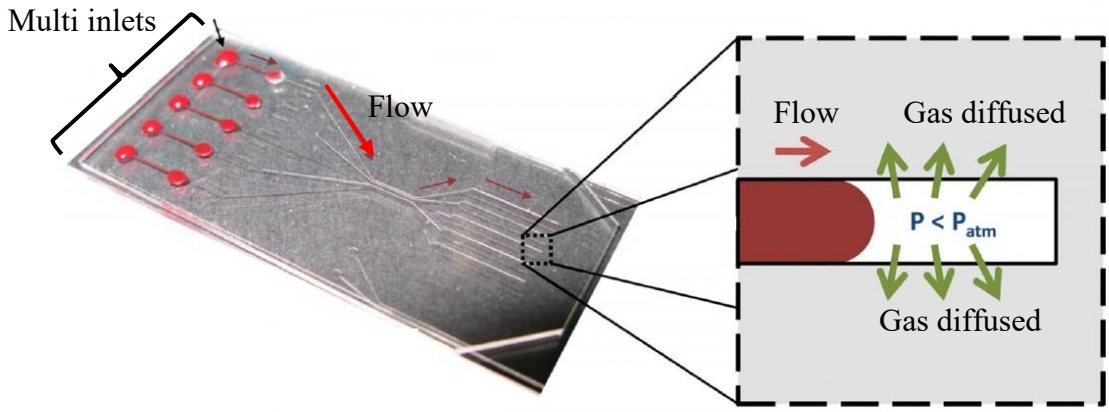

Figure 2.14: Micropump Based on PDMS Degas-driven Flow by Liang et al. (2011)

Begolo et al. (2014) introduced the pumping-lid micropump that was based on the controlled compression or expansion of gas (Figure 2.15). The micropump was capable to generate both positive and negative pressures, and also able to handle complex fluid manipulation such as stable long-term laminar flow of multiple samples. The pumping lids were capable to produce predictable negative pressure via controlled expansion of gases. Both positive and negative pressures were pre-programmed by the geometry of the parts and could be tuned further even while the experiment was in progress.

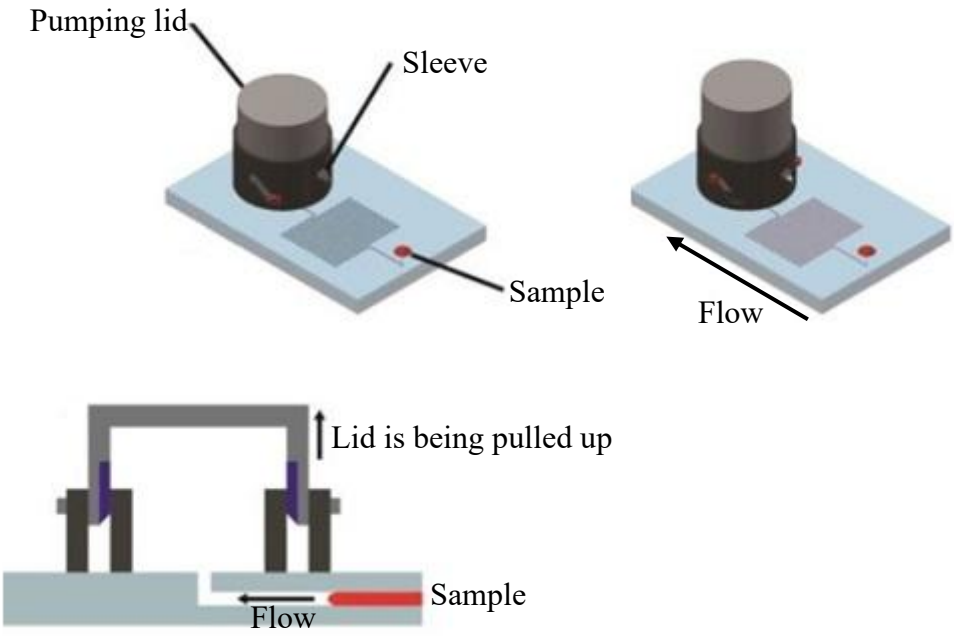

Figure 2.15: Pumping Lid as Micropump by Begolo et al. (2014)

2.6 Gauge Pressure Optimization

Wang et al. (2021) studies the mixing performance and pressure drop in Tesla micromixers with and without the embedment of diamond obstacle. The effect of the location and diamond sizes was studied, and the diamond-shaped barrier Tesla has higher mixing rate as compared to the one without obstacles under the same conditions. Pressure drops were found to be increased with the size of obstacle due to the reduction of area through which the fluid passes resulting to an increase of internal pressure. The flow through the Tesla micromixer was assumed to be;

i. Steady state, laminar and incompressible
ii. No-slip condition at the boundary
iii. Single phase flow and constant fluid properties with negligible viscosity dissipation
iv. Negligible gravity effects as flows perpendicular to gravity

Chen and Zhao (2017) numerically optimized the layout of obstacles in a 3D micromixer. Numerical analysis shows that the direction of flow velocity change constantly due to the obstacles blocking, which produces higher pressure drop and increased fluid mixing effectively. The CFD simulations used standard mass continuity (Equation 2.1) and momentum balance (Equation 2.2) for Newtonian fluid as the governing equations for fluid continuity and momentum, where $\vec{\mathbf{u}}$ is the fluid steady-state velocity field.

$$\frac{\partial \vec{\mathbf{u}}_j}{\partial x_j} = 0 \qquad \text{Equation 2.1}$$

$$\rho \vec{\mathbf{u}}_j \frac{\partial \vec{\mathbf{u}}_l}{\partial x_j} - \mu \frac{\partial^2 \vec{\mathbf{u}}_l}{\partial x_j \, \partial x_j} + \frac{\partial P}{\partial x_l} = 0 \qquad \text{Equation 2.2}$$

Kelley et al. (2020) showed that the mesh independence study is used to verify the number of grids used in the calculation is not affecting to the simulation results in steady-state flow. Although denser grid points will give more accurate result, the number of grids must not be overly dense as larger and longer calculation period is required.

dos Santos et al. (2019) mentioned that the simulations results must not change significantly with further refinement of the mesh so that mesh independence can be achieved. This can be realized by running simulations with progressively finer mesh, and results are then plotted against the mesh size to observe the convergence.

Gamboa et al. (2005) presented a CFD optimization of a fixed-valve micropump with Tesla element. A significant increase in gauge pressure was of three times higher as compared to an identical pump with non-optimized Tesla valve over the Reynolds number range of $0 \leq Re \leq 2000$. The large performance increase observed demonstrated the importance of valve shape optimization in the overall design process for fixed-valve

micropumps. It was also concluded that the optimization of gauge pressure can be achieved by optimizing the shape of Tesla valve, or the addition of multiple Tesla valve element in series.

Guo et al. (2018) numerically demonstrated the optimized gauge pressure of a passive hydrostatic-based ram pump for applications in fountain sight and irrigation. The study proposed four indexes of evaluation, namely; head loss coefficient, drag coefficient, eccentric distance of pressure on the waste valve, and velocity distribution uniformity of the outlet, to optimized the ram pump design. Calculation model and parameters, mesh generation and boundary conditions related to the numerical simulation are presented.

Porwal et al. (2018) presented the significant effects of a single and multiple Tesla valves onto pressure drop and fluid diodicity in their study of a 10-stage Tesla micromixer. CFD simulations showed that valve effectiveness was increased in terms of pressure drop and subsequently the diodicity of fluid, by the placement in series a multiple element of Tesla valves.

Zhang et al. (2023) numerically studied the effects of the variation of the flow channel width-to-narrow ratio onto flow performance of the Tesla micromixer. It was aimed to optimize the geometry and pressure drop within the micromixer so that high performance flow control was achieved. Result showed the proportion of flow rate occupied by the arc channel does not increase with the increase in the width-to-narrow ratio. Its maximum proportion of flow rate mainly occurs in the width-to-narrow ratio = 0.4 and 0.6. As the width-to-narrow ratio decreases, the pressure drop became greater, and the pressure change is most pronounced in the case of width-to-narrow ratio = 0.2. The change in flow channel in the low width-to-narrow ratio range (0.2 to 0.4) significantly affects fluid flow, flow rate distribution, pressure drop characteristics, and vortex distribution.

2.7 Chapter Summary

In short, the microfluidic units applicable to POC devices are reviewed, namely micromixer and micropump. The designs, methods of fabrication, and applications of both systems have been presented in the relevant sections of this chapter. Selection of the possible candidates for this present study is based on the deduction from each section of literature on micromixer and micropump, and summarized as in Table 2.3.

Table 2.3: Summary on the Problem Statement on Micromixer-micropumps Used in POC Device

No.	Microfluidic Unit	Disadvantages or Problems	Solutions	Potential Designs
1.	Micromixers	i. Active micromixers are not suitable for POC device ii. Lamination-based passive micromixers require long mixing channels to achieve complete mixing iii. 3D-structure passive micromixers and Obstacle-based 2D passive micromixers must utilize precision fabrication techniques and equipment	i. Passive micromixers are suitable for POC device ii. Shorter channel length is preferable iii. Avoid precision-based fabrication. iv. Integration of the curved-based and convergence-divergence based micromixer elements is needed to enhance micromixing based on Dean vortices and fluid collision	Two potential designs that are based on Dean vortices and fluid collision are; i. Micromixer with circular mixing channel ii. Tesla-type micromixer

Table 2.3: continued

2.	Micropumps	i. All active-driven full-size benchtop pumps are usually used ii. Most pumps are placed at the micromixer inlet (pre-micromixer placement) – This setting usually operates with a considerably higher working pressure, making the assembly prone to leakage iii. Multiple units of pumps are required to drive fluids into a multi-inlet micromixer	i. Small sized and portable passive-driven micropump is preferable ii. Micropump shall be placed at the micromixer outlet (post-micromixer placement) to avoid multiple pumps being used in a multi-inlet micromixer iii. Vacuum-like pumping method is preferable to avoid fluid leakage	Two potential designs that are passive, and suitable for post-micromixer placement are: i. Paper-based micropump ii. Vacuum-based micropump
3.	Integrated micromixer-micropump unit	i. Micropumps are usually characterized in a standalone operation only ii. Integrated micromixer-micropump unit for a successful liquid mixing has never been comprehensively studied	Selected passive micropump is characterized in an integration with the selected passive micromixer so that successful liquid mixing is achieved	Integrated unit of a passive micromixer and passive micropump

CHAPTER 3

METHODOLOGY

3.1 Chapter Overview

The methodology used for this study was segmented into sections based on the study objectives. The methodology is summarized in the form of research framework shown in Figure 3.1. To realize the first objective, the first section began by reviewing the previous literatures and outlining the shortcomings of the micromixers used in LOC systems, by which some potential micromixers that suitable for the application in a POC device were shortlisted. It was noted that micromixing technique based on Dean vortex and fluid collision are found suitable for fluid mixing in POC applications. Based on this criterion, the T-micromixer with circular mixing channel and Tesla micromixer, both of which utilize the mentioned micromixing techniques were investigated. The T-micromixer with circular mixing channel was selected and tested first for performance assessment as it featured simpler microchannel design as compared to the Tesla micromixer. However, due to the unfavourable mixing performance (MI < 100%) at $5 \leq Re \leq 40$, and the microchannel design was intricating to be improved further, the selection proceeded to the Tesla micromixer. The first objective was achieved as the Tesla micromixer was capable to completely mixed fluid (MI = 100%) at its tenth valve stage for Re = 40.

By referring to **Figure 3.1**, the potential micropumps were shortlisted after reviewing related literatures. The selected micropump to be utilized in the proposed POC unit must be able to sufficiently withdraw fluid from the Tesla micromixer, and this requirement was achievable by using the paper-based MAPC micropump and vacuum-based SAP micropump. The MAPC micropump was tested first for the flowrate assessment as it

featured simpler design as compared to the SAP micropump, and having a replaceable paper matrix. However, the flowrate adjustment and increment were strictly limited to platform angle and paper matrix size, restricting any possible design iterations. Thus, the SAP micropump was selected overcoming the aforementioned design limitations of the former. Inherently, the SAP micropump was flexible towards flowrate adjustment and increment that can be achieved through appropriate sizing of the pump chamber volume.

Following the first and second objectives, the appropriate size of the SAP micropump chamber volume was simulated through CFD prior to actual integration. By varying the operating gauge pressures, the optimum gauge pressure for a complete fluid mixing within the proposed integrated POC unit was determined. Next, the actual micropump was fabricated and physically attached to the Tesla micromixer for validation experiment and realization of the third objective.

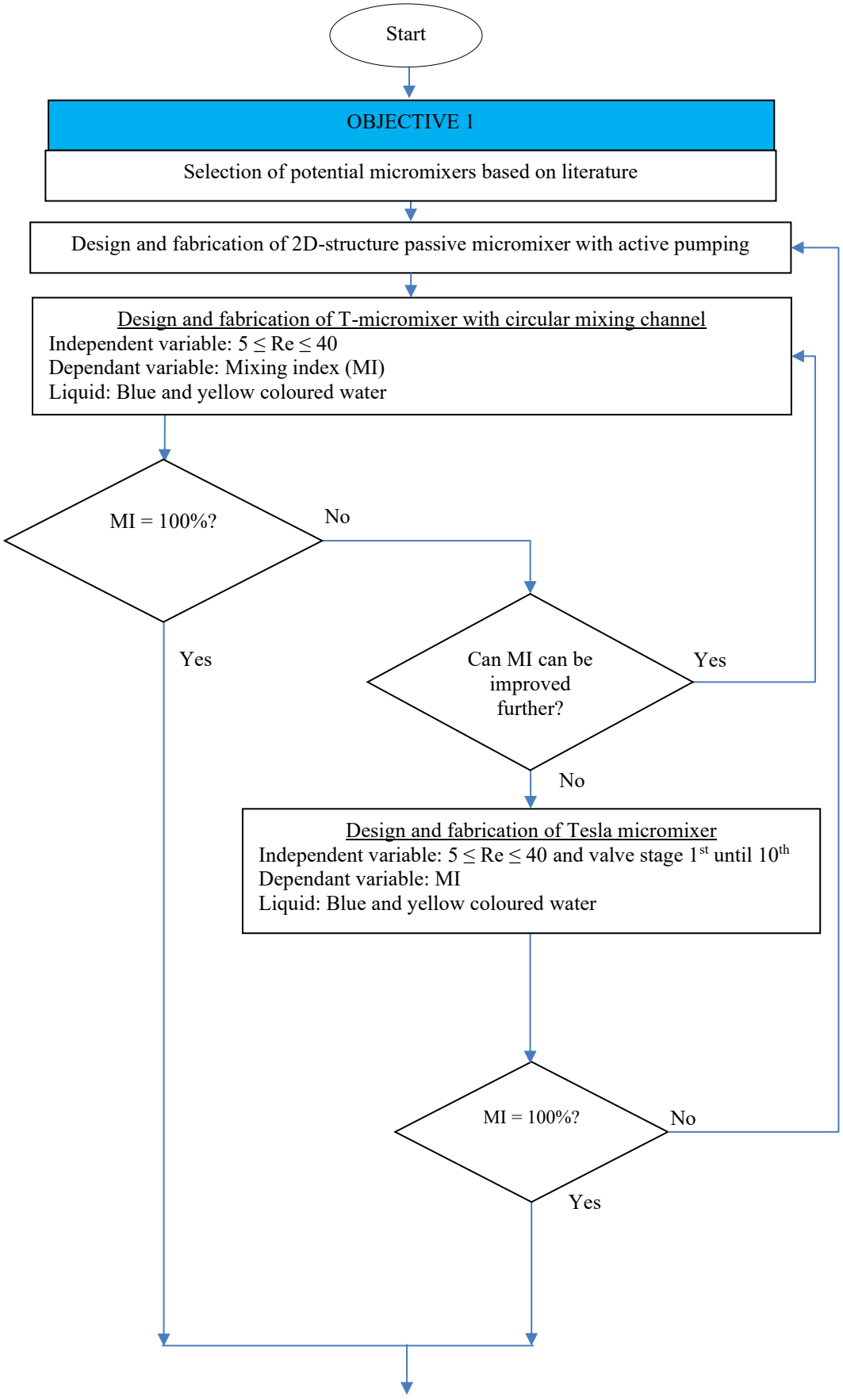
Start
OBJECTIVE 1
Selection of potential micromixers based on literature
Design and fabrication of 2D-structure passive micromixer with active pumping
Design and fabrication of T-micromixer with circular mixing channel
Independent variable: 5 ≤ Re ≤ 40
Dependant variable: Mixing index (MI)
Liquid: Blue and yellow coloured water
MI = 100%?
No
Yes
Can MI can be improved further?
Yes
No
Design and fabrication of Tesla micromixer
Independent variable: 5 ≤ Re ≤ 40 and valve stage 1st until 10th
Dependant variable: MI
Liquid: Blue and yellow coloured water
MI = 100%?
No
Yes

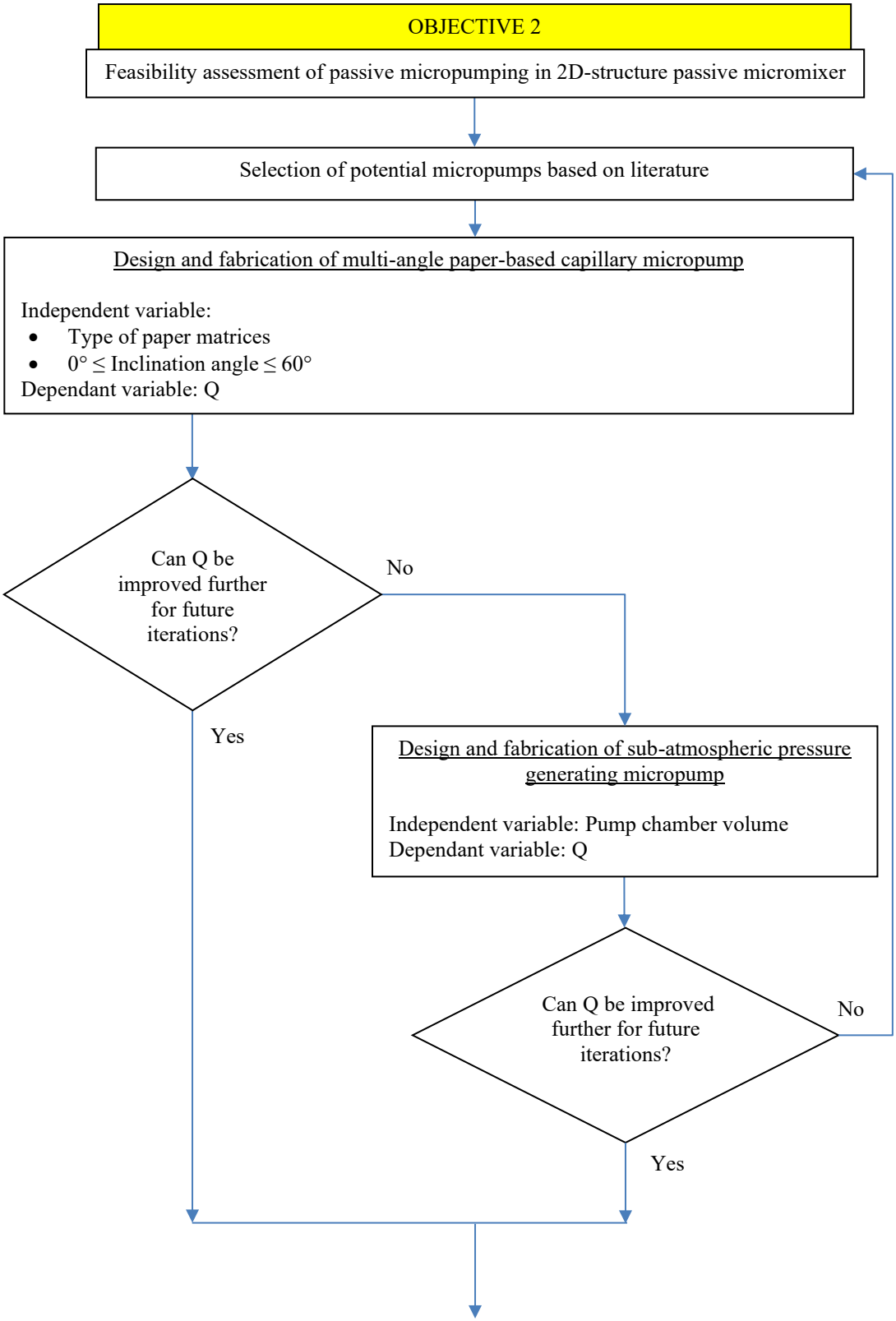
OBJECTIVE 2
Feasibility assessment of passive micropumping in 2D-structure passive micromixer
Selection of potential micropumps based on literature
Design and fabrication of multi-angle paper-based capillary micropump
Independent variable:
Type of paper matrices
0° ≤ Inclination angle ≤ 60°
Dependant variable: Q
Can Q be improved further for future iterations?
No
Yes
Design and fabrication of sub-atmospheric pressure generating micropump
Independent variable: Pump chamber volume
Dependant variable: Q
Can Q be improved further for future iterations?
No
Yes

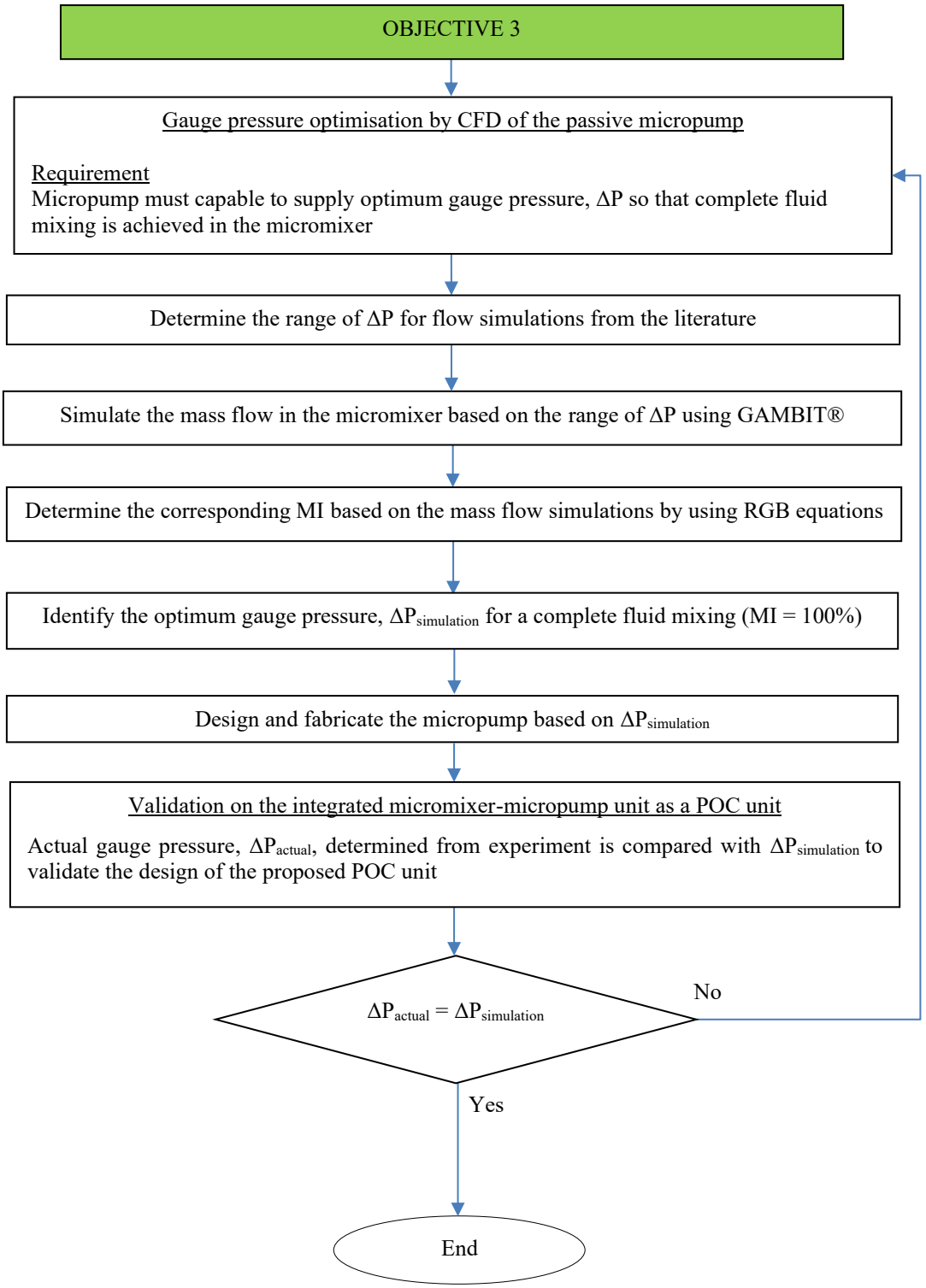

Figure 3.1: Research Framework

Table 3.1 shows the design of experiment that being conducted throughout the study. The first experiment was executed to observe the mixing performance (in terms of mixing index) of the T-micromixer with circular mixing channel based on the progressing Reynolds number from Re = 5, 10, 15 and 40. For the second experiment, mixing performance was measured at each valve stage in the Tesla micromixer for Re = 5, 10, 15 and 40. In the third experiment, flow rate performance was measured for each paper matrix in the MAPC micropump at different inclination angle, $\Theta = 0°$, 15°, 30°, 45° and 60°. Subsequently, in the fourth experiment, flow rate performance of the SAP micropump was measured based on the determined volumetric size of the chamber. Finally, the gauge pressure and mixing performance of the proposed POC device was tested to validate the CFD simulation.

Table 3.1: Design of Experiment

No.	Microfluidic Unit	Variables	
1.	T-micromixer with circular mixing channel	Independent	Re = 5, 10, 15, 20, and 40
		Dependent	Mixing index (%)
2.	Tesla micromixer	Independent	Valve stage = 1, 2, 3, 4, 5, 6, 7, 8, 9, and 10
			Re = 5, 10, 15, 20, and 40
		Dependent	Mixing index (%)
3.	MAPC micropump	Independent	i. Platform angle, $\Theta = 0°$, 15°, 30°, 45° and 60° ii. Paper matrix; a. Type-A (high-absorbing paper tissue) b. Type-B (SMITH filter 102) c. Type-C (office paper A4-70 g/m^2)
		Dependent	Flow rate (µL/s)
4.	SAP micropump	Independent	Volumetric size of micropump chamber (23 mL)
		Dependent	Flow rate (µL/s)
5.	Proposed POC unit	Independent	Volumetric size of SAP micropump chamber (23 mL)
		Dependent	Gauge pressure (kPa) and mixing index (%) in Tesla micromixer

3.2 Methodology to realize Objective 1

3.2.1 Design and Fabrication of T-micromixer with Circular Mixing Channel

T-micromixer with circular mixing channel was fabricated which is a modified version of a conventional T-micromixer, but with added circular mixing channel at the converging point of the inlets and outlet channels as illustrated in Figure 3.2. A maximized fluid collision can be generated due to the direct engagement of inlet flows as the placement of the inlet channels are in-line and opposite to each other. Subsequently, rotational fluid movement will be generated in the mixing channel, thus creating secondary flows such as the Dean vortices.

The T-micromixer with circular mixing channel was fabricated in-house from polymethyl methacrylate (PMMA) sheets with a thickness of 3 mm each. Each individual sheet was made up of two PMMA sheets of 65 mm in length, 40 mm in width and 3 mm thick. Three holes with a diameter of 6 mm were then etched out in the depth of 400 μm for direct attachment of inlets and outlet ports. A milled-through hole of 6.5 mm in diameter was also cut out from another PMMA sheet exactly at the intersection of two inlets and outlet channels before the insertion of the mixing channel. Both PMMA sheets were fixed together with a liquid organic compound of methyl ethyl ketone and leakage tests were done to ensure no fluid leak within the micromixer.

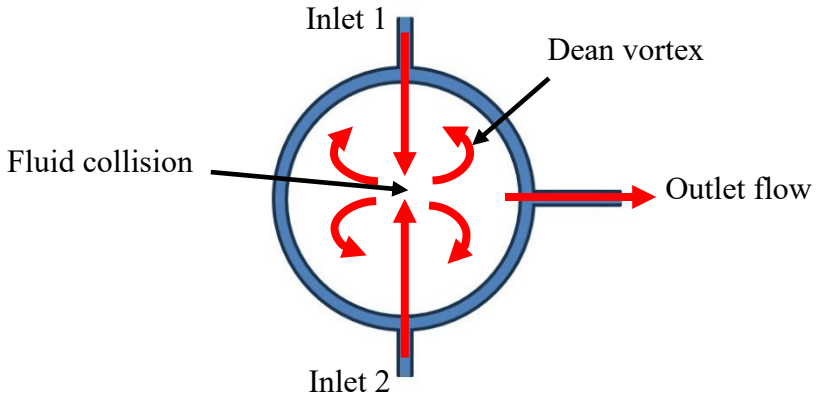

(a)

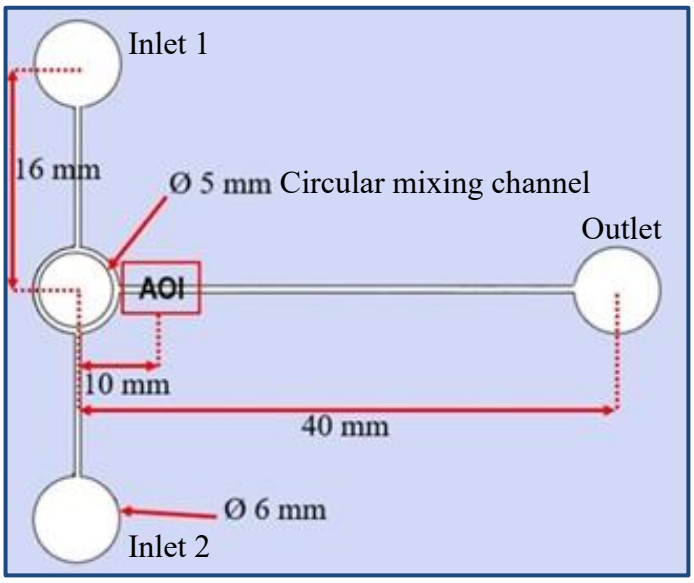

(b)

Figure 3.2: (a) Fluid Mixing Principle, and (b) Schematic Diagram of T-micromixer with Circular Mixing Channel

3.2.2 Design and Fabrication of Tesla Micromixer

Tesla micromixer utilizes the integration of the curved-based and convergence-divergence based micromixer elements to enhance micromixing based on Dean vortices and fluid collision (Figure 3.3a). The micromixer as shown in Figures 3.3b and 3.3c was made up of two PMMA sheets of 65 mm in length, 40 mm in width and 3 mm thick. The adopted Porwal et al. (2018) pattern of Tesla micromixer was constructed by micro-etching cut onto the main PMMA sheet using EASEL X-Carve micro-engraving machine with 100 µm

engrave bit to produce microchannels with a dimension of 400 µm width and 400 µm depth. Two inlets and one outlet port were then drill-out from the main PMMA sheet for insertion of tubing with a 3 mm internal diameter. The ports were attached using ultraviolet acrylic resin to prevent leakage before fixing the main to secondary PMMA sheets by using double-sided adhesive film with a thickness of 100 µm. A leak test was conducted 24 hours after the fabrication of the micromixer to confirm the reliability of all attachments.

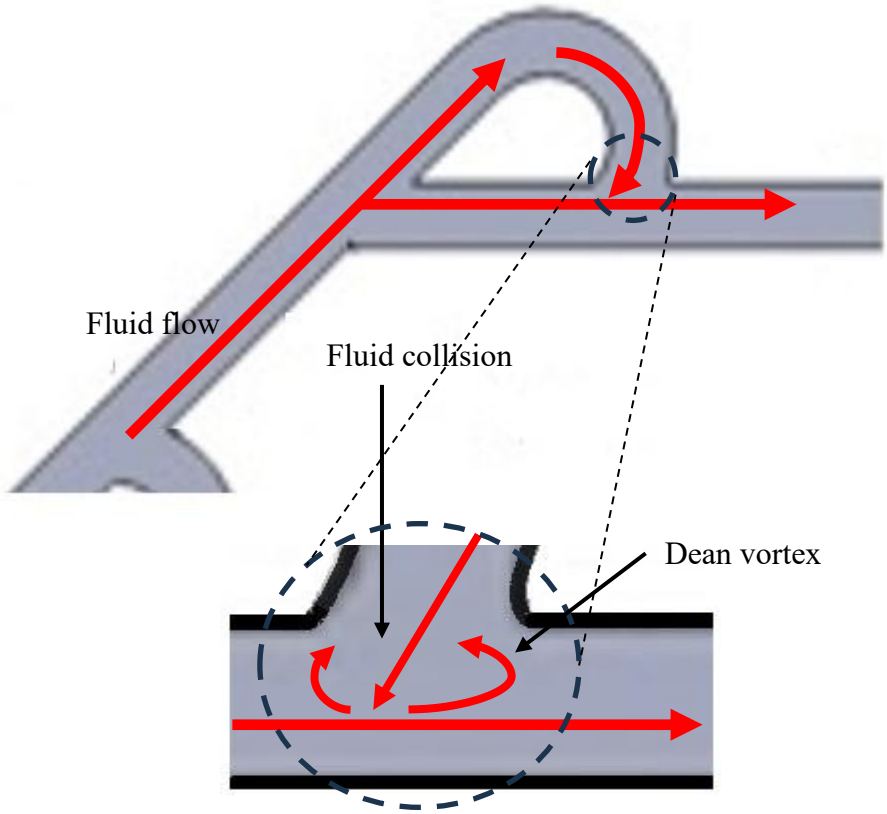

(a)

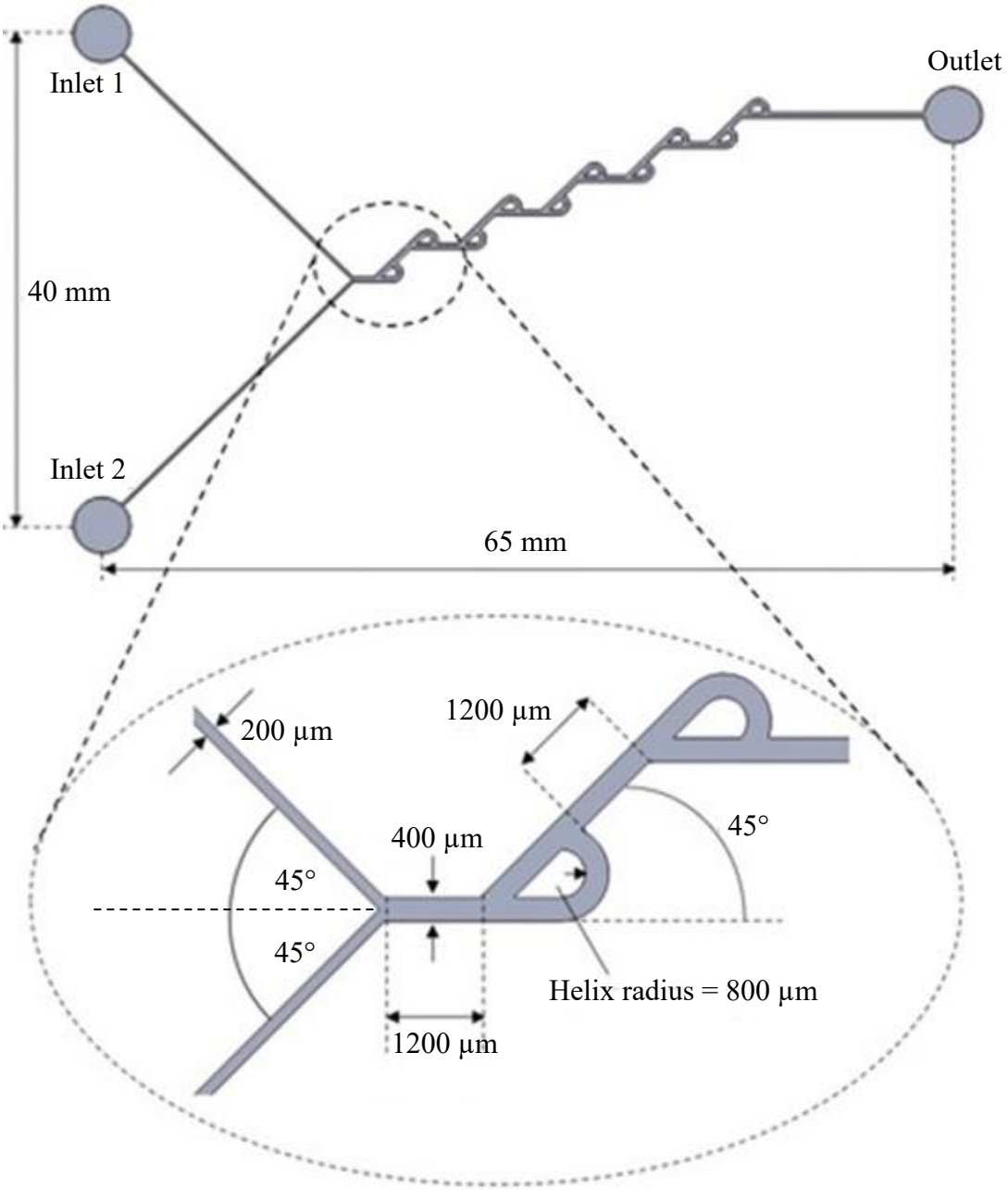
Inlet 1
Outlet
40 mm
Inlet 2
65 mm
200 µm
1200 µm
400 µm
45°
45°
45°
Helix radius = 800 µm
1200 µm

(b)

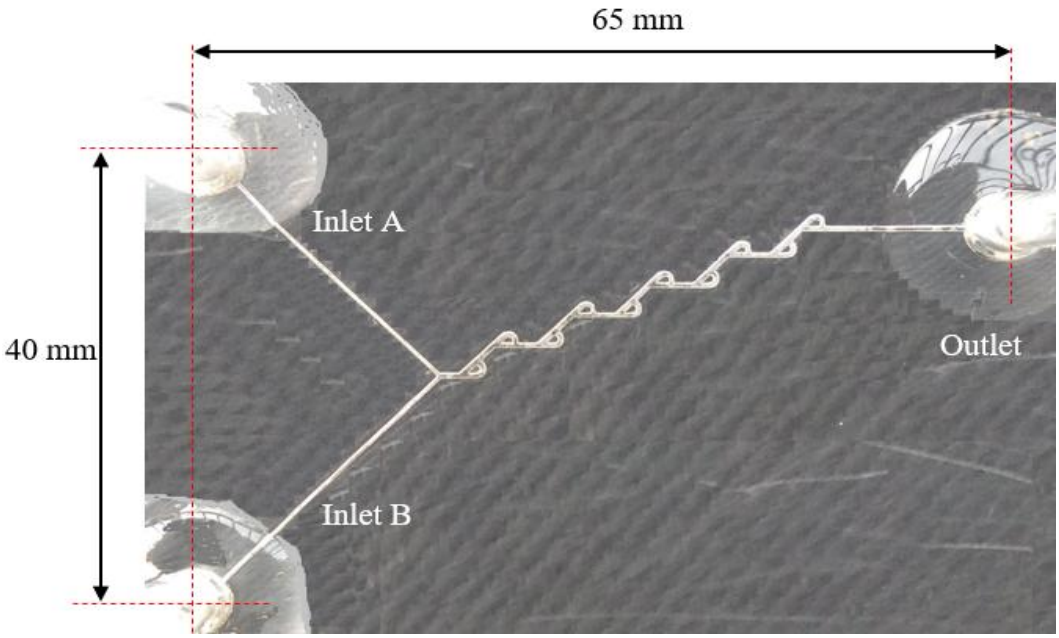

(c)

Figure 3.3: (a) Fluid Mixing Principle, (b) Schematic Diagram, and (c) Actual Fabricated Tesla micromixer

3.2.3 Experimental Setup on Mixing Performance of Proposed Micromixers

Experiments were conducted via a set of apparatus as shown in Figure 3.4. The blue solution was prepared by mixing food-grade dye (FD&C Blue 1) with water with a ratio of 1:60. A similar step was used to prepare yellow solution but with FD&C Yellow 6 dye. The density (997 kg/m^3) and viscosity (0.00089 kg/ms) of the coloured solutions were assumed to be similar to water owing to low dye concentrations.

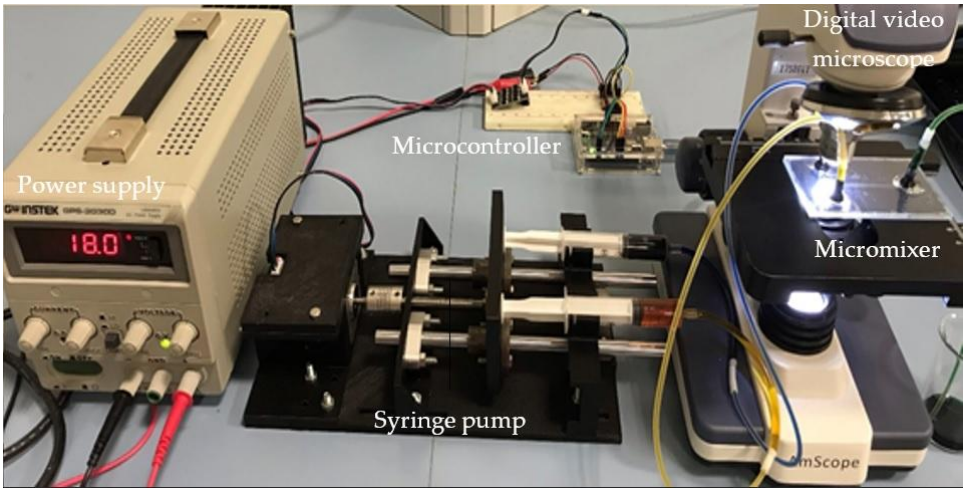

(a)

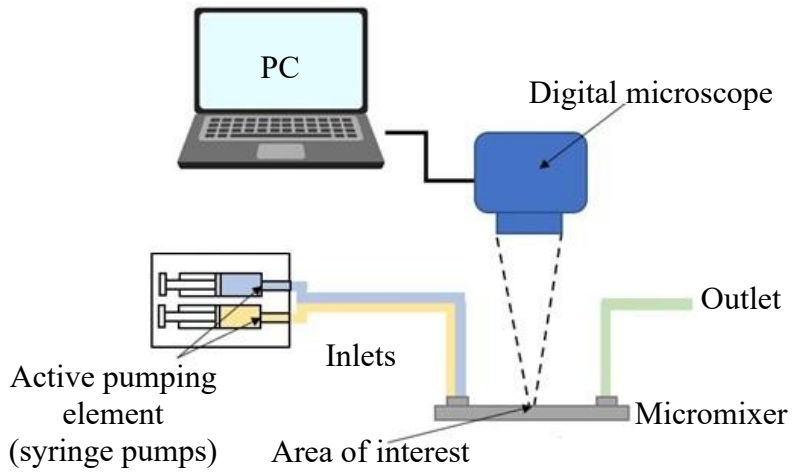

(b)

Figure 3.4: (a) Experimental Apparatus and Setup, and (b) Schematic Diagram of Micromixing Experiment

An active benchtop syringe pumps were used to drive the blue and yellow solutions into the Tesla micromixer using a two-phase stepper motor controlled by an Arduino Uno microcontroller. Volumetric tolerance of a single MEDIC ALCHEMY® 10 ml hypodermic syringe is ± 4%. The rotational resolution was increased from 200 to 3,200 steps per rotation by using an A4988 smoother driver to further refine the steps in the stepper motor so that stuttering and vibration were reduced. A digital video microscope (AmScope MD500) with 4× magnification (resolution of 368 × 368 pixels) was used to capture the images at the assigned area of interrogation (AOI), with all microscope settings and ambient light was kept constant throughout the experiments. Mixing index measurement was carried out in MATLAB® software by analysing the cropped images of the AOI, and by using the related equations as discussed in Section 3.2.4. The same experiment was done in 30 repetitions to capture mixing images at each valve stage of the micromixer. Mixing performance was calculated based on the red-green-blue (RGB) colour model method.

Nguyen et al. (2019) found that $Re \leq 5$ is believed to be unsuitable for fluid mixing while $Re \geq 100$ is uncommon in any passive micromixers due to the limited capability of micropumps for providing such high Re (Cai et al., 2017; Hossain & Kim, 2014; The et al., 2014; Viktorov et al., 2016). Therefore, to make the experiment reliable, the Re range of $5 \leq Re \leq 40$ was taken for the entire tests. The variables related to the study on micromixers are tabulated as in

Table **3.2**.

Table 3.2: Independent and Dependant Variables of Experiment on Micromixers

No.	Micromixer	Variables	
1.	T-micromixer with circular mixing channel	Independent	Re = 5, 10, 15, 20, and 40
		Dependent	Mixing index (%)
2.	Tesla micromixer	Independent	Valve stage = 1, 2, 3, 4, 5, 6, 7, 8, 9, and 10
			Re = 5, 10, 15, 20, and 40
		Dependent	Mixing index (%)

3.2.4 Mixing Index Calculation

Mixing performance was calculated based on the red-green-blue (RGB) colour model method (Mahmud & Tamrin, 2020). The equations of the said RGB method are given in equations 3.1, 3.2 and 3.3.

$$N_{mixed} = n\left(\left\{r_{g,min} \le R \le r_{g,max} \cap\ g_{g,min} \le G \le g_{g,max} \cap\ b_{g,min} \le B \le b_{g,max}\right\}\right) \quad \text{Equation 3.1}$$

$$N_{not\text{-}mixed} = n\left(\left\{r_{b,min} \le R \le r_{b,max} \cap\ g_{b,min} \le G \le g_{b,max} \cap\ b_{b,min} \le B \le b_{b,max}\right\}\right) + n\left(\left\{r_{y,min} \le R \le r_{y,max} \cap\ g_{y,min} \le G \le g_{y,max} \cap\ b_{y,min} \le B \le b_{y,max}\right\}\right) \quad \text{Equation 3.2}$$

$$\text{Mixing index, MI (\%)} = \frac{N_{mixed}}{N_{mixed} + N_{not-mixed}} \quad \text{Equation 3.3}$$

where N_{mixed} and $N_{not\text{-}mixed}$ are the numbers of mixed and unmixed pixels, respectively. n is the number of pixels that satisfy the RGB conditions. Red, green, and blue values derived

from images are represented as r, g, and b, and the Boolean operator ∩ refers to AND. Subscripts b, y, and g represent the minimum or maximum RGB values of blue, yellow, and green (mixed) pixels, respectively. N_{mixed} is for green pixels, while $N_{not\ mixed}$ comprises both blue and yellow pixels. The illustration on the calculation of mixing performance is shown in Figure 3.5.

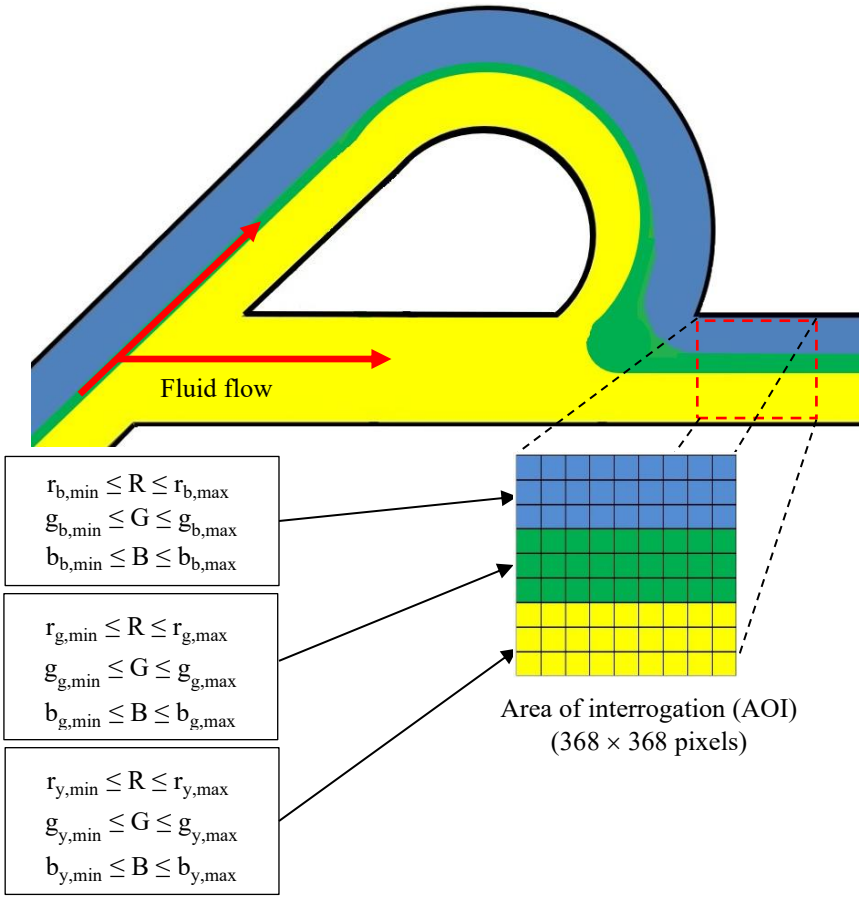

Figure 3.5: Illustration on the Calculation of Mixing Performance

3.3 Methodology to realize Objective 2

3.3.1 Design and Fabrication of Multi Angle Paper-based Capillary Micropump

The proposed paper-based capillary micropump comes with the capability of platform tilting to varying angles, θ so that the effect of gravity is integrated along into the

micropump flow rate. With this capability, this micropump can be designated as the multi angle paper-based capillary (MAPC) micropump. The MAPC micropump was developed by utilizing both hydrostatic (Section A) and capillary (Section B) effects, as shown in Figure 3.6. In Section A, the fluid flow within the fabricated microchannel is governed by Bernoulli's equation, and is used for determining the velocity at point, h_B. The same principle has been applied in micropump designs developed by Wang et al. (2018) and Kai et al. (2012). The generalized expression of Bernoulli's equation is;

$$\frac{v^2}{2} + \frac{P}{\rho} + \vec{g}h = \text{constant} \qquad \text{Equation 3.4}$$

where v is the velocity at the chosen point along the streamline, $\vec{g}$ is the gravitational acceleration, h is the elevation of the point above a reference plane, P is the pressure at the chosen point, and ρ is the density of the fluid used. By referring to Figure 3.6, V_T and V_B can be assumed as the velocities at points, h_T and h_B, respectively. Accordingly, the flow rate at point h_B can be written as

$$Q_H = A_{CS}\sqrt{2g(h_T - h_B)} \qquad \text{Equation 3.5}$$

where A_{CS} is the cross-sectional area of the microchannel. It is noted that Q_B is directly proportional to the manipulated inclination angles, θ = 15°, 30°, 45°, and 60°. Meanwhile, in Section B, the paper-capillary flow rate, Q_{PC} is governed by the porosity of the paper matrix, and can be calculated according to Washburn's equation (Soum et al., 2019; Washburn, 1921) at the expense of negligible gravitational force (Xu et al., 2020).

$$Q_{PC} = \text{Porosity}\left(\frac{A_{flow}}{4}\sqrt{\frac{D_{cap}\cdot\gamma\cos\beta}{\mu t}}\right) \qquad \text{Equation 3.6}$$

The porosity is defined as the percentage of gaps that can be filled with liquid to the total volume of the porous material. Parameters A_{flow}, D_{cap}, γ, β and μ are the cross-sectional area of the flow path, the effective capillary diameter, the interfacial tension, the angle of contact between the porous material surface and liquid, and the dynamic viscosity of the liquid, respectively. By incorporating both the hydrostatic effect in Section A, and the paper capillary effect in Section B, the total flow rate generated by the MAPC micropump is;

$$Q_{MAPC} = Q_H + Q_C \qquad \text{Equation 3.7}$$

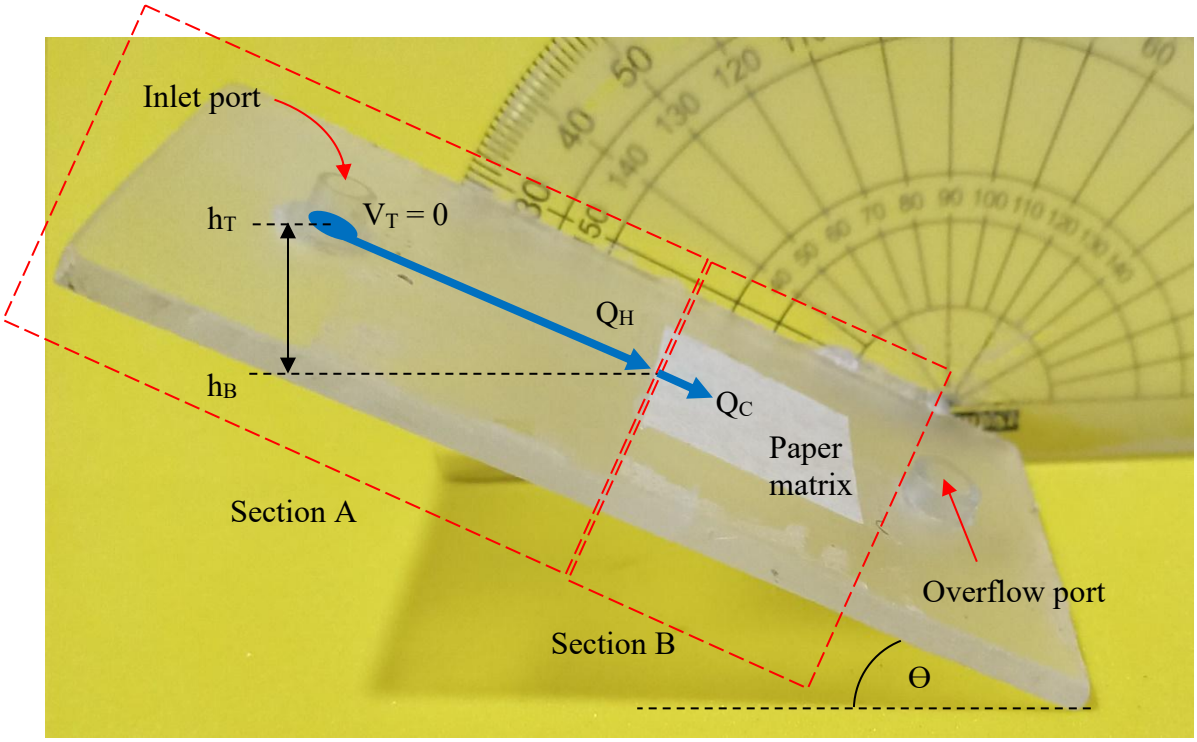

Figure 3.6: MAPC Micropump

MAPC micropump platform was made from two layers of PMMA sheets, constructed by using the same micro-etching procedure. A compartment with dimensions of 40 mm × 40 mm × 0.5 mm was etched out of the PMMA sheet for placing the paper matrix unit. Inlet and overflow ports with 3.5 mm diameter were cut through and linked to the square

compartment via a straight-line square-duct microchannel of 400 μm × 400 μm. The engraved sheet was then fixed to another PMMA sheet of the same size by using double-sided adhesive film. MAPC micropump operates by utilizing the combined effects of paper-based capillary and gravity. Tests were done by observing the flow rates generated during the inclination of micropump platform to the angles of θ = 15°, 30°, 45°, and 60°, with the attachment of paper matrices; a) Type-A (high-absorbing paper tissue), b) Type-B (SMITH filter 102), and c) Type-C (office paper A4-70 g/m^2).

3.3.2 Design and Fabrication of Sub-Atmospheric Pressure Micropump

Vacuum-based micropumps are capable to generate sub-atmospheric or negative pressure for fluid micropumping. Here, a new design of micropump that utilizes vacuum that being generated in its pneumatic chamber is proposed. Fluid is driven into the micropump as the sub-atmospheric pressure is generated inside the chamber which is lower than ambient. As the proposed micropump was designed in accordance to the concept of vacuum generating, hence it is designated as sub-atmospheric pressure (SAP) generating micropump. SAP micropumps operates by using the initiated vacuum in the micropump chamber. As shown in Figure 3.7, it is initiated by depressing the chamber to release air. At this stage, fluid flow from the inlet is blocked by the inlet check-valve. Next, as the micropump chamber is being undepressed, it reverts to its original shape hence creating vacuum internally. Here, the outlet check-valve is closed while the inlet is open, making the working fluid flows into the chamber.

Two sets of moulds of the SAP micropump chamber in a half-sliced cylindrical shape were designed and printed using Ender 3D-printer. The uncompressed chamber volume was measured with a total volume of 23 mL. Subsequently, the EcoflexTM 00-30 PDMS was premixed, poured into each printed mould, and left for about two hours. The partially-cured,

half-sliced chambers were extracted from the mould and attached. Meanwhile, the input and output check valves were simultaneously 3D printed, and attached to both inlet and outlet of the partially-cured micropump chamber. They were left for complete curing for another 22 hours. These check valves function as flow diodes by allowing a uni-directional fluid flow (Li et al., 2012a) through the inlet and outlet of the pump chamber. Next, the chamber and check valves were then fixed into another mould with a cuboidal shape, poured with a premixed PDMS, and set to cure for another 24 hours. This process is aimed for embedding the chamber and check valves as a single SAP micropump assembly unit (Figure 3.8). After the curing process, the tubing was attached to the inlet and outlet of the SAP micropump assembly.

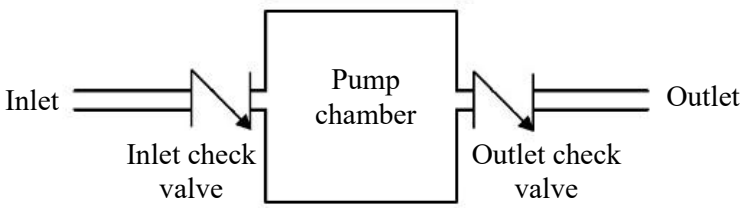

(a)

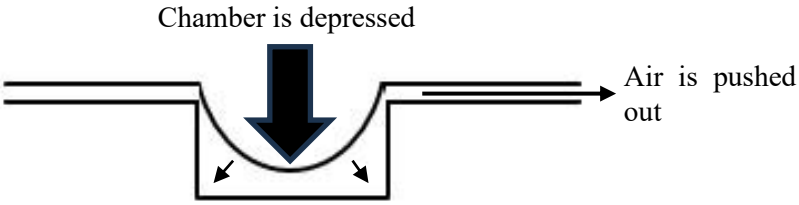

(b)

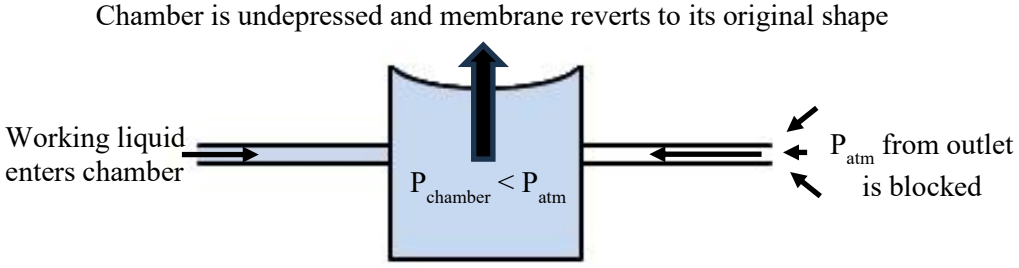

(c)

Figure 3.7: Sequence of Operating Event of SAP Micropump;(a) Initial Condition, (b) Pump Chamber is Depressed, and (c) Pump Chamber is Undepressed

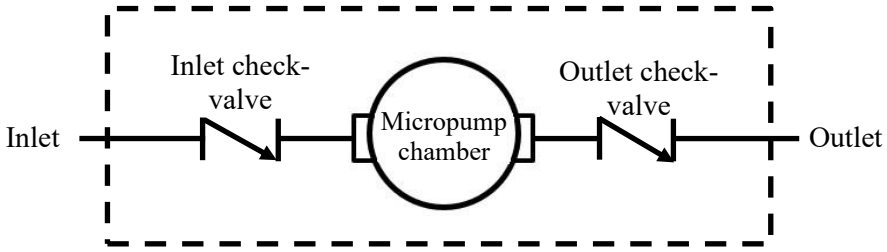

Figure 3.8: Schematic Diagram of SAP Micropump Assembly

3.3.3 Experiments Setup on Flow Rate Performance of Proposed Micropumps

Experiments on standalone MAPC and SAP micropumps operations were conducted by attaching the micropump to a reservoir of blue coloured distilled water for investigating the flow rates generated. Time was taken as soon as the working liquid started to cross the start line and recorded simultaneously as the stop line was reached (Figure 3.9). All recorded time were used to calculate fluid velocities and flow rates. Related variables to the standalone micropump operation are listed in Table 3.3.(c)

A set of 30 tests was repeated for the MAPC and SAP micropumps for statistical validity. As according to the central limit theorem, 30 unit of sample is sufficiently large for the data distribution to be a bell-shaped/normal distribution regardless of the population size, which subsequently allows the use of normal distribution techniques in confidence interval estimation (Ahsanullah et al., 2014; Cohen, 2013; Field, 2024).

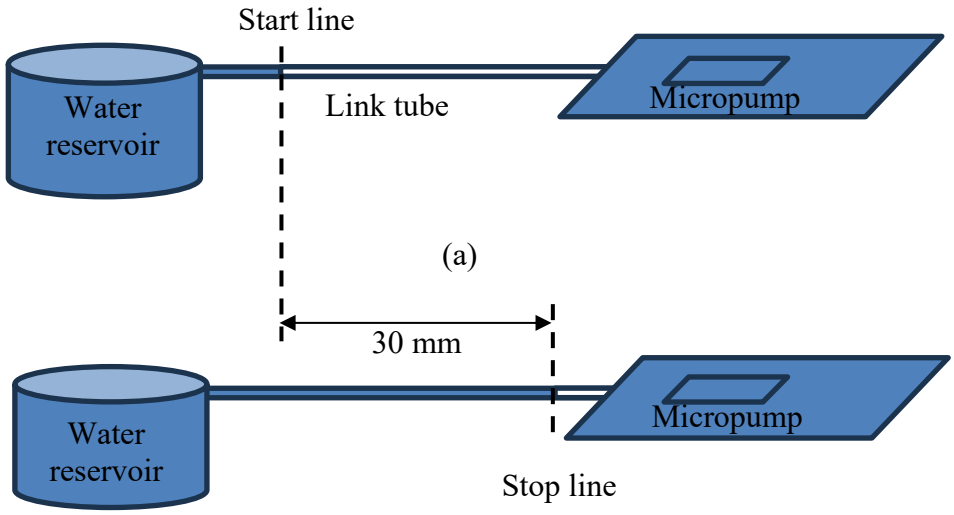

Figure 3.9: Schematic Diagram for Assessing the Flow Rates of MAPC and SAP Micropumps; (a) Initial Condition, and (b) Final Condition

Table 3.3: Independent and Dependant Variables of Experiment on Micropump

No.	Micropump	Variables	
1.	MAPC	Independent	i. Platform angles of 0°, 15°, 30°, 45°, and 60° ii. Paper matrix type; a. Type-A (high-absorbing paper tissue) b. Type-B (SMITH filter 102) c. Type-C (office paper A4-70 g/m^2)
		Dependent	Flow rate, Q (µL/s)
2.	SAP	Independent	Size of micropump chamber
		Dependent	Flow rate, Q (µL/s)

3.4 Methodology to realize Objective 3

3.4.1 CFD Simulations

Design optimization via experiments is known to be laboriously time consuming and non-economical due to the fact that for each iteration of gauge pressure, an individually fabricated micropump is required. This fabrication cycles continues until the desirable gauge pressure is achieved. This design and fabrication intricacies however, can be overcome by CFD simulations to determine the range of suitable gauge pressure. As an addition, CFD simulations also crucial for a comprehensive understanding of the mass flow and mixing in the proposed POC unit.

Boundary Conditions

Boundary conditions must be carefully defined to minimize errors at the interfaces between the fluid domain and its surroundings. The flow through the Tesla micromixer was assumed to be;

i. Steady state
ii. Laminar and incompressible
iii. Constant fluid properties
iv. Negligible viscosity dissipation
v. Single phase flow
vi. Negligible gravity effects as flows perpendicular to gravity
vii. No-slip condition at the boundary
viii. Inlet pressure: Standard atmospheric pressure (P_{atm})

ix. Outlet pressure: For varying conditionings, the negative gauge pressure indicates the pressure is less than P_{atm} given in the range of $-10 \leq \Delta P \leq -100$ kPa for different scenarios

Governing Equations

Standard mass continuity and momentum balance for Newtonian fluid was used for the CFD simulations. The governing equations for fluid continuity and momentum are stated in Equations 3.4 and 3.5, respectively. These equations were numerically solved by employing a pressure based finite volume solver via GAMBIT®.

$$\frac{\partial \vec{\mathbf{u}}_j}{\partial x_j} = 0 \qquad \text{Equation 3.8}$$

$$\rho \vec{\mathbf{u}}_j \frac{\partial \vec{\mathbf{u}}_l}{\partial x_j} - \mu \frac{\partial^2 \vec{\mathbf{u}}_l}{\partial x_j \, \partial x_j} + \frac{\partial P}{\partial x_l} = 0 \qquad \text{Equation 3.9}$$

where $\vec{\mathbf{u}}$ is the fluid steady-state velocity field. Velocity at the inlet was set based on the Re equation (Equation 3.6), and the volumetric flowrate, Q was calculated by using equation 3.7;

$$Re = \frac{\rho v D_H}{\mu} \qquad \text{Equation 3.10}$$

$$Q = \frac{\pi Re D_H \mu}{4} \qquad \text{Equation 3.11}$$

where ρ is water density, v is the velocity at the inlet, D_H is the hydraulic diameter, and μ is the dynamic viscosity of water.

Mesh Independency

Mesh independence study is used to verify that the number of grids used in the calculation is not affecting the simulation results performed in a steady-state conditions. Although denser grid points will give more accurate result, an overly dense grids requires longer computation period (Kelley et al., 2020). In addition, the simulation results must not change significantly with further mesh refinement to comply with independency. Simulations are done with progressively finer mesh, and the results are then plotted against the mesh size to observe the convergence (dos Santos et al., 2019). Mesh independency of the Tesla micromixer was based on the element size which is directly linked to the statistics of elements and nodes. The statistic of the mesh varies accordingly as the size of the mesh changes. The mesh was controlled by using the mesh control settings tuned finely by applying the curvature-based function, refinement function, separate face meshing and defeaturing size. In addition, mesh inflation was also tuned. Table 3.4 shows the overall mesh statistics of the Tesla micromixer. Details of the mesh at the second valve and the outlet of Tesla Micromixer is shown in Figure 3.10.

Table 3.4: Mesh Statistics

No.	Description	Value
1.	Minimum element size	0.02 mm
2.	Maximum face size	3.14 mm
3.	Growth rate	1.20 (120%)
4.	Minimum edge length	0.0304 mm
5.	Number of nodes	363,208 nodes
6.	Number of elements	352,311 elements

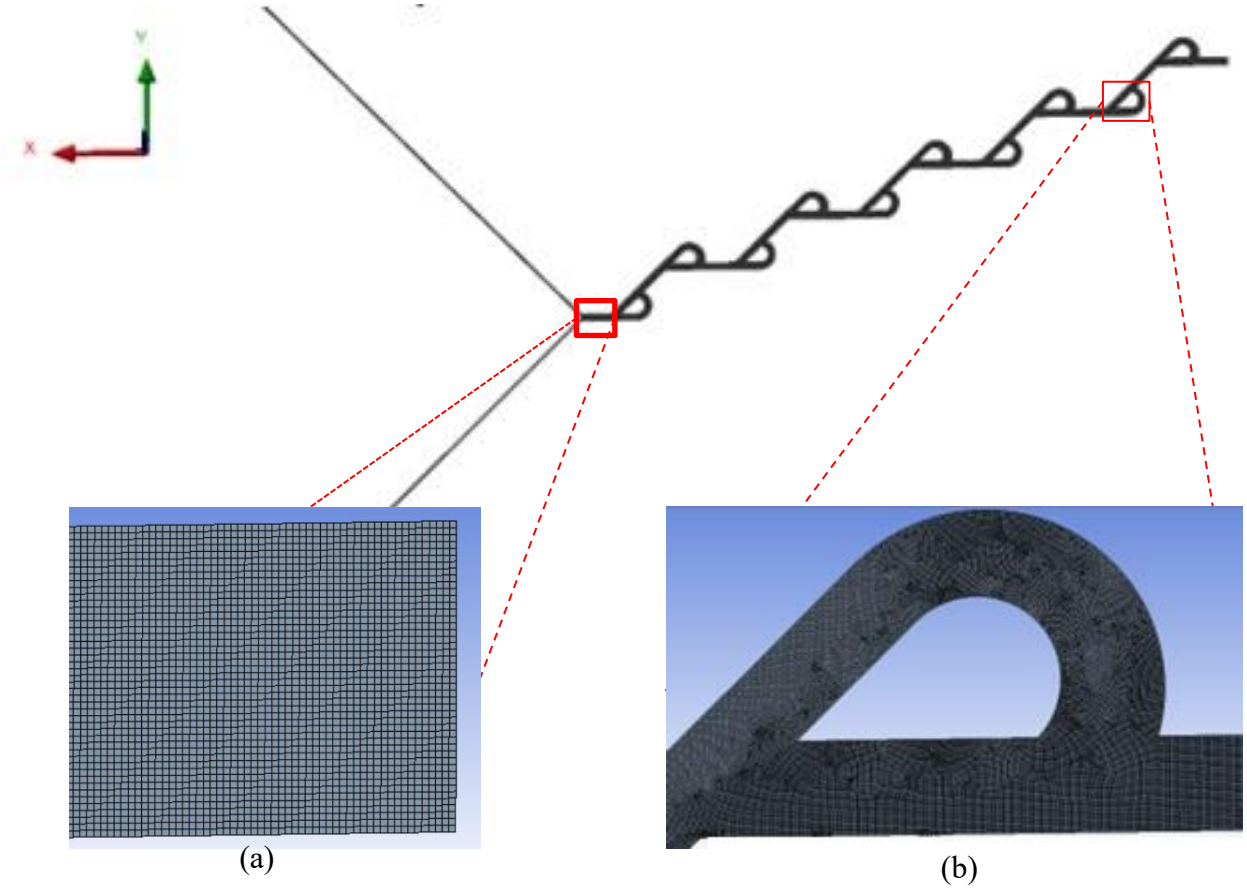

Figure 3.10: Mesh Details of the (a) Second Valve, and (b) Outlet of the Tesla Micromixer

The convergence and the trend of residuals (continuity, x-velocity, and y-velocity) with each iteration at varying valve number of the Tesla micromixer, as they approach the best possible results were studied. Figure 3.11 shows the convergence and residuals trends with respect to the first valve. The residuals decrease as the iterations increases, suggesting that the numerical inaccuracy is reducing with each iteration. Convergence occurs when residuals fall below the threshold of 10^{-3}. This indicates that the solution has achieved a stable condition in which more iterations would have little effect on the accuracy of the results and demonstrates the solution's precision and reliability for the given boundary conditions. Overall, the errors in the CFD were controlled by defining the convergence criteria in the calculations, mesh quality checks, and the setting of different parameters such

as skewness and smoothing. The refinement in the mesh and proper growth rate minimizes the numerical errors.

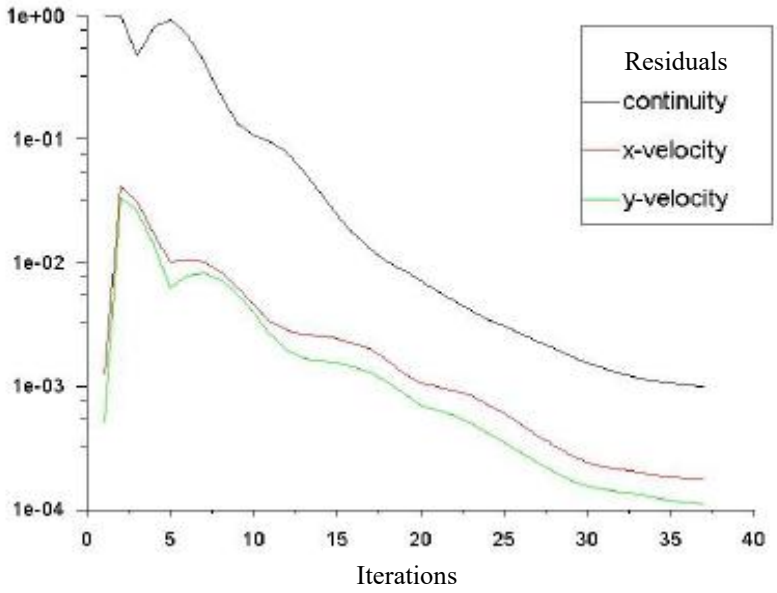

Figure 3.11: Numerical Accuracy (In Terms of Convergence) of the First Valve of Tesla Micromixer

Uniformity Index

Uniformity index is used to evaluate the consistency of mesh size in CFD. A more uniform mesh often leads to more accurate results as it reduces numerical errors associated with element distortion and size variations. The uniformity index is defined as the ratio of the average mesh size to the maximum mesh size. A value close to 1 indicates a more uniform mesh. Table 3.5 shows the uniformity index across different patches of the micromixers after each tesla valve with varying the mesh size. It can be observed that the percentage variation between mesh size of 0.04 and 0.03 mm were acceptable, therefore 0.04 mm mesh size was used to ensure mesh independence.

Table 3.5: Evaluation of Uniformity Index for Mesh Consistency

No.	Mesh Size (mm)	Uniformity Index									
		Patch 1	Patch 2	Patch 3	Patch 4	Patch 5	Patch 6	Patch 7	Patch 8	Patch 9	Patch 10
1.	0.02	0.97007759	0.9762688	0.98061577	0.98446242	0.98726415	0.98982234	0.991795	0.993411	0.99466	0.995722
2.	0.03	0.96749807	0.97252438	0.97619674	0.97948564	0.98210635	0.98458341	0.98667	0.988502	0.990003	0.991408
3.	0.04	0.96713713	0.97166092	0.97502362	0.9780572	0.98054554	0.98294820	0.984931	0.986789	0.988262	0.989745
4.	0.05	0.96662762	0.97107553	0.9741905	0.97717897	0.97946124	0.98169934	0.983516	0.985389	0.98676	0.988327
5.	0.06	0.96677691	0.97140822	0.97464264	0.97776606	0.98017697	0.98258711	0.984374	0.986153	0.987491	0.988864

3.4.2 Experimental Validation of CFD Simulations

For validation, the selected passive micromixer and micropump were linked to each other based on the schematic diagram as shown in Figure 3.12, for comparing ΔP_{actual} to $\Delta P_{simulation}$.

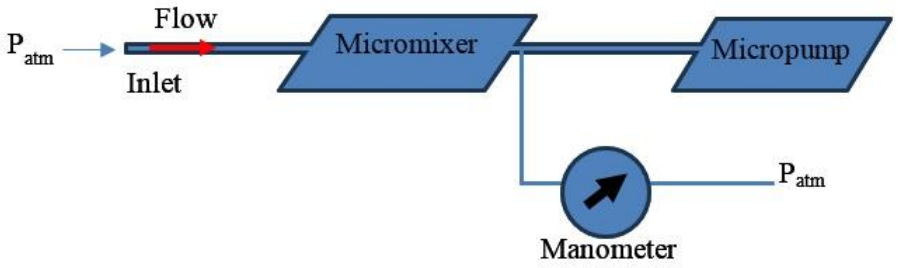

Figure 3.12: Schematic Diagram for Assessing the ΔP_{actual}

3.5 Measurement Uncertainties

This study was characterized based on variables such as pressure, P, time, t, mixing index, MI, and Re. Corresponding measurement uncertainties of the respective variables and their sources are presented in Table 3.6 and according to the Joint Committee for Guides in Metrology (JCGM) 2008 (BIPM et al., 2008). Measurement uncertainty, U_M is expressed in terms of bias limit, L_b and precision limit, L_p.

$$U_m = \sqrt{{L_b}^2 + {L_p}^2} \qquad \text{Equation 3.12}$$

Table 3.6: Measurement Uncertainties

No.	Parameter (unit)	L_b		L_p		U_M
		Source	Value	Source	Value	
1.	Pressure (kPa)	Digital manometer	± 0.01	30 repetitions	X_P ± 0.053	± 0.063
2.	Time (s)	Stopwatch	± 0.018		X_t ± 0.2	± 0.218
3	Mixing Index (%)	368 × 368 pixels	± 0.0007 %		X_{MI} ± 2%	± 2 %
4.	Reynolds number (Re)	Hypodermic syringe	± 0.04		X_{Re} ± 0.2	± 0.204

where X_P, X_t, X_{MI} and X_{Re} are mean values for fluid pressure, stopwatch time, mixing index and Re, respectively.

3.6 Chapter Summary

This chapter presented the methodology used to achieve each research objectives in the entire study, and can be summarized as in Table 3.7.

Table 3.7: Summary of Chapter 3

No.	Objective	Microfluidic Unit	Task or Method
1.	First	i. T-micromixer with circular mixing channel ii. Tesla micromixer	i. Design and fabrication ii. Experiments for characterization of MI iii. Selection of the suitable micromixer for the proposed POC unit
2.	Second	i. MAPC micropump ii. SAP micropump	i. Design and fabrication ii. Experiments for characterization of Q iii. Selection of the suitable micropump for the proposed POC unit
3.	Third	Integration of the selected micromixer and micropump	i. Optimization using CFD simulation ii. Validation via experiment

CHAPTER 4

RESULTS AND DISCUSSION

4.1 Chapter Overview

Chapter 4 presents the results and discussion chronologically, and presented into sections based on the study objectives. In Section 4.2, the mixing performances of the T-micromixer with circular mixing channel and Tesla micromixer were compared to get the most suitable passive micromixer to be adapted into the proposed POC unit. In Section 4.3, the comparison of flow rate performances of the paper-based MAPC micropump and vacuum-based SAP micropump were made to determine the appropriate passive micropump for the integration with the selected micromixer mentioned in the previous section. In the final section, numerical study via CFD simulation was executed to optimize the operating gauge pressure in the proposed POC unit. Then, the actual experiment of the fabricated POC unit was executed to validate the CFD simulation.

4.2 Results and Discussion for Objective 1

4.2.1 Mixing Performance of T-micromixer with Circular Mixing Channel

Qualitative images presented in Table 4.1 were taken during the experiments to observe the effect of increasing Re to fluid mixing performance. Images taken during observations in the AOI show a distinguishable green fluid stream as the mixing product of the blue- and yellow-coloured liquids. Mixing performance, MI of the T-micromixer with circular mixing channel is seemingly intensified as the Re increased progressively from 5 to 40. Figure 4.1 shows the mixing performance of conventional T- and Y-micromixers that having a straight mixing channel and the proposed T-micromixer with circular mixing

channel. Result shows that the T-micromixer with circular mixing channel gave relatively higher mixing performance as compared to conventional T- and Y-micromixers. In a straight mixing channel such found in conventional T- and Y-micromixers, an increased in Re causes a lower mixing index and vice versa due to the reduction in residence time of liquid in the microchannel (Mahmud & Tamrin, 2020; Matsunaga et al., 2013). Liquid mixing in a straight mixing channel generally caused by molecular diffusion, and it is becoming more dominant when Re is progressively reduced (Babaie et al., 2022). However, this is different in the case of T-micromixer with circular mixing channel. Higher Re amplified the effect of fluid collision and Dean vortices that subsequently increased advection intensively. This indicates that liquid mixing was greatly influenced by the geometry of the added circular mixing channel in T-micromixer.

Table 4.1: Mixing Images of T-micromixer with Circular Mixing Channel at $5 \leq Re \leq 40$

No.	**Re ± 0.3**	**MI (± 1%)**	**Colour Reference**
1.	5	 MI = 44.31%	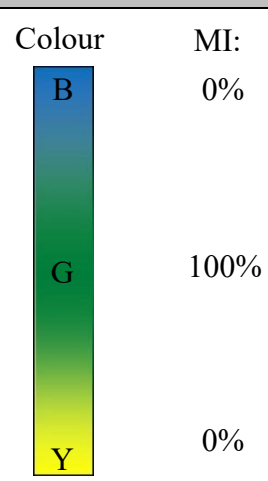
2.	10	 MI = 52.70%	
3.	20	 MI = 54.58%	
5.	40	 MI = 57.33%	

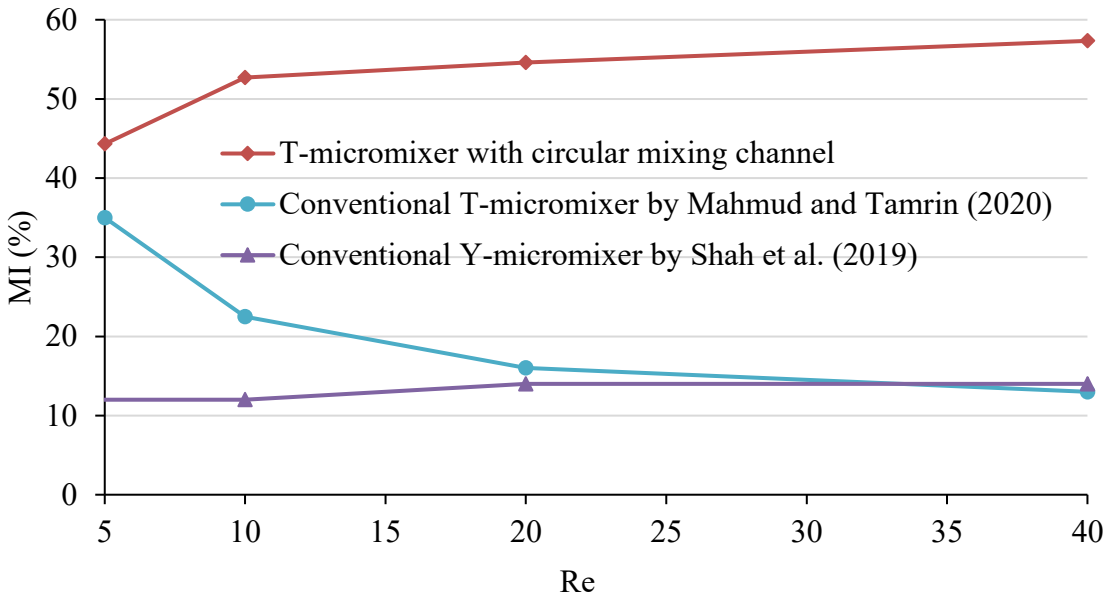

Figure 4.1: Mixing Performance of Conventional T-and Y-micromixers, and T-micromixer with Circular Mixing Channel at $5 \leq Re \leq 40$

4.2.2 Mixing Performance of Tesla Micromixer

Experiments on Tesla micromixer was done by observing liquid mixing performance based on; a) the effect of increasing valve stage (from first to tenth) at fixed Re (Figure 4.2) and, b) the effect of increasing Re ($5 \leq Re \leq 40$) at fixed valve stage (Figure 4.3). Though all 10 valve stages were analysed, only the first, fifth, and tenth valves are presented here for ease of discussion (Table 4.2). A gradual increment of the mixing index was identified at all valve stages for Re = 5, 10, 15, and 20.

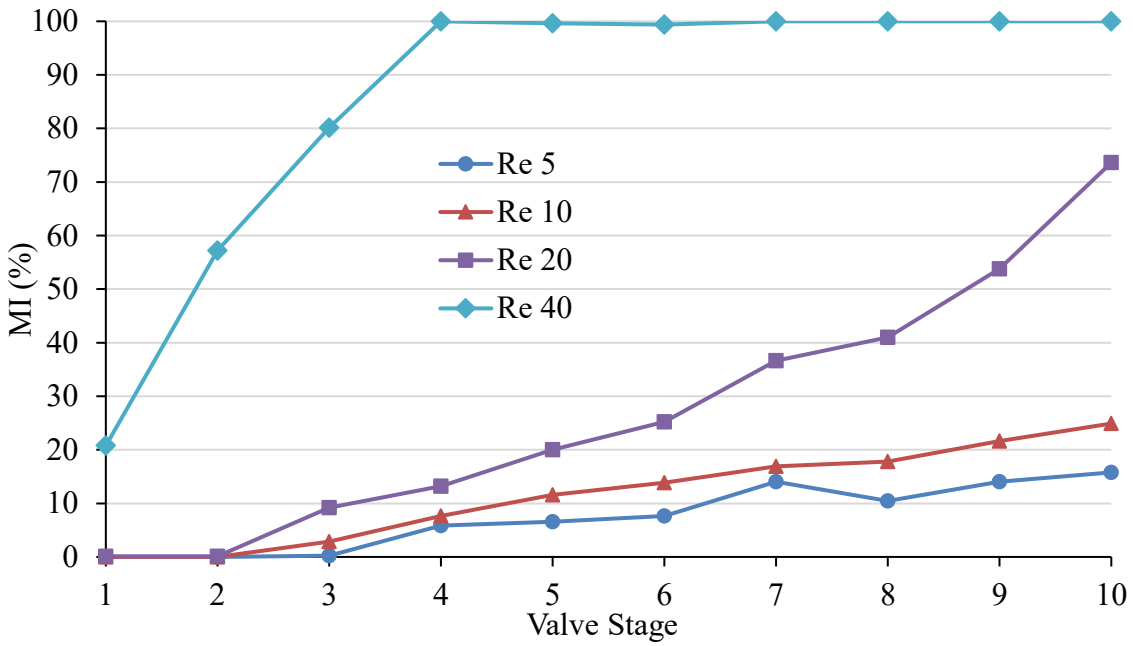

Figure 4.2: Mixing Performance of Tesla Micromixer Based on Increasing Valve Stages at $5 \leq Re \leq 40$

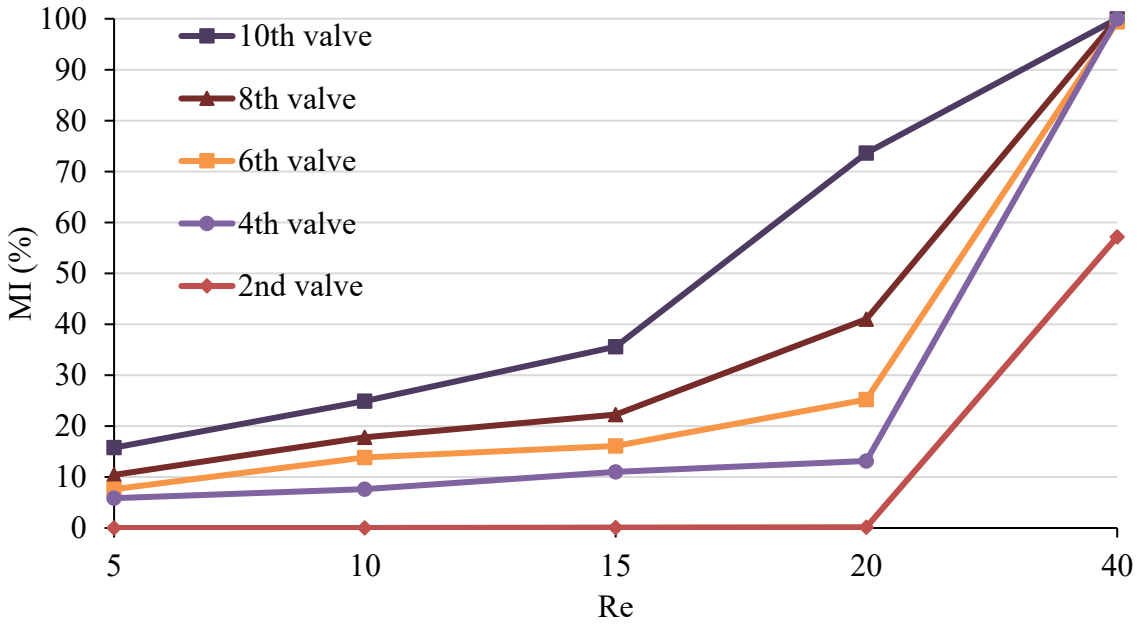

Figure 4.3: Mixing Performance of Tesla Micromixer Based on Increasing Re at Certain Valve Stage

Table 4.2: Mixing Images at the First, Fifth, and Tenth Valve Stages of Tesla Micromixer at $5 \leq Re \leq 40$

No.	Re ± 0.3	Valve Stage		
		First	5th	10th
1.	5	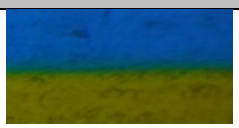 MI = 0%	 MI = 7%	 MI = 16%
2.	10	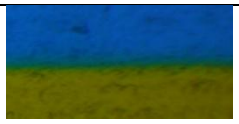 MI = 0%	 MI = 12%	 MI = 25%
3.	15	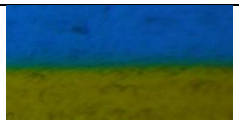 MI = 0%	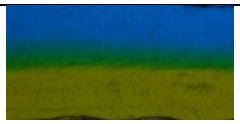 MI = 13%	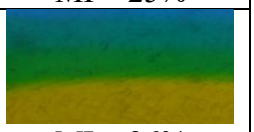 MI = 36%
4.	20	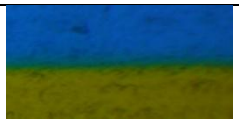 MI = 0.1%	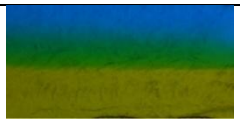 MI = 20%	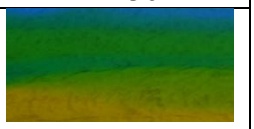 MI = 74%
5.	40	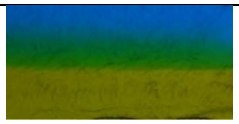 MI = 21%	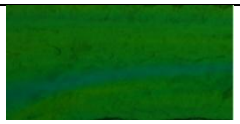 MI = 99%	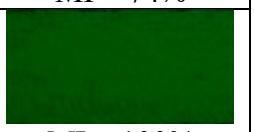 MI = 100%

Observation shows that the valve stage provides the main control for mixing performance at a lower Re range ($5 \leq Re \leq 20$) parallel to the finding by Bhagat and Papautsky (2008). It can be deduced that for $5 \leq Re \leq 20$, the increase of mixing based on valve stage is fairly linear albeit with few fluctuations. However, the correlation is observed to be steeper with some minor non-linearity integrated-in after rising the Re to 20. Interestingly, when the flow shifted to Re = 40, the first valve experienced a sudden large jump from almost zero mixing (0.1%) to 21% mixing index. Thus, there are two flow regimes identified from the experimental observations, which is the low regime ($Re \leq 20$), and the high regime (Re = 40). In the low Re regime, a steady incremental mixing was observed as the flow passed by each stage. Conversely, the high Re regime showed enhanced

mixing at the early stage of the first valve. With the increase of Re, inertial effects in the fluid are expected to grow as compared to viscous forces. The increasing inertial effect in the flowing stream that curls around the helix branch gave rise to a strong reversed-advective current once the branch flow is reunited with the mainstream. This advective current in the reversed direction seemed to become stronger as the Re increased to Re > 20. As the reversed stream became increasingly large, the mixing index showed an incremental rise for the second and third valves. At Re = 40, a fully mixed fluid was achieved in the fourth stage valve.

The helix branch channel introduced a high-speed, reversed jet flow that collides with the main flow stream at the vicinity of converging point of helix channel and main channel. This setting amplifies advection intensively by generating Dean vortices and resulting to the increased of mixing index. This is justified by comparing the performance of the first valve of Tesla micromixer with conventional Y-micromixers with a straight mixing channel by Mahmud and Tamrin (2020) and Shah et al. (2019) as shown in Figure 4.4. Both studies shared the same finding that is that is an increase in Re showed no major increment in the mixing index. Mixing performance was considerably constant throughout $10 \leq Re \leq 100$. In addition, they also possess a considerably unfavourable mixing performance which is MI $\leq$ 50%. In the contrary, the mixing performance of Tesla micromixer increases even at the first valve stage due to the introduction of a high-speed and reversed fluid flow that amplifies advection intensively in the trailing end of the helix branch. This is justified by comparing the performance curves of the first valve of the Tesla micromixer with the one by Mahmud et al. (2021) and Wang et al. (2012b), where the latter consists of no additional curving or bifurcation in the main channel after Y-junction.

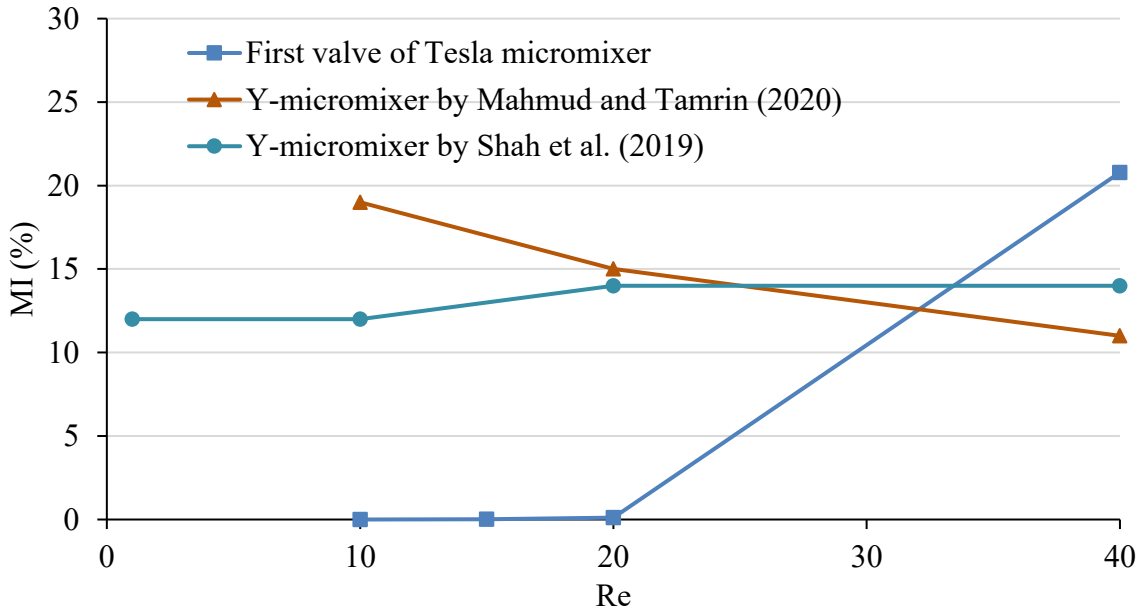

Figure 4.4: Mixing Performance of Conventional Y-micromixers and Tesla Micromixer at $5 \leq Re \leq 40$

4.2.3 Selection of a Suitable Micromixer

Figure 4.5 shows the progressing patterns of mixing performance of T-micromixer with circular mixing channel and Tesla micromixer. For Tesla micromixer, a completely mixed liquid was achieved at the fourth valve stage at Re = 40. On the other hand, T-micromixer with circular mixing channel only demonstrated 57.33% mixing index at the same Re. Micromixer is required to fully mix fluid so that a successful POC unit is realized. However, the present result of fluid mixing performance in T-micromixer with circular mixing channel was not sufficient. Alternatively, Tesla micromixer gave promising result by which a fully mixed liquid is achieved at the fourth valve stage with Re = 40.

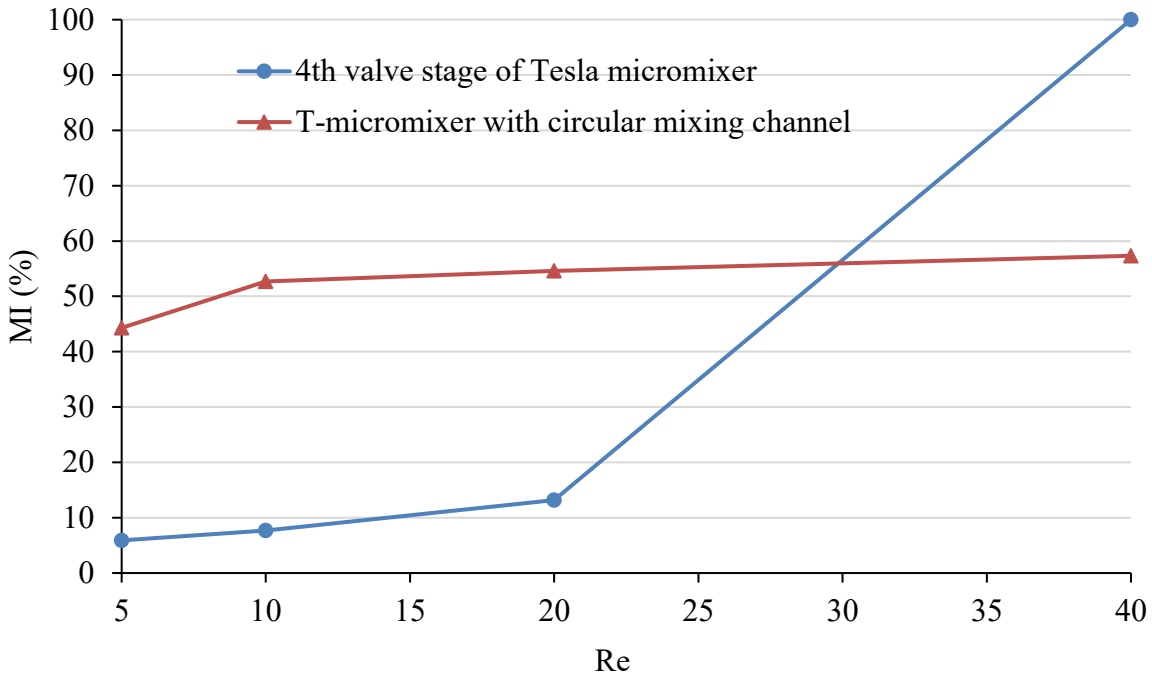

Figure 4.5: Mixing Performance Comparison T-micromixer with Circular Mixing Channel and Tesla Micromixer at $5 \leq Re \leq 40$

4.3 Results and Discussion for Objective 2

4.3.1 Flow Rate Performance of MAPC Micropump

The water absorption capacity, V_{cap} for all paper matrices is shown in Table 4.3. It is noted that the highest water absorption capacity was observed on Type-A paper matrix as compared to the other two. Fluid flow during the absorption process is highly influenced by the adhesive and cohesive forces that are caused by the fluid surface tension and the surface chemistry of the cellulose fibre, respectively (Soum et al., 2019). The liquid also can be absorbed into the internal cavity of the cellulose fibres and within the void volume in the fibre weaving (intra-fibre pores) (Chang et al., 2018).

Table 4.3: Water Absorption Capacity of Each Paper Matrix

No.	Paper matrix	V_{cap} (± σ) (µL)
1.	Type-A (high-absorbing paper tissue)	10.1 (± 0.2)
2.	Type-B (office paper A4-70 g/m^2)	6.9 (± 0.4)
3.	Type-C (SMITH® filter paper-102)	4.4 (± 0.1)

The dynamics of liquid absorption are mainly affected by the internal cavities and intra-fibre pores of the paper matrix used. Qualitatively, in comparison, higher fluid absorption capacity in Type-A paper matrix due to its comparably greater inter-fibre pores as compared to the other types resulting from the uncompressed and widely arranged fibrous cellulose (Figure 4.6). Fluid absorption speed was found to be faster in cellulose fibres with larger internal cavities, and smaller intra-fibre pores per unit volume (Chang & Kim, 2020). This explains the reason why the Type-A paper matrix has the highest fluid absorption capacity although having a smaller fibre size. The effect of intra-fibre pores seemed to dominate and overrule the effect of internal cavities, thus making it capable to absorb more volume of fluid and at a higher flow rate as compared to both Type-B and Type-C paper matrices. This agrees well with the findings on kitchen towel performance by de Assis et al. (2018). In the case of SMITH® filter paper-102 (Type-C), both fibre size and the weaving pore per unit volume are the smallest of the others due to the compactly arranged and densely compressed cellulose fibre weaving (Figure 4.6c) which gives the lowest absorption capacity.

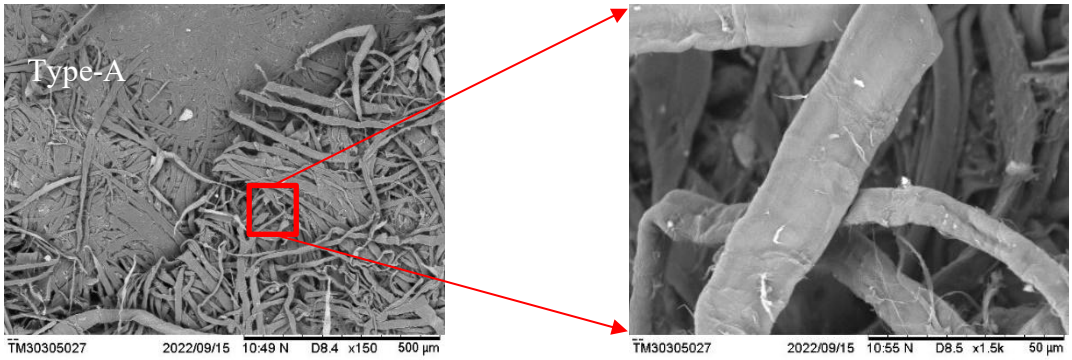

(a)

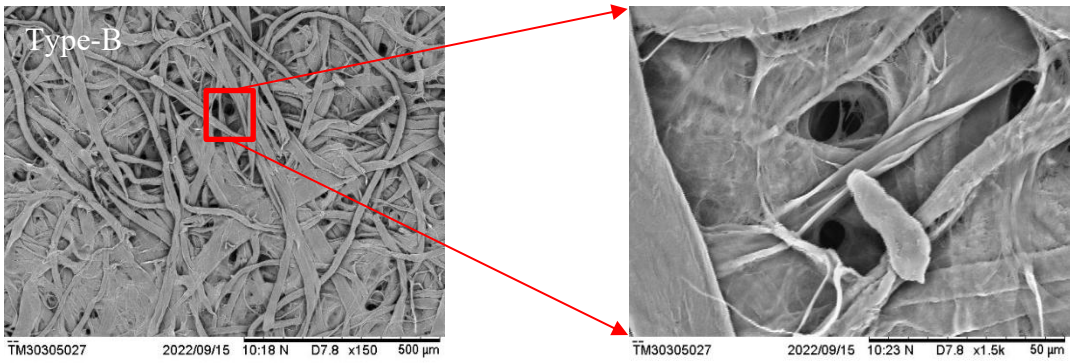

(b)

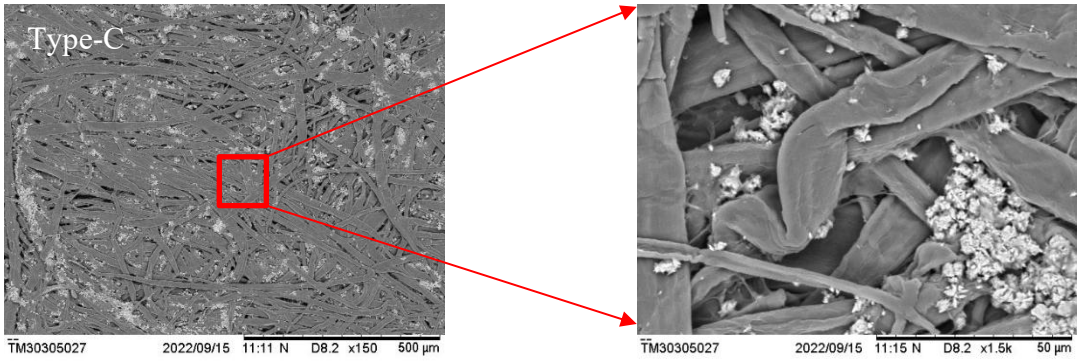

(c)

Figure 4.6: Microscope Images of 150× and 1500× Magnifications for; (a) Type-A, (b) Type-B, and (c) Type-C Paper Matrices

On a levelled platform, the flow rate of MAPC, Q_{MAPC} was increased based on the capillarity of each attached paper matrices (Table 4.4). This setup further enhanced the flow rate when the platform is inclined gradually to 15°, 30°, 45° and 60°.

Table 4.4: Paper-based Capillary and Gravitational Effects on Flow Rate Based on Inclination Angles of the Micropump Platform

No.	Angle (°)	Q_{MAPC} (± σ) (µL/s)		
		Type-A	**Type-B**	**Type-C**
1.	0	3.80 (±0.04)	2.40 (±0.03)	2.30 (±0.03)
2.	15	7.20 (± 0.03)	3.80 (± 0.02)	2.60 (± 0.02)
3.	30	11.20 (± 0.04)	6.00 (± 0.02)	4.00 (± 0.05)
4.	45	18.40 (± 0.03)	9.60(± 0.04)	6.40 (± 0.03)
5.	60	24.40 (± 0.02)	10.80 (± 0.03)	8.90 (± 0.04)

The flow rate performance of the MAPC micropump can be classified into two criteria based on the effects of hydrostatic and paper capillary. In the first criterion, the fluid velocity, V_B at point h_B determines the flow rate, Q_H. For the second criterion, the flow rate of paper capillary, Q_{PC} is affected by an external influence that is initially caused by fluid flow at point h_B, resulting from the hydrostatic effect. This fluid movement that heads towards the paper matrix surface carries along some amount of kinetic energy which eventually gives an extra pushing force into the paper matrix. This made Q_{MAPC} gradually compounding based on the inclination angles, θ. As shown in Figure 4.7, the highest flow rate produced seemed to be comparatively higher than some other capillary and hydrostatic-based micropump designs (Cummins et al., 2017; Wang et al., 2018). The present design has a wide flow rate operating range of 2.3 µL/s ≤ Q ≤ 24.4 µL/s which made it flexible and versatile to cope with any microfluidic unit. A range of paper-based capillary micropump designs by Cummins et al. (2017) reported the maximum flow rate of 0.0917 µL/s was achieved for their parallelly-stacked papers micropump. On the other hand, a hydrostatic pressure-driven micropump design by Wang et al. (2018) reported a maximum flow rate of 18.3 µL/s.

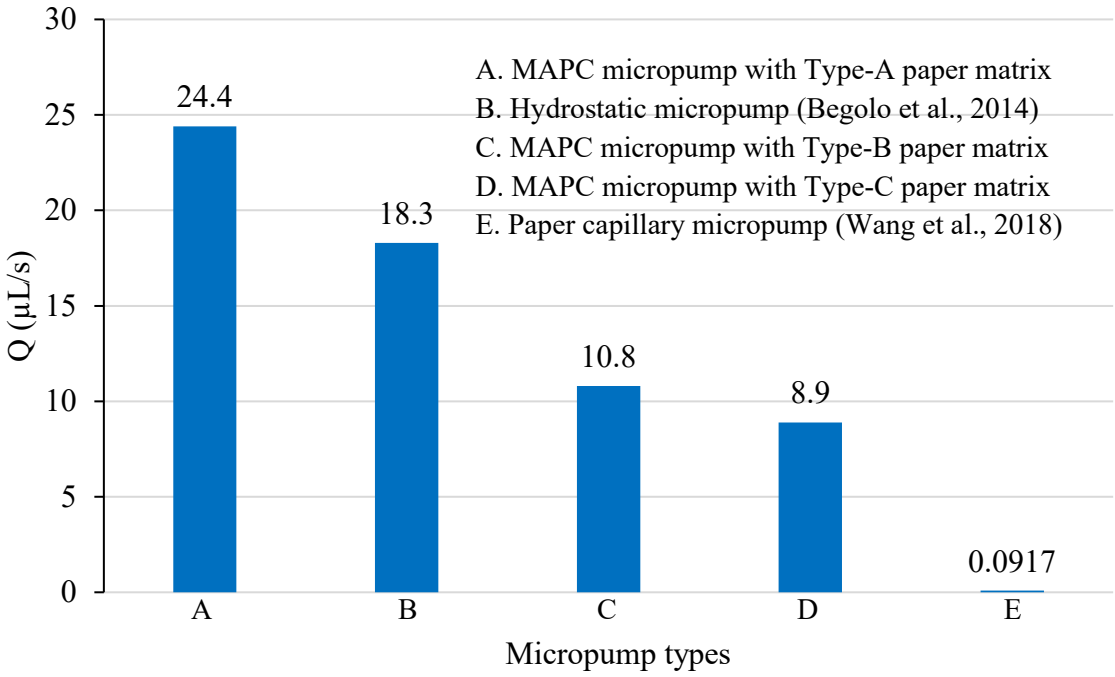

Figure 4.7: Comparison of the Highest Generated Flow Rates of Some Micropump Designs

4.3.2 Flow Rate Performance of SAP Micropump

The operating principle of SAP micropump is actually based on the household siphon pump. It is designed by manipulating the advantage of flexible material such as PDMS as the micropump chamber to produce sub-atmospheric pressure, and the placement of a series of check-valves. During initiation, it was identified that only 60.86% from the overall 23 mL chamber volume was effectively utilized. This can be attributed to the limitation of chamber geometrical shape. By referring to Figure 4.8, the flow rate of a standalone micropump operation is 49.9 µL/s which is comparatively higher than other vacuum-based micropump designs by Begolo et al. (2014) and Li et al. (2012b) due to the sufficiently large volumetric capacity of the existing chamber.

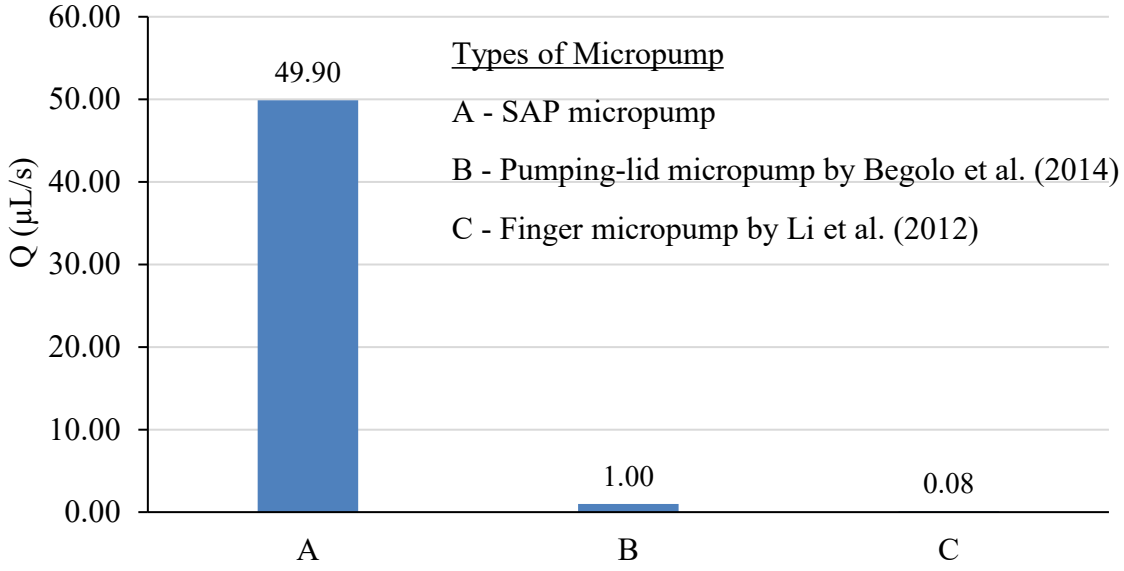

Figure 4.8: Flow Rate Comparison of Vacuum-based Passive Micropumps

4.3.3 Selection of a Suitable Micropump

Flow rate performance of the two developed micropumps is shown in Figure 4.9, with the highest flow rates for the SAP and MAPC micropumps were identified as 49.9 µL/s and 24.4 µL/s, respectively. Additional increase in flow rate can be done by increasing the inclination angle of the MAPC micropump or increasing the chamber volume of the SAP micropump. However, increment of platform inclination of MAPC micropump was found unnecessary due to insignificant increment of flow rate. Due to this limitation, the selection of micropump therefore is resolved to the next alternative which is the optimization of SAP micropump by CFD.

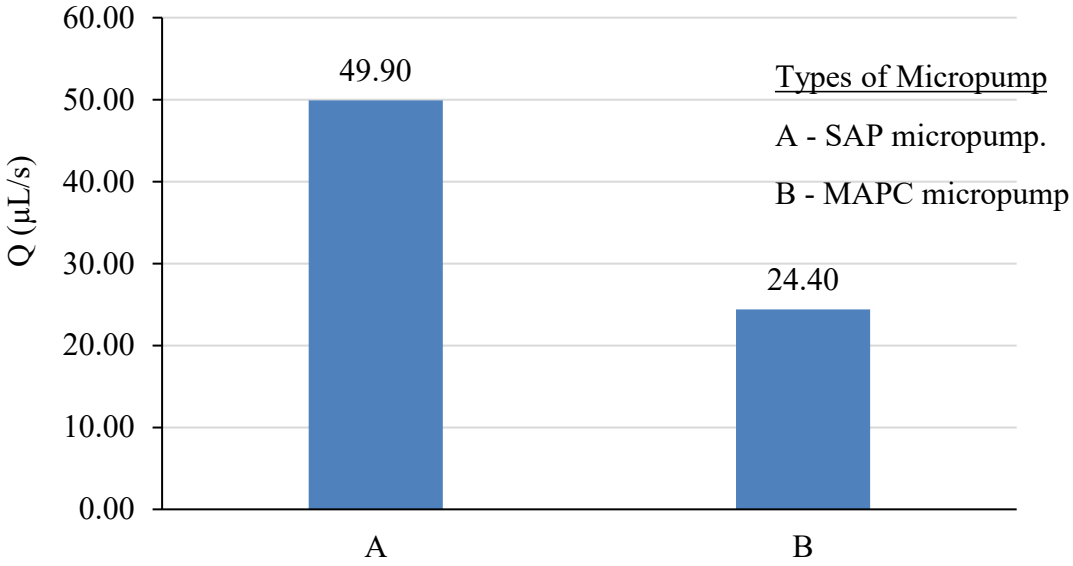

Figure 4.9: Flow Rate Comparison of SAP and MAPC Micropumps

4.4 Results and Discussion for Objective 3

4.4.1 CFD Simulations

Based on the predecessor studies, the range of gauge pressure for the simulations of mass flow in the Tesla micromixer was pre-determined as -10 kPa ≤ $\Delta P_{simulation}$ ≤ -100 kPa. Mixing indices were extracted from the point located downstream after the converging section of the helix and main branches, and calculated based on Equations 3.1, 3.2 and 3.3 in Section 3.2.4.

Mass flow simulations were done in the gauge pressure range of -10 kPa ≤ $\Delta P_{simulation}$ ≤ -100 kPa with the increasing valve stage from 1 to 10. Mass flow and mixing are represented by colour contour as shown in Figure 4.10. The overall mixing performance based on gauge pressure range and valve stages is presented in Table 4.5.

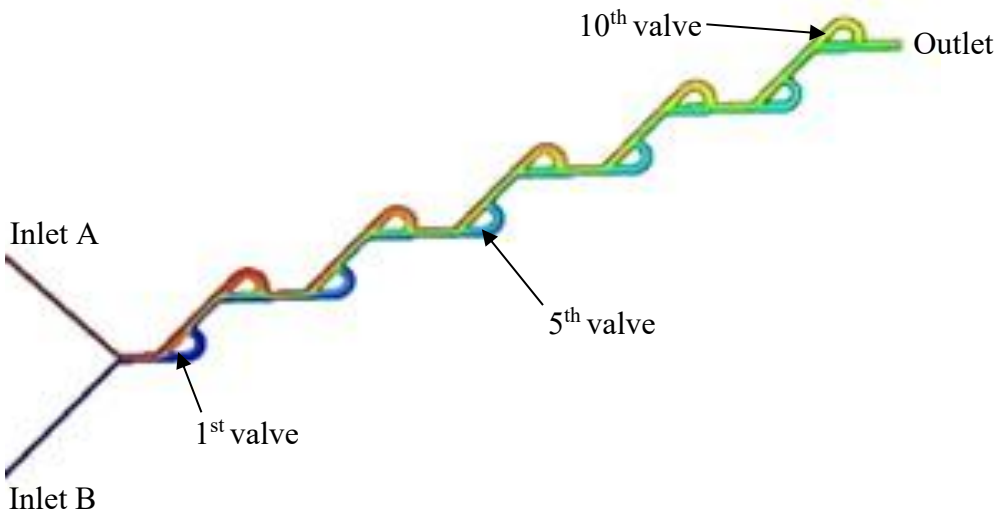

Figure 4.10: 10-stage Tesla Micromixer

Table 4.5: Mixing Performance (in percentage) of Tesla Micromixer Based on Mass Flow Simulations

No.	Valve Stage	$\Delta P_{simulation}$									
		-10 kPa	**-20 kPa**	**-30 kPa**	**-40 kPa**	**-50 kPa**	**-60 kPa**	**-70 kPa**	**-80 kPa**	**-90 kPa**	**-100 kPa**
1.	1st	19.93	13.99	11.13	10.96	10.31	9.44	9.15	7.69	6.77	6.52
2.	2nd	26.20	14.97	13.84	11.89	12.27	11.37	11.09	9.97	9.90	9.51
3.	3rd	31.78	19.91	14.77	12.43	12.69	12.17	11.76	10.41	10.11	10.00
4.	4th	38.76	26.72	15.03	13.67	12.98	12.51	12.47	11.14	10.61	10.53
5.	5th	52.44	28.11	19.85	15.74	14.85	14.26	12.96	12.49	11.65	11.85
6.	6th	61.31	30.30	25.26	20.87	19.53	17.67	14.64	13.10	12.67	12.20
7.	7th	76.43	59.28	30.98	27.97	26.51	25.62	24.49	24.34	23.50	21.00
8.	8th	79.18	60.37	33.76	29.42	27.93	26.56	25.21	25.06	24.33	23.14
9.	9th	98.00	67.27	34.01	30.93	29.15	27.63	26.60	25.86	25.40	24.72
10.	10th	100.0	74.06	38.44	32.10	29.95	28.72	27.62	26.94	26.15	25.81

In the simulations, a distinguishable green coloured fluid stream is formed and intensifies as at each valve stages albeit at any increments of $\Delta P_{simulation}$. For qualitative visualization, only the mass mixing in the first, second, fifth and tenth valves are presented, as in Table 4.6.

Table 4.6: Mixing Images at the First, Second, Fifth and Tenth Valve Stages

No.	Valve Stage	$\Delta P_{simulation}$			Colour Reference
		-10 kPa	-50 kPa	-100 kPa	
1.	First	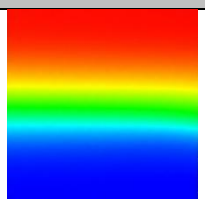	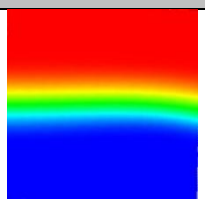	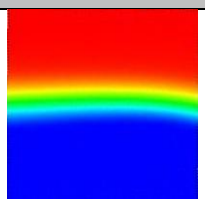	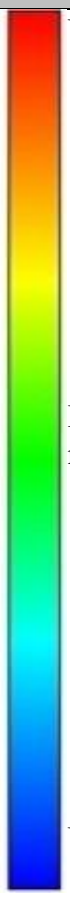 Unmixed (Inlet A)
2.	Second	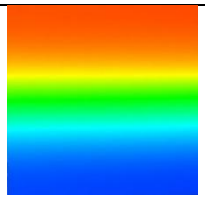	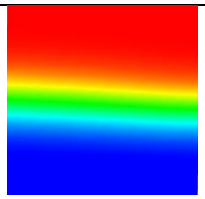	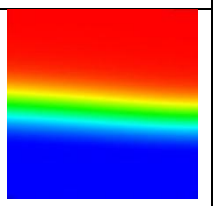	
3.	5th	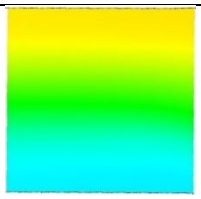	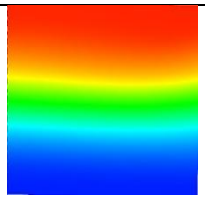	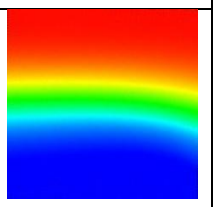	Fully mixed
4.	10th	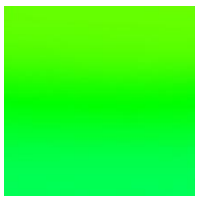	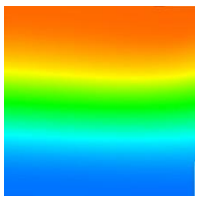	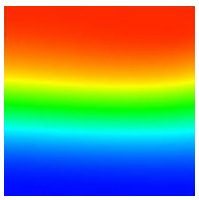	Unmixed (Inlet B)

In Figure 4.11, graph shows an increment of mixing performance from 19.93% in the first valve to 100% mixed in the tenth valve when $\Delta P_{simulation}$ was induced to -10 kPa. The declining of mixing follows gradually when the gauge pressure was increased further from -20 kPa until -100 kPa. In general, similar pattern of declining in mixing index was identified when $\Delta P_{simulation}$ was progressively increased step by step in the interval of -10 kPa. On the other hand, it is identified that lower mixing indices were produced for lesser number of valves for a different gauge pressure reading. Overall, result shows the suitable gauge pressure for a complete fluid mixing was identified as $\Delta P_{simulation}$ = -10 kPa.

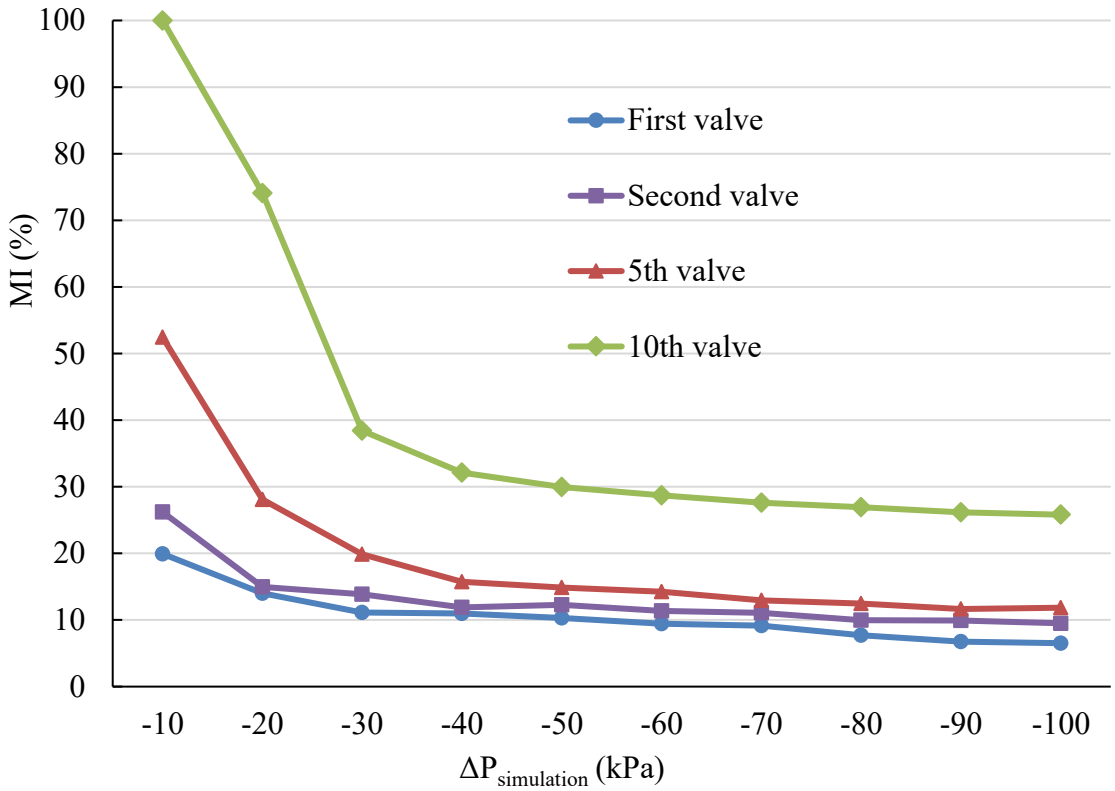

Figure 4.11: Mixing Performance Based on $\Delta P_{simulation}$

Fluid Mixing Mechanism in the Tesla Micromixer

Minor chaotic advection is expected to be created at the trailing end of the helix channel. As the fluid exits the helix branch channel at a certain angle, the flow tries to recombine itself back with the opposing flow stream of the main channel, amplifying the

advection and mixing (Figure 4.12). Each Tesla valve gives a compound effect on the overall mixing performance. The curved rectangular channels in the Tesla micromixer introduced secondary flows in terms of two counter rotating vortices. This effect is caused by the fluid flow that tries to keep attached to the curved surface of the helix branch channel produces pressure gradient imbalance that subsequently leads to secondary flows to form counter-rotating flows that are known as Dean vortices resulting to a minor chaotic advection at the trailing end of the helix branch. This finding also parallel to the ones by (Porwal et al., 2018) and Babaie et al. (2022).

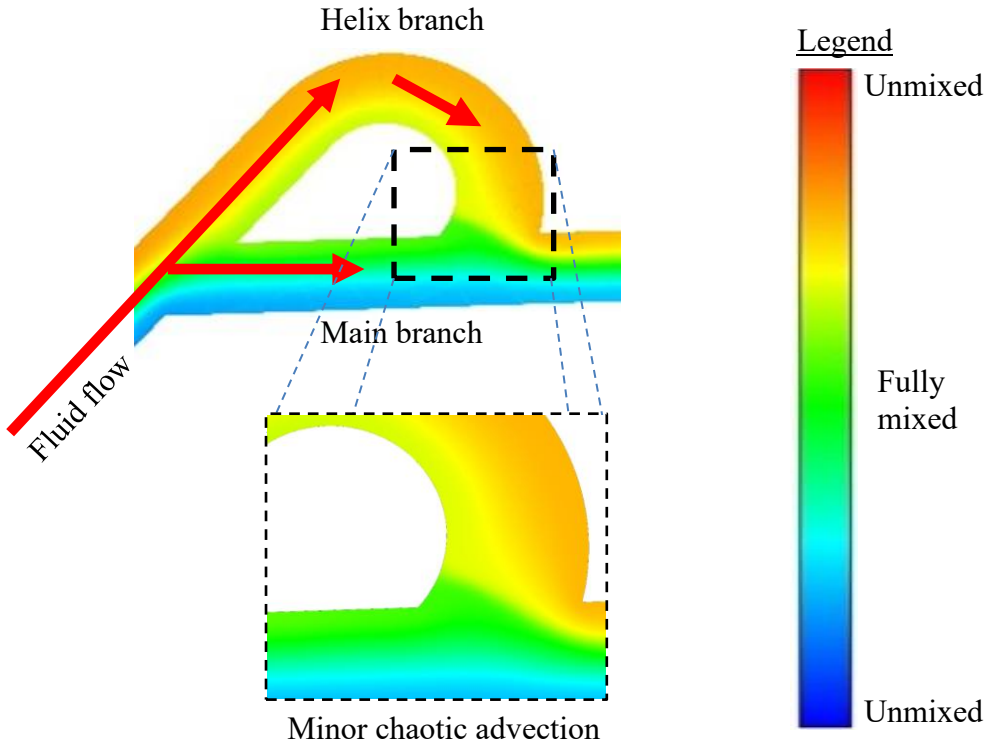

Figure 4.12: Minor Chaotic Advection at the Trailing End of the Helix Branch

4.4.2 Experimental Validation at Optimum Gauge Pressure

Validation tests on the proposed POC unit were conducted based on the setup shown in Figure 4.13. Tests to determine the actual gauge pressure, ΔP_{actual} is shown in Figure 4.14. In terms of statistical validity, with a total number of tests, n = 30, and standard deviation, σ

= 0.28 kPa, retrieved from the test result of the actual gauge pressure, the mean of ΔP_{actual} is within the confidence interval (CI) of; 9.392 kPa ≤ CI ≤ 9.588 kPa which corresponds to the z-score of 1.96 or 95% confidence level.

In the actual SAP micropump chamber, it was identified that only a volume of 14 mL (60.86%) from the overall 23 mL chamber volumetric capacity is effectively utilized during the actual operation due to the physical limitation of the chamber geometrical shape, with the remaining 9 mL volume still consisting of air. This contributes to a pumping efficiency of $\eta = 0.61$, that made the ΔP_{actual} to be slightly lower than $\Delta P_{simulation}$. The difference between ΔP_{sim} and ΔP_{actual} results can be attributed to the followings;

i. In the simulation, inlet pressure was predicted to be in a constant value, but this is not the case during experiment. The generated negative pressure by the SAP micropump decreases with time due to the nature of micropump chamber membrane
ii. Flow resistance contributed by microchannel surface roughness at the microscopic level
iii. Variation in the forces exerted during manual finger pressing of micropump chamber

In overall, the mixing performance between the simulation and experiment compares well despite the deviation of about -0.51 kPa.

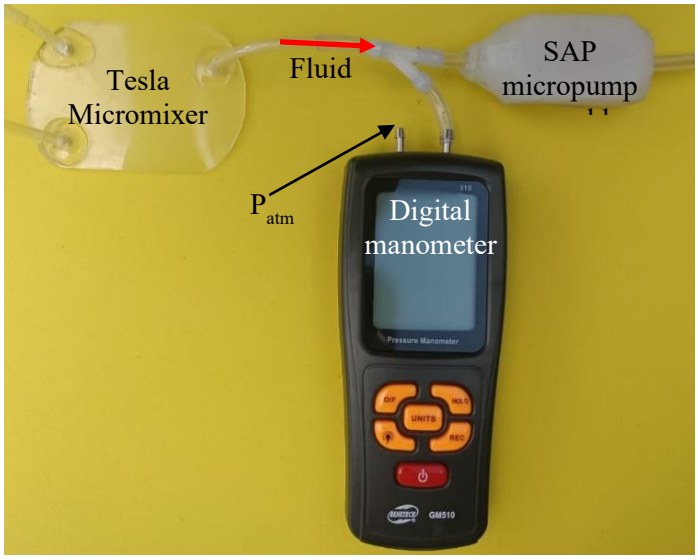

Figure 4.13: Experimental Setup for Gauge Pressure Validation of the Proposed POC Unit

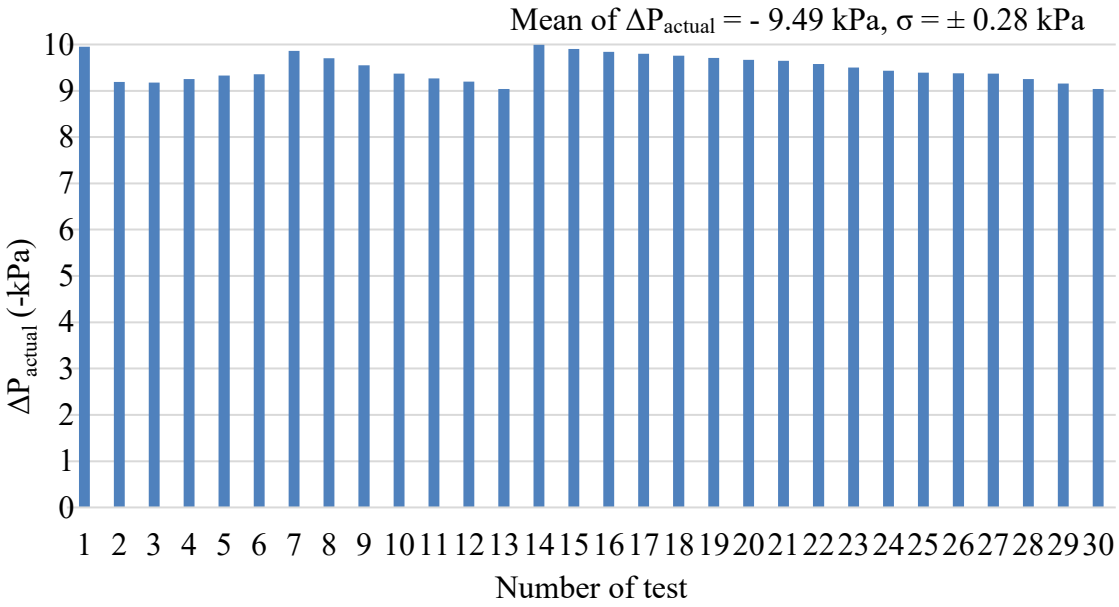

Figure 4.14: Determined ΔP_{actual} from the Proposed POC Unit

In addition, it was also found that after the operation on the POC unit was initiated, ΔP_{actual} seemed to be descending exponentially with time, and ceased after there was no more pressure difference between the micropump chamber and the atmosphere as shown in Figure 4.15.

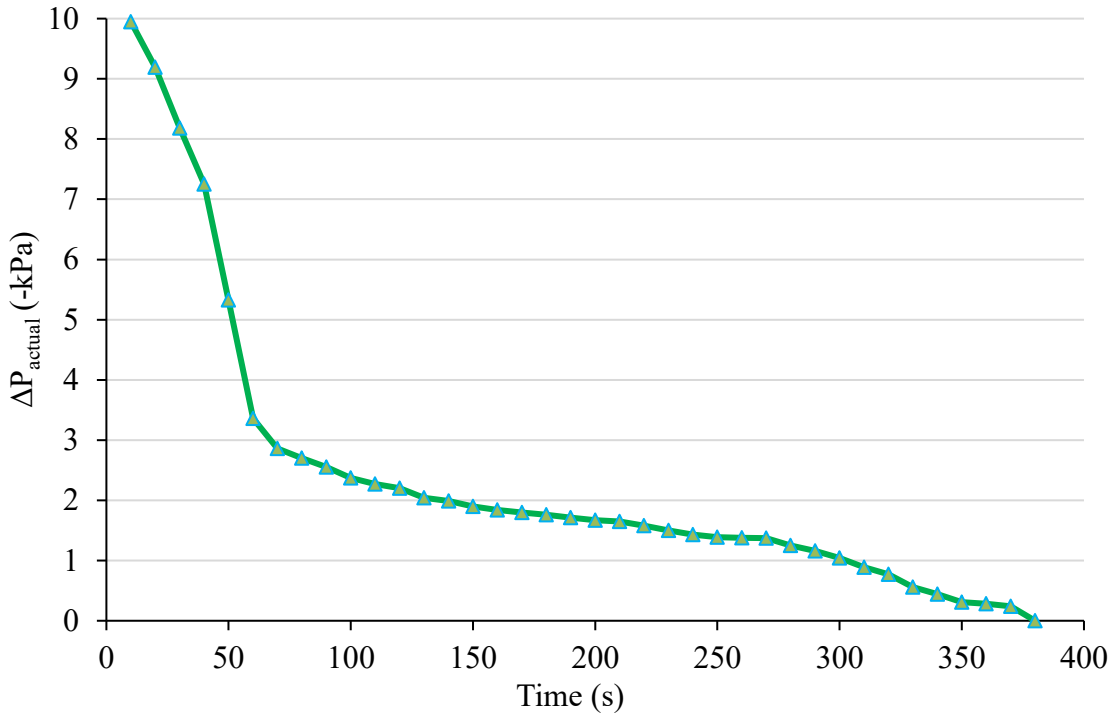

Figure 4.15: Dissipation of ΔP_{actual} Based on Time

4.5 Chapter Summary

This chapter presented the results and discussion related to the integration of Tesla micromixer and SAP micropump as the proposed POC unit. Tesla micromixer achieved a complete fluid mixing at $\Delta P_{simulation}$ = -10 kPa. However, results also showed that mixing performance diminished gradually from 100% to 25.81% for -10 kPa > $\Delta P_{simulation} \geq$ -100 kPa. From the CFD simulations, it was also identified that fluid mixing was caused by the generation of minor chaotic advection and Dean vortices at the trailing end of the helix branch of each valve. In the contrary, an overall pumping efficiency of η = 0.61 was achieved due to the design limitation of the SAP micropump. This limitation subsequently made $\Delta P_{actual} < \Delta P_{simulation}$. In addition, ΔP_{actual} was also found to be diminished with time.

CHAPTER 5

CONCLUSION AND RECOMMENDATIONS

5.1 Conclusion

In the first objective, the mixing performance of two passive micromixers, namely, T-micromixer with circular mixing channel and Tesla micromixer were experimentally characterized based on varying Re. T-micromixer with circular mixing channel was able to acquire a moderate mixing performance of 57.33% at Re = 40. Alternatively, with Tesla micromixer, a fully mixed liquid was obtained at the fourth valve stage of the same Re. Hence, for this reason, Tesla micromixer was selected due to its better performance.

In the second objective, the flow rate performances of SAP and MAPC micropumps were experimentally characterized. Both micropumps are passive-driven and placed at the outlet of a micromixer so that fluid movement was caused by the negative pressure. This had successfully overcome the design limitation for attachment onto a multi-inlet micromixer. In a standalone operation, SAP micropump demonstrates higher flow rate as compared to MAPC micropump that were 49.9 μL/s and 24.4 μL/s, respectively., Therefore, based on this comparison, SAP micropump was selected and integrated with Tesla micromixer as the proposed POC unit.

In the final objective, CFD simulations were used for design optimization of the proposed POC unit and a complete mixing was achievable in the tenth valve stage, at gauge pressure of $\Delta P_{simulation}$ = -10 kPa. Fluid mixing was identified to be caused by the generation of minor chaotic advection at the trailing end of the helix branch of each valve. The physical limitation of the SAP micropump contributes to the overall pumping efficiency of $\eta = 0.61$

which consequently made the measured actual gauge pressure lesser than the simulated gauge pressure. Due to the same physical limitation, the actual gauge pressure was also identified to be diminished with time.

5.2 Recommendations

It is recommended that;

i. Tesla micromixer can be further incorporated with an active mixing element to assist the fluid mixing process. Such element however must be small in size, having a simple circuitry, and empowered by a small power source, so that it still complies to the ASSURED criteria outlined by the World Health Organization

ii. Material with higher elastic strength than PDMS can be used for the micropump chamber membrane so that the overall pumping efficiency can be improved further

iii. The actual gauge pressure of the SAP micropump was found to be reducing with time. This can be improved using a micro-electro-mechanical system for sequential pressing on multiple micropump chambers placed in series to maintain a constant gauge pressure

REFERENCES

Afzal, A., & Kim, K.-Y. (2012). Passive split and recombination micromixer with convergent–divergent walls. *Chemical Engineering Journal, 203*, 182-192.

Afzal, A., & Kim, K.-Y. (2015). Convergent–divergent micromixer coupled with pulsatile flow. *Sensors and Actuators B: Chemical, 211*, 198-205.

Afzal, A., & Kim, K.-Y. (2021). Active and Passive Micromixers. *Analysis and Design Optimization of Micromixers, 32*(3), 11-34.

Aguirre, G. R., Efremov, V., Kitsara, M., & Ducrée, J. (2015). Integrated micromixer for incubation and separation of cancer cells on a centrifugal platform using inertial and dean forces. *Microfluidics and Nanofluidics, 18*, 513-526.

Ahmad, D. A. M. A., Ahmad, J., & Saad, S. (2020). Sarawak Digital Economy and The Organisational Sensemaking Process of CSR: A Conceptual View. *Jurnal Komunikasi: Malaysian Journal of Communication, 36*(1), 12-18.

Ahsanullah, M., Kibria, B. G., & Shakil, M. (2014). *Normal and Student Standard Distributions and Their Applications*. Springer.

Al-Halhouli, A. a., Alshare, A., Mohsen, M., Matar, M., Dietzel, A., & Büttgenbach, S. (2015). Passive micromixers with interlocking semi-circle and omega-shaped modules: Experiments and simulations. *Micromachines, 6*(7), 953-968.

Alam, A., Afzal, A., & Kim, K.-Y. (2014). Mixing performance of a planar micromixer with circular obstructions in a curved microchannel. *Chemical Engineering Research and Design, 92*(3), 423-434.

Alam, A., & Kim, K.-Y. (2013). Mixing performance of a planar micromixer with circular chambers and crossing constriction channels. *Sensors and Actuators B: Chemical, 176*, 639-652.

Ansari, M. A., Kim, K.-Y., Anwar, K., & Kim, S. M. (2010). A novel passive micromixer based on unbalanced splits and collisions of fluid streams. *Journal of Micromechanics and Microengineering, 20*(5), 55007.

Asadi Dereshgi, H., Dal, H., & Yildiz, M. Z. (2021). Piezoelectric micropumps: State of the art review. *Microsystem Technologies*, *1*, 1-29.

Babaie, Z., Bahrami, D., & Bayareh, M. (2022). Investigation of a novel serpentine micromixer based on Dean flow and separation vortices. *Meccanica*, *1*, 1-14.

Balbino, T. A., Azzoni, A. R., & de La Torre, L. G. (2013). Microfluidic devices for continuous production of pDNA/cationic liposome complexes for gene delivery and vaccine therapy. *Colloids and Surfaces B: Biointerfaces, 111*, 203-210.

Bayareh, M., Ashani, M. N., & Usefian, A. (2020). Active and passive micromixers: A comprehensive review. *Chemical Engineering and Processing-Process Intensification, 147*, 107771.

Begolo, S., Zhukov, D. V., Selck, D. A., Li, L., & Ismagilov, R. F. (2014). The pumping lid: investigating multi-material 3D printing for equipment-free, programmable generation of positive and negative pressures for microfluidic applications. *Lab on a Chip, 14*(24), 4616-4628.

Bhagat, A. A. S., & Papautsky, I. (2008). Enhancing particle dispersion in a passive planar micromixer using rectangular obstacles. *Journal of Micromechanics and Microengineering, 18*(8), 85005.

BIPM, I., IFCC, I., ISO, I., & IUPAP, O. (2008). *Evaluation of measurement data—guide to the expression of uncertainty in measurement, JCGM 100: 2008 GUM 1995 with minor corrections*. Joint Committee for Guides in Metrology.

Cai, G., Xue, L., Zhang, H., & Lin, J. (2017). A review on micromixers. *Micromachines, 8*(9), 274.

Chang, S., & Kim, W. (2020). Dynamics of water imbibition through paper with swelling. *Journal of Fluid Mechanics, 892*, A39.

Chang, S., Seo, J., Hong, S., Lee, D.-G., & Kim, W. (2018). Dynamics of liquid imbibition through paper with intra-fibre pores. *Journal of Fluid Mechanics, 845*, 36-50.

Chen, X., & Zhao, Z. (2017). Numerical investigation on layout optimization of obstacles in a three-dimensional passive micromixer. *Analytica Chimica Acta, 964*, 142-149.

Choi, J. Y., Kim, Y. T., Byun, J.-Y., Ahn, J., Chung, S., Gweon, D.-G., & Seo, T. S. (2012). An integrated allele-specific polymerase chain reaction-microarray chip for multiplex single nucleotide polymorphism typing. *Lab on a Chip, 12*(24), 5146-5154.

Chung, Y.-C., Hsu, Y.-L., Jen, C.-P., Lu, M.-C., & Lin, Y.-C. (2004). Design of passive mixers utilizing microfluidic self-circulation in the mixing chamber. *Lab on a Chip, 4*(1), 70-77.

Cohen, J. (2013). *Statistical power analysis for the behavioral sciences*. Routledge.

Cosentino, A., Madadi, H., Vergara, P., Vecchione, R., Causa, F., & Netti, P. A. (2015). An efficient planar accordion-shaped micromixer: from biochemical mixing to biological application. *Scientific Reports, 5*(1), 17876.

Cummins, B. M., Chinthapatla, R., Lenin, B., Ligler, F. S., & Walker, G. M. (2017). Modular pumps as programmable hydraulic batteries for microfluidic devices. *Technology, 5*(1), 21-30.

de Assis, T., Reisinger, L. W., Dasmohapatra, S., Pawlak, J., Jameel, H., Pal, L., & Gonzalez, R. W. (2018). Performance and sustainability vs. the shelf price of tissue paper kitchen towels. *Bio Resources, 13*(3), 6868-6892.

dos Santos, A. A. C., Childs, M., Nguyen, T. D., & Hassan, Y. (2019). Convergence study and uncertainty quantification of average and statistical PIV measurements in a matched refractive index 5× 5 rod bundle with mixing vane spacer grid. *Experimental Thermal and Fluid Science, 102*, 215-231.

Femmer, T., Eggersdorfer, M. L., Kuehne, A. J., & Wessling, M. (2015). Efficient gas–liquid contact using microfluidic membrane devices with staggered herringbone mixers. *Lab on a Chip, 15*(15), 3132-3137.

Feng, Q., Chen, X., Wang, X., Yu, X., Zeng, X., Ma, Y., & Wang, Q. (2021). Numerical simulation of a three dimensional electroosmotic micromixer with a flexible and controllable Rubik's cube module. *International Communications in Heat and Mass Transfer, 127*, 105482.

Field, A. (2024). *Discovering statistics using IBM SPSS statistics*. Sage Publications Limited.

Forster, F. K., Bardell, R. L., Afromowitz, M. A., Sharma, N. R., & Blanchard, A. (1995). Design, fabrication and testing of fixed-valve micro-pumps. *ASME-Publications-Fed, 234*, 39-44.

Gamboa, A. R., Morris, C. J., & Forster, F. K. (2005). Improvements in fixed-valve micropump performance through shape optimization of valves. *Journal of Fluids Engineering, 127*(2), 339-346.

Gao, Y., Tran, P., Petkovic-Duran, K., Swallow, T., & Zhu, Y. (2015). Acoustic micromixing increases antibody-antigen binding in immunoassays. *Biomedical Microdevices, 17*, 1-5.

Geissler, M., Li, K., Zhang, X., Clime, L., Robideau, G. P., Bilodeau, G. J., & Veres, T. (2014). Integrated air stream micromixer for performing bioanalytical assays on a plastic chip. *Lab on a Chip, 14*(19), 3750-3761.

Gervais, L., Hitzbleck, M., & Delamarche, E. (2011). Capillary-driven multiparametric microfluidic chips for one-step immunoassays. *Biosensors and Bioelectronics, 27*(1), 64-70.

Gobby, D., Angeli, P., & Gavriilidis, A. (2001). Mixing characteristics of T-type microfluidic mixers. *Journal of Micromechanics and Microengineering, 11*(2), 126.

Guo, X., Li, J., Yang, K., Fu, H., Wang, T., Guo, Y., & Huang, W. (2018). Optimal design and performance analysis of hydraulic ram pump system. *Proceedings of the Institution of Mechanical Engineers, Part A: Journal of Power and Energy, 232*(7), 841-855.

Gurkan, U. A., Wood, D. K., Carranza, D., Herbertson, L. H., Diamond, S. L., Du, E., & Papautsky, I. (2024). Next generation microfluidics: fulfilling the promise of lab-on-a-chip technologies. *Lab on a Chip, 24*(7), 1867-1874.

Heshmatnezhad, F., Aghaei, H., & Nazar, A. R. S. (2017). Parametric study of obstacle geometry effect on mixing performance in a convergent-divergent micromixer with sinusoidal walls. *Chemical Product and Process Modeling, 12*(1), 12-14.

Hitzbleck, M., Gervais, L., & Delamarche, E. (2011). Controlled release of reagents in capillary-driven microfluidics using reagent integrators. *Lab on a Chip, 11*(16), 2680-2685.

Holstein, C. A., Chevalier, A., Bennett, S., Anderson, C. E., Keniston, K., Olsen, C., & Fu, E. (2016). Immobilizing affinity proteins to nitrocellulose: a toolbox for paper-based assay developers. *Analytical and Bioanalytical Chemistry, 408*, 1335-1346.

Hong, C.-C., Choi, J.-W., & Ahn, C. H. (2004). A novel in-plane passive microfluidic mixer with modified Tesla structures. *Lab on a Chip, 4*(2), 109-113.

Hong, Y., Wu, M., Chen, G., Dai, Z., Zhang, Y., Chen, G., & Dong, X. (2016). 3D printed microfluidic device with microporous Mn2O3-modified screen printed electrode for real-time determination of heavy metal ions. *ACS Applied Materials & Interfaces, 8*(48), 32940-32947.

Hossain, S., Ansari, M. A., Husain, A., & Kim, K.-Y. (2010). Analysis and optimization of a micromixer with a modified Tesla structure. *Chemical Engineering Journal, 158*(2), 305-314.

Hossain, S., Husain, A., & Kim, K.-Y. (2011). Optimization of micromixer with staggered herringbone grooves on top and bottom walls. *Engineering Applications of Computational Fluid Mechanics, 5*(4), 506-516.

Hossain, S., & Kim, K.-Y. (2014). Mixing analysis of passive micromixer with unbalanced three-split rhombic sub-channels. *Micromachines, 5*(4), 913-928.

Howell Jr, P. B., Mott, D. R., Golden, J. P., & Ligler, F. S. (2004). Design and evaluation of a Dean vortex-based micromixer. *Lab on a Chip, 4*(6), 663-669.

Jung, J. H., Kim, G.-Y., & Seo, T. S. (2011). An integrated passive micromixer–magnetic separation–capillary electrophoresis microdevice for rapid and multiplex pathogen detection at the single-cell level. *Lab on a Chip, 11*(20), 3465-3470.

Kai, J., Puntambekar, A., Santiago, N., Lee, S. H., Sehy, D. W., Moore, V., & Ahn, C. H. (2012). A novel microfluidic microplate as the next generation assay platform for enzyme linked immunoassays (ELISA). *Lab on a Chip, 12*(21), 4257-4262.

Kelley, C., Bernholc, J., Briggs, E., Hamilton, S., Lin, L., & Yang, C. (2020). Mesh independence of the generalized Davidson algorithm. *Journal of Computational Physics, 409*, 109322.

Kim, H.-S., Kim, H.-O., & Kim, Y.-J. (2018). Effect of electrode configurations on the performance of electro-hydrodynamic micromixer. *Lab on a Chip, 22*(3), 8229-8300.

Kokalj, T., Park, Y., Vencelj, M., Jenko, M., & Lee, L. P. (2014). Self-powered imbibing microfluidic pump by liquid encapsulation: SIMPLE. *Lab on a Chip, 14*(22), 4329-4333.

Kost, G. J., & Zadran, A. (2019). Schools of Public Health Should be Accredited for, and Teach the Principles and Practice of Point-of-Care Testing. *Journal of Applied Laboratory Medicine, 4*(2), 278-283.

Le The, H., Tran-Minh, N., Le-Thanh, H., & Karlsen, F. (2014). A novel micromixer with multimixing mechanisms for high mixing efficiency at low Reynolds number. *Chemical, 153*, 277-302.

Lee, C.-Y., & Fu, L.-M. (2018). Recent advances and applications of micromixers. *Sensors and Actuators B: Chemical, 259*, 677-702.

Lee, T. Y., Hyun, K.-A., Kim, S.-I., & Jung, H.-I. (2017). An integrated microfluidic chip for one-step isolation of circulating tumor cells. *Sensors and Actuators B: Chemical, 238*, 1144-1150.

Li, G., Luo, Y., Chen, Q., Liao, L., & Zhao, J. (2012a). A "place n play" modular pump for portable microfluidic applications. *Biomicrofluidics, 6*(1), 14118.

Li, W., Chen, T., Chen, Z., Fei, P., Yu, Z., Pang, Y., & Huang, Y. (2012b). Squeeze-chip: a finger-controlled microfluidic flow network device and its application to biochemical assays. *Lab on a Chip, 12*(9), 1587-1590.

Li, X., Chang, H., Liu, X., Ye, F., & Yuan, W. (2015). A 3-D overbridge-shaped micromixer for fast mixing over a wide range of reynolds numbers. *Journal of Microelectromechanical Systems, 24*(5), 1391-1399.

Li, Y., Xu, F., Liu, C., Xu, Y., Feng, X., & Liu, B.-F. (2013). A novel microfluidic mixer based on dual-hydrodynamic focusing for interrogating the kinetics of DNA–protein interaction. *Analyst, 138*(16), 4475-4482.

Liang, D. Y., Tentori, A. M., Dimov, I. K., & Lee, L. P. (2011). Systematic characterization of degas-driven flow for poly (dimethylsiloxane) microfluidic devices. *Biomicrofluidics, 5*(2), 24108.

Lin, Y.-H., Wang, C.-C., & Lei, K. F. (2014). Bubble-driven mixer integrated with a microfluidic bead-based ELISA for rapid bladder cancer biomarker detection. *Biomedical Microdevices, 16*, 199-207.

Liu, C., Li, Y., Li, Y., Chen, P., Feng, X., Du, W., & Liu, B.-F. (2016). Rapid three-dimensional microfluidic mixer for high viscosity solutions to unravel earlier folding kinetics of G-quadruplex under molecular crowding conditions. *Talanta, 149*, 237-243.

Liu, R. (2000). A Passive Three-Dimensional 'C-shape' Herical Micromixer. *Journal of Microelectromechanical System, 9*, 190-197.

Lounsbury, J. A., Karlsson, A., Miranian, D. C., Cronk, S. M., Nelson, D. A., Li, J., & Landers, J. P. (2013). From sample to PCR product in under 45 minutes: a polymeric integrated microdevice for clinical and forensic DNA analysis. *Lab on a Chip, 13*(7), 1384-1393.

Lv, H., Chen, X., Wang, X., Zeng, X., & Ma, Y. (2022). A novel study on a micromixer with Cantor fractal obstacle through grey relational analysis. *International Journal of Heat and Mass Transfer, 183*, 122159.

Mahmud, F., & Tamrin, K. (2020). Method for determining mixing index in microfluidics by RGB color model. *Asia-Pacific Journal of Chemical Engineering, 5*(2), 2407.

Mahmud, F., Tamrin, K., Mohamaddan, S., & Watanabe, N. (2021). Effect of Thermal Energy and Ultrasonication on Mixing Efficiency in Passive Micromixers. *Processes, 9*(5), 891.

Mahmud, F., Tamrin, K., & Sheikh, N. (2020). A Review of Enhanced Micromixing Techniques in Microfluidics for the Application in Wastewater Analysis. *Advances in Waste Processing Technology, 2*(5), 1-22.

Matsunaga, T., Lee, H.-J., & Nishino, K. (2013). An approach for accurate simulation of liquid mixing in a T-shaped micromixer. *Lab on a Chip, 13*(8), 1515-1521.

Modarres, P., & Tabrizian, M. (2020). Phase-controlled field-effect micromixing using AC electroosmosis. *Microsystems & Nanoengineering, 6*(1), 1-11.

Mohammadzadeh, K., Kolahdouz, E., Shirani, E., & Shafii, M. (2013). Numerical Investigation on the effect of the size and number of stages on the Tesla microvalve efficiency. *Journal of Mechanics, 29*(3), 527-534.

Mukherji, S., & Mondal, D. (2017). Lab-on-chip (LOC) devices for point of care (POC) applications. *Medical Biosensors for Point of Care (POC) Applications, 2*(3), 99-131.

Nason, F., Morganti, E., Collini, C., Ress, C., Bersini, S., Pennati, G., & Banfi, G. (2011). Design of microfluidic devices for drug screening on in-vitro cells for osteoporosis therapies. *Microelectronic Engineering, 88*(8), 1801-1806.

Nguyen, N.-T., Wereley, S. T., & Shaegh, S. A. M. (2019). *Fundamentals and applications of microfluidics*: Artech House.

Nilghaz, A., Ballerini, D. R., & Shen, W. (2013). Exploration of microfluidic devices based on multi-filament threads and textiles: A review. *Biomicrofluidics, 7*(5), 3-8.

Nivedita, N., Ligrani, P., & Papautsky, I. (2017). Dean flow dynamics in low-aspect ratio spiral microchannels. *Scientific Reports, 7*, 44072.

Olanrewaju, A., Beaugrand, M., Yafia, M., & Juncker, D. (2018). Capillary microfluidics in microchannels: from microfluidic networks to capillaric circuits. *Lab on a Chip, 18*(16), 2323-2347.

Petkovic, K., Metcalfe, G., Chen, H., Gao, Y., Best, M., Lester, D., & Zhu, Y. (2017). Rapid detection of Hendra virus antibodies: an integrated device with nanoparticle assay and chaotic micromixing. *Lab on a Chip, 17*(1), 169-177.

Pittman, T. W., Decsi, D. B., Punyadeera, C., & Henry, C. S. (2023). Saliva-based microfluidic point-of-care diagnostic. *Theranostics, 13*(3), 1091.

Porwal, P. R., Thompson, S. M., Walters, D. K., & Jamal, T. (2018). Heat transfer and fluid flow characteristics in multistaged Tesla valves. *Numerical Heat Transfer, Part A: Applications, 73*(6), 347-365.

Qian, J.-y., Wu, J.-y., Gao, Z.-x., Wu, A., & Jin, Z.-j. (2019a). Hydrogen decompression analysis by multi-stage Tesla valves for hydrogen fuel cell. *International Journal of Hydrogen Energy, 44*(26), 13666-13674.

Qian, J. Y., Chen, M. R., Liu, X. L., & Jin, Z. J. (2019b). A numerical investigation of the flow of nanofluids through a micro Tesla valve. *Journal of Zhejiang University-Science A, 20*(1), 50-60.

Rafeie, M., Welleweerd, M., Hassanzadeh-Barforoushi, A., Asadnia, M., Olthuis, W., & Ebrahimi Warkiani, M. (2017). An easily fabricated three-dimensional threaded lemniscate-shaped micromixer for a wide range of flow rates. *Biomicrofluidics, 11*(1), 3455-3490.

Rajabi, N., Bahnemann, J., Tzeng, T.-N., Barradas, O. P., Zeng, A.-P., & Müller, J. (2014). Lab-on-a-chip for cell perturbation, lysis, and efficient separation of sub-cellular components in a continuous flow mode. *Sensors and Actuators A: Physical, 215*, 136-143.

Ringkai, H., Tamrin, K., Sheikh, N., & Barroy, P. (2021a). Characterization of dissimilar liquids mixing in T-junction and offset T-junction microchannels. *Proceedings of the Institution of Mechanical Engineers, Part E: Journal of Process Mechanical Engineering*, 9544089211015476.

Ringkai, H., Tamrin, K., Sheikh, N., & Mohamaddan, S. (2021b). Evolution of Water-in-Oil Droplets in T-Junction Microchannel by Micro-PIV. *Applied Sciences, 11*(11), 5289.

Rudyak, V., & Minakov, A. (2014). Modeling and optimization of Y-type micromixers. *Micromachines, 5*(4), 886-912.

Sachdeva, S., Davis, R. W., & Saha, A. K. (2021). Microfluidic point-of-care testing: commercial landscape and future directions. *Frontiers in Bioengineering and Biotechnology, 8*, 602659.

Safavieh, R., & Juncker, D. (2013). Capillarics: pre-programmed, self-powered microfluidic circuits built from capillary elements. *Lab on a Chip, 13*(21), 4180-4189.

Shah, I., Kim, S. W., Kim, K., Doh, Y. H., & Choi, K. H. (2019). Experimental and numerical analysis of Y-shaped split and recombination micro-mixer with different mixing units. *Chemical Engineering Journal, 358*, 691-706.

Shamloo, A., Vatankhah, P., & Akbari, A. (2017). Analyzing mixing quality in a curved centrifugal micromixer through numerical simulation. *Chemical Engineering and Processing: Process Intensification, 116*, 9-16.

Shangguan, J.-W., Liu, Y., Wang, S., Hou, Y.-X., Xu, B.-Y., Xu, J.-J., & Chen, H.-Y. (2018). Paper capillary enables effective sampling for microfluidic paper analytical devices. *ACS Sensors, 3*(7), 1416-1423.

Soum, V., Park, S., Brilian, A. I., Kwon, O.-S., & Shin, K. (2019). Programmable paper-based microfluidic devices for biomarker detections. *Micromachines, 10*(8), 516.

Stroock, A. D., Dertinger, S. K., Ajdari, A., Mezić, I., Stone, H. A., & Whitesides, G. M. (2002). Chaotic mixer for microchannels. *Science, 295*(5555), 647-651.

Thompson, S. M., Paudel, B., Jamal, T., & Walters, D. (2014). Numerical investigation of multistaged tesla valves. *Journal of Fluids Engineering, 136*(8), 81102.

Tian, T., Zhang, H.-X., He, C.-P., Fan, S., Zhu, Y.-L., Qi, C., & Tannous, B. A. (2018). Surface functionalized exosomes as targeted drug delivery vehicles for cerebral ischemia therapy. *Biomaterials, 150*, 137-149.

Tran-Minh, N., Dong, T., & Karlsen, F. (2014). An efficient passive planar micromixer with ellipse-like micropillars for continuous mixing of human blood. *Computer Methods and Programs in Biomedicine, 117*(1), 20-29.

Truong, T., & Nguyen, N. (2003). Simulation and optimization of Tesla valves. *Nanotech, 1*, 178-181.

Viktorov, V., Mahmud, M. R., & Visconte, C. (2016). Numerical study of fluid mixing at different inlet flow-rate ratios in Tear-drop and Chain micromixers compared to a new HC passive micromixer. *Engineering Applications of Computational Fluid Mechanics, 10*(1), 182-192.

Wang, D., Chan, H. N., Liu, Z., Micheal, S., Li, L., Baniani, D. B., & Wu, H. (2020). Recent developments in microfluidic-based point-of-care testing (POCT) diagnoses. *Nanotechnology and Microfluidics, 17*(2), 239-280.

Wang, L., Kodzius, R., Yi, X., Li, S., Hui, Y. S., & Wen, W. (2012a). Prototyping chips in minutes: Direct Laser Plotting (DLP) of functional microfluidic structures. *Sensors and Actuators B: Chemical, 168*, 214-222.

Wang, L., Liu, D., Wang, X., & Han, X. (2012b). Mixing enhancement of novel passive microfluidic mixers with cylindrical grooves. *Chemical Engineering Science, 81*, 157-163.

Wang, L., Ma, S., Wang, X., Bi, H., & Han, X. (2014). Mixing enhancement of a passive microfluidic mixer containing triangle baffles. *Asia-Pacific Journal of Chemical Engineering, 9*(6), 877-885.

Wang, X., Yang, L., & Sun, F. (2021). CFD analysis and RSM optimization of obstacle layout in Tesla micromixer. *International Journal of Chemical Reactor Engineering, 19*(10), 1045-1055.

Wang, X., Zhao, D., Phan, D. T., Liu, J., Chen, X., Yang, B., & Lee, A. P. (2018). A hydrostatic pressure-driven passive micropump enhanced with siphon-based autofill function. *Lab on a Chip, 18*(15), 2167-2177.

Wang, Y.-N., & Fu, L.-M. (2018). Micropumps and biomedical applications–A review. *Microelectronic Engineering, 195*, 121-138.

Wang, Z., Han, T., Jeon, T.-J., Park, S., & Kim, S. M. (2013). Rapid detection and quantification of bacteria using an integrated micro/nanofluidic device. *Sensors and Actuators B: Chemical, 178*, 683-688.

Washburn, E. W. (1921). The dynamics of capillary flow. *Physical review, 17*(3), 273.

Wong, S. H., Ward, M. C., & Wharton, C. W. (2004). Micro T-mixer as a rapid mixing micromixer. *Sensors and Actuators B: Chemical, 100*(3), 359-379.

Wootton, R., Craig, J., & Patterson, V. (2017). *Introduction to telemedicine*. CRC Press.

Wu, C.-Y., & Tsai, R.-T. (2013). Fluid mixing via multidirectional vortices in converging–diverging meandering microchannels with semi-elliptical side walls. *Chemical Engineering Journal, 217*, 320-328.

Xing, S., Jiang, J., & Pan, T. (2013). Interfacial microfluidic transport on micropatterned superhydrophobic textile. *Lab on a Chip, 13*(10), 1937-1947.

Xu, L., Wang, A., Li, X., & Oh, K. W. (2020). Passive micropumping in microfluidics for point-of-care testing. *Biomicrofluidics, 14*(3), 031503.

Yamada, K., Shibata, H., Suzuki, K., & Citterio, D. (2017). Toward practical application of paper-based microfluidics for medical diagnostics: state-of-the-art and challenges. *Lab on a Chip, 17*(7), 1206-1249.

Yang, A.-S., Chuang, F.-C., Chen, C.-K., Lee, M.-H., Chen, S.-W., Su, T.-L., & Yang, Y.-C. (2015). A high-performance micromixer using three-dimensional Tesla structures for bio-applications. *Chemical Engineering Journal, 263*, 444-451.

Yang, J., Wang, K., Xu, H., Yan, W., Jin, Q., & Cui, D. (2019). Detection platforms for point-of-care testing based on colorimetric, luminescent and magnetic assays: A review. *Talanta, 202*, 96-110.

Zhang, S., Winoto, S., & Low, H. (2007). Performance simulations of Tesla microfluidic valves. *Scientific Reports, 3*(14), 1314

Zhang, Y.-L., Tong, J.-B., & Zhu, Z.-C. (2023). Numerical calculation of forward and reverse flow in Tesla valves with different longitudinal width-to-narrow ratios. *Scientific Reports, 13*(1), 12496.

APPENDICES

Appendix A: Journal Publications

1. **Buglie, W. L.,** Tamrin, K. F., Sheikh, N. A., Yasin, M. F. M., & Mohamaddan, S. (2022). Enhanced fluid mixing using reversed multi-stage Tesla micromixer. *Chemical Engineering & Technology, 45*(7), 1255-1263.
2. **Buglie, W.,** & Tamrin, K. (2022). Enhanced mixing in dual-mode cylindrical magneto-hydrodynamic (MHD) micromixer. *Proceedings of the Institution of Mechanical Engineers, Part E: Journal of Process Mechanical Engineering,* 9544089221093596.
3. **Buglie, W. L.,** & Tamrin, K. (2023). Investigation of sub-atmospheric pressure-inducing micropump for enhanced micromixing performance. *Chemical Engineering & Technology,* 202200366.
4. **Buglie, W.,** Tamrin, K. Yasin, M. F. M., & Rahmatullah, B. (2023). Novel design of micropump based on multi-angle paper-based capillary approach for enhanced and well-controlled flow rates. *Proceedings of the Institution of Mechanical Engineers, Part E: Journal of Process Mechanical Engineering,* 9544089221093596.